
Fibration, Nexus and Cosmological Composite Topological Defects in Uniaxially Disordered Superfluid ^3He

Author:
Kuang. Zhang

Topological Quantum Fluids (ROTA) Group, Aalto University
Department of Mathematics and Statistics, University of Helsinki

July 5, 2021

Abstract

Fibration, Nexus and Cosmological Composite Topological Defects in Uniaxially Disordered Superfluid ^3He

by Kuang. Zhang

The liquid Helium-3 is the unique member in the many bodies systems and condensed matter systems. This is not only because it never freezes to solid even in zero temperature by the existence of strong enough quantum fluctuation, but also because it has complicated enough symmetry breaking patterns to different superfluid phases. The related discussions started from 1960s till now, and lots of intriguing physics have been proposed or been observed, such as novel topological defects and chiral anomaly of quisaiparticle induced by the textures of order parameters.

In last decade years, the impurity with nanometer length scales, i.e., aerogel was introduced into the liquid Helium-3 to modify the scattering properties of Helium-3 quasiparticles. One of them, the nafen, which is collection of thin Al_2O_3 strands is used in the ROTA's experiment, and generates a series of axially polarized new phases, in which the half quantum vortices have been observed.

The half quantum vortices are firstly stabilized in polar phase, which is also the first observed nafen distorted superfluid phase of Helium-3. This novel string defects are analogy of the cosmological strings which probably appear in the early universe. The existence of half quantum vortices provides the clue about the existence of other cosmological objects in the nafen distorted superfluid. To solve this question, we analyzed the possible symmetry breaking patterns in detail by using the algebraic topology and group theory. It turns out that the fibrations of the degenerate parameter spaces of symmetry breaking patterns dominate the existence of composite cosmological defects in the successive symmetry breaking of nafen distorted Helium-3.

In this review, the fibrations of degenerate parameter spaces in the successive symmetry breaking phase transition of nafen distorted superfluid Helium-3 are revealed by using the homotopy theory and group theory. The results of this deep mathematics i.e., the composite string monopole (Nambu monopole) and the string wall (Kibble-Lazarides-Shafi domain wall) are described topologically by using the exact sequences of homotopy groups. To compare our model with ROTA's experiment of string wall, we demonstrate how the topological defects with coherent length scales extend to mesoscopic spin solitons in equilibrium states. After this, the equilibrium free energies, which determines the extended equilibrium configurations, are evaluated by non-linear numerical optimization algorithm. Based on these equilibrium configurations, we calculated the spectrum of spin dynamical response of system under weak magnetic driving. The results exactly coincide with the experimental observations.

In addition, the implements of the numerical algorithms, which were used to evaluated the equilibrium configurations of spin solitons and the spin dynamical response, also generate a useful programs library. The massive applications of the functional analysis and theory of integral operators in the algorithms and their implements provide a instance, through which the physical expressions can be mapped to data objects of computer and evolve as physical expressions require.

Acknowledgements

We especially thank the instructive and inspiring discussions and comments from professor Grigory. E. Volovik during the process of this work. We thank Hiromitsu Takeuchi, Mikhail Silaev, Jaakko Nissinen, Vladislav Zavyalov and professor Erkki. V. Thuneberg for important discussions. We also thank professor Vladimir. B. Eltsov, Jere. T. Mäkinen and Juho. Rysti for instructive discussions about experiments of polar distorted B-phase. This work has been supported by the European Research Council (ERC) under the European Union's Horizon 2020 research and innovation programme (Grant Agreement No. 694248).

Contents

Abstract	iii
Acknowledgements	v
1 Introduction	1
2 Symmetry Breaking Phase Transitions and Topological Defects in Polar Distorted Superfluid ^3He	5
2.1 The Primary Symmetry Groups of Normal Phase Vacuum of Nafen Distorted ^3He	5
2.2 Conventional Symmetry Breaking Scheme of Nafen Distorted ^3He and Vacuum Manifolds	7
2.2.1 Transition from normal phase to polar phase	7
2.2.2 From polar phase to PdB phase	7
2.2.3 From normal phase to PdB phase	8
2.3 Topological Objects Generated from Different Symmetry Breakings . .	8
2.3.1 Defects in polar phase	8
2.3.2 Defects in PdB phase with R_1	10
2.3.3 Defects in PdB phase with R_2	10
Spin vortices	10
Unstable monopoles and spin vortices	11
HQVs and the KLS domain wall	11
3 Fibration and Composite Cosmological Objects	13
3.1 Relative Homotopy Groups and Fibration between Vacuum Manifolds	13
3.2 Composite Cosmological Objects and Exact Sequences	16
3.2.1 Strings terminated by monopole – String Monopole	16
3.2.2 Wall bounded by string – KLS string wall	16
3.3 Skyrmions and Nexus in the presence of magnetic field	19
4 Equilibrium Configurations of the Extended Structures of KLS String Wall	23
4.1 Vacuum manifolds in the presence of orientation energies	23
4.2 1D nexus objects and spin solitons	27
4.2.1 Spin configuration of KLS string wall – half spin vortices	27
4.2.2 Spin soliton described by $\pi_1(R_1^H, \tilde{R}_1^{SOC})$	27
4.2.3 Short exact sequence of $\pi_1(S_S^1, \tilde{R}_2)$ and 1D nexus	30
4.2.4 Two different configurations of 1D nexus object – separable and inseparable	30
4.3 Equilibrium textures of pseudo-random lattices	31
4.3.1 Pseudo-random lattices	33
4.3.2 Spin solitons in the absence of KLS string walls – solitons and big-solitons	36

4.3.3	Spin solitons in the presence of KLS string walls – Boundary conditions on wall	36
4.3.4	Equilibrium spin textures and free energies of pseudo-random lattices consisting of inseparable and separable 2/4 spin solitons	37
4.4	The mirror symmetry of 1D nexus objects and its breaking	41
5	Spin Dynamical Response and NMR	45
5.1	Spin dynamic response equations	46
5.2	NMR of 1D nexus objects	49
5.2.1	Transverse NMR frequency shifts and surface densities of ratio intensity — inseparable spin solitons	53
5.2.2	Transverse NMR frequency shifts and surface densities of ratio intensity — separable spin solitons	53
6	Conclusion and Outlook	55
A	Fibration, Relative Homotopy Groups and Exact Sequences	59
A.1	Long and short exact sequences	59
A.1.1	LES and SES of $\pi_n(R_P)$	59
A.2	Extensions with and without magnetic field	60
A.2.1	No Magnetic Field	60
A.2.2	In the presence of magnetic field	61
A.3	Fibration and a theorem	61
B	Sobolev Space, Non-Linear Optimization and Discrete Eigen-Value Problem	63
B.1	Ritz strategy and finite elements partition	63
B.2	BFGS algorithm and implements	65
B.3	Garlkin strategy with finite element partition	74
C	Simplifications of Eign-Equations	75
C.1	The derivation of the first order dynamic equation	75
C.2	The derivation of the second order dynamic response equation	77
C.3	The derivation of transverse NMR response equation	78
C.4	All $\Xi_{\alpha\lambda}$ terms in Eq. (5.19)	78
D	Separable spin soliton with $\theta_{KLS} = \pi$ and its NMR	81
D.1	Pseudo-random lattices with two different domain wall boundary conditions – $\theta_{KLS} = 0$ and $\theta_{KLS} = \pi$	81
D.2	NMR frequency shifts Of soliton ($ \Delta\theta = \pi - 2\theta_0$) and big-soliton ($ \Delta\theta = \pi + 2\theta_0$)	81
	Bibliography	85

Chapter 1

Introduction

The North American Nanohertz Observatory for Gravitational Wave (NANOGrav) team reported its finding from the accumulated data in 12.5 years at the end of 2020 [1–5]. Similar to the famous LIGO/Virgo, NANOGrav is a gravitational wave observatory. What the significant difference between them is that the NANOGrav is sensitive to gravitational wave with frequency in nanohertz scales. To implement this, scientists actually setup the observatory by utilizing our galaxy. Forty five pulsars were chosen to form the so called pulsar timing array, and their time ticks will change if a gravitational wave signal passes between the earth and the pulsars array. By analyzing the 12.5 years observation data, NANOGrav team reveals the possible existence of a stochastic background of gravitational wave, and this discovery takes the cosmological strings to the table of candidates of the sources for gravitational wave [6–8].

The cosmological strings typically appear in many different Grand Unify Theory (GUT) models and String-Theories [9–15]. Usually, these topological defects are proposed to appear when the primary GUT symmetry groups spontaneously breaks into its subgroups in the early age of universe after big bang [16–18]. Even the existence of cosmological strings is controversial [19–22], some of them, which have intriguing and novel properties, still have been discussed intensively in last decades, not only in cosmology, but also in condensed matter physics [23–32]. The Alice strings or half quantum vortices (HQVs) are one example of this kind of string defect [33, 34]. Alice strings appear when the residual symmetry of a symmetry breaking phase is disconnected and contains a \mathbb{Z}_2 subgroup, such that its two elements belong to the disconnected parts of the residual symmetry group respectively [33]. In the experiment of ROTA group of Aalto University, this is implemented in the polar phase of ^3He , which results from the modifications of microscopic scattering properties by axially polarized impurity i.e., nafen aerogel [35].

The idea, that introducing aerogel to modify the microscopic scattering properties of ^3He quasiparticles, was discussed and intensively practiced around late 1990s to 2000s by using isotropic SiO_2 aerogel [36–58]. Because the characteristic length of aerogel is less than coherent length of Cooper pairing of superfluid ^3He , this impurity may dramatically modify the stable phase and the equilibrium phase diagram of superfluid ^3He [59–65]. In the case of nafen aerogel, which consists of randomly distributed parallel Al_2O_3 strands, the polar phase was predicted as the possible new phase and later be identified experimentally [51, 62, 66, 67]. This new phase dominates the most part of the phase diagram, and the reason of its domination was explained by the Anderson-Fomin theorem [68–71]. Moreover, the new phase diagram shows the two-step successive symmetry breaking phase transitions via polar phase is possible [51, 60, 72, 73]. When the temperature of polar phase superfluid reaches

the transition temperature of polar distorted B-phase (PdB), the second time symmetry breaking phase transition occurs [73, 74]. If this transition happens just below the transition temperature of phase transition from polar phase to PdB phase, a very fantastic composite topological object – the Kibble-Lazarides-Shafi (KLS) string domain wall will appear in the distorted superfluid ^3He [74].

This novel composite cosmological object and the corresponding symmetry breaking pattern was introduced in the 1980s. As an example, Kibble, Lazarides and Shafi discussed the two-step symmetry breaking of $spin(10)$ gauge theory to $H = \{H_0, K\}$, where $H_0 = spin(6) \otimes spin(4)$ and $K = H_0 i\sigma_{67}$ [28, 29, 75]. Because the charge conjugation $C = i\sigma_{67}i\sigma_{23}$ is an element of K , this symmetry breaking generates Alice string as we have mentioned. At the second stage of symmetry breaking from H to the $SU(3) \times SU(2) \times U(1)$, the charge conjugation symmetry C is broken, as a result, domain wall appears and is terminated on the Alice string. Following the idea of KLS, similar two-step symmetry breaking pattern were discussed in different unified gauge models. And physicists soon found that this mechanism induces domain wall problem of the axion solution of the CP violation in QCD [76–82]. In the axion solution, two phase transitions successively occur in our universe during its temperature cools down. In the first time transition, the $U(1)_{PQ}$ symmetry of Peccei-Quinn mechanism spontaneously breaks, then the axion and string defect appear. When the cosmic temperature reaches the QCD temperature, the $U(1)_{PQ}$ symmetry breaks to discrete symmetry and then the domain wall appears. As a result, the cosmic strings formed in the first time symmetry breaking convert to string domain wall under QCD temperature [78, 81]. The universe which has this structure will be very different with what we have observed. In order to solve this problem, a lots of ideas have been reported, and the corresponding decay dynamics of the string wall system also be researched [83–87].

In spite of the controversy about the route of the string walls decay, the story looks running well until we take the Nambu monopole (string monopole) into account [88]. This unusual monopole may be generated by different mechanism beside the two-step successive symmetry breaking pattern [89]. However, it has an unanticipated similarity with the KLS string domain wall, that is, Nambu monopole is the composite cosmological object formed by combination between zero dimensional object (monopole) and one dimensional object (string). While the KLS string domain wall is formed by combination between one dimensional object (string) and two dimensional object (domain wall). Considering about that the polar phase, though which the successive symmetry breaking occurs, also has monopole because its π_2 groups is non-trivial, we started to get the idea that the monopole of polar phase may convert to Nambu monopole in a similar way, in which Alice string converts to KLS string domain wall when the second symmetry breaking happens. Fortunately, the answer is yes. In the system with two-step successive symmetry breaking pattern, there is general mechanism to guarantee the cosmological objects appearing in the first time symmetry breaking convert to composite topological objects during the second time symmetry breaking occurs. And this guarantee has a deep mathematical origin in algebraic topology [90].

In this review, we demonstrate in details what this guarantee is by using the algebraic topology and group theory. The significant tools are the relative homotopy groups and the exact sequences consisting of homotopy groups and relative

homotopy groups of the degenerate parameter spaces of PdB order parameters. We will see how the composite topological defects are classified by relative homotopy groups and characterized by boundary homomorphism of the corresponding exact sequences. Originally the classification in terms of the relative homotopy groups has been used if there is the hierarchy of the energy scale or length scales in physical system [91–93], when each energy scale has its own well defined vacuum manifold R_i – the space of the degenerate states. In our case of two-step successive symmetry breaking transitions, two energy scales arise in the vicinity of the second transition. There, the coherence length related to the first symmetry breaking is much smaller than the coherence length related to the second symmetry breaking. This gives rise to two well defined degenerate parameter spaces, and allows us to apply the relative homotopy groups. By directly calculating the exact sequences and relative homotopy groups $\pi_n(R_1, R_2)$, where R_1 and R_2 are degenerate spaces of PdB phase generated from different vacua, we found the string monopole (Nambu monopoles) and KLS string wall are classified by $\pi_2(R_1, R_2)$ and $\pi_1(R_1, R_2)$ groups respectively. Moreover, we found an amazing fact, that is $\pi_n(R_1, R_2)$ are always isomorphic to $\pi_n(R_P)$, which are the homotopy groups of topological defects in polar phase, i.e.,

$$\pi_n(R_P) = \pi_n(R_1, R_2), \quad (1.1)$$

where $n \in \mathbb{Z}^+$ and $n \geq 1$. This means the topological defects in polar phase convert to composite cosmological defects when the second time symmetry breaking occurs! Facing to this amazing fact, all physicists must ask why? Our work reveal that there is fibration between PdB phase vacuum manifold and polar phase vacuum manifold, and this fibration determines that $\pi_n(R_1, R_2)$ must equal to $\pi_n(R_P)$.

The rest parts of review are organized as follows. In Chapter. 2 we consider the conventional scheme of the symmetry breaking and the vacuum manifolds of different superfluid phases appeared in the two-step successive transitions in the polar distorted ^3He . The topological defects in these phases are described in terms of the conventional homotopy groups. In Chapter. 3 we discuss the composite topological objects in the vicinity of the second transition. We use the relative homotopy groups and corresponding exact sequence of homomorphisms to classify the composite objects, which are topologically stable in the vicinity of the transition. We demonstrate how fibration of the degenerate parameter spaces happens and what it results in. In order to test our theory with experiment about the KLS string wall of ROTA group, we further discuss the equilibrium extended structures of the KLS string wall with length scale around the dipole length in Chapter. 4. In Chapter. 5, we calculate NMR frequency shift – the experimental observable of the extended structures of KLS string wall by using the linear response theory. The results of numerical simulations exactly coincide with the experimental observations. We summarize the researches and discuss the future work which deserve to be focused on in Chapter. 6. In the appendices, we provide some essential background discussions about technical details.

Chapter 2

Symmetry Breaking Phase Transitions and Topological Defects in Polar Distorted Superfluid ^3He

2.1 The Primary Symmetry Groups of Normal Phase Vacuum of Nafen Distorted ^3He

The continuous phase transition is understood as spontaneous symmetry breaking by order parameters about a primary symmetry group G . In most case, order parameters are elements of (complex) vector spaces in which the primary symmetry group G is represented. For example, the magnetization vector of ferromagnetic materials is element of 3-dimensional Euclidean space, where the $SO(3)$ spin rotation is represented. And the order parameter of s-wave superconductor is element of complex number set, which provides $S = 0$ and $L = 0$ representation of $SO_S(3) \times SO_L(3) \times U(1)$ group, where S and L are quantum numbers of spin and orbital angular momentums.

In ^3He liquid at low temperature, the basis vectors of vector spaces are eigenfunctions of $S = 1$ and $L = 1$, thus the order parameters space consists of two 3-dimensional vector spaces and the phase space. This gives rise to the bilinear complex-valued order parameter i.e., dyadic tensor $A_{\alpha i}$ [94], which transforms under the action of spin, orbital and phase rotations of the primary group G . Stabilizer of those actions, which is collection of the residual symmetry transformations of given order parameter, forms the residual symmetry group H of superfluid phase of ^3He .

In our case, the symmetry group G of normal liquid ^3He in the "nematically ordered" aerogel with the uniaxial anisotropy is different from that in the bulk ^3He [94]. In ROTA's experiment, the nafen aerogel consisting of parallel-distributed Al_2O_3 strands with diameter around 8nm is immersed in to liquid ^3He [66, 72, 74, 95]. The coupling energy between the orbital vector of order parameter and nafen strand is proportional to

$$\eta_{ij} A_{\alpha i} A_{\alpha j}^*, \quad (2.1)$$

where η_{ij} is tensor describing the coupling between aerogel and orbital degree of freedom (DoF) for Cooper paring. In the case of spatially isotropic aerogel, η_{ij} is an

isotropic tensor and can be written as

$$\eta_{ij}^{isotropic} = \eta_0 \delta_{ij}, \quad (2.2)$$

where η_0 is the eigenvalue of $\eta_{ij}^{isotropic}$. When the aerogel turns to be axially polarized like nafen aerogel, the anisotropic traceless part appears and then η_{ij} can be written as

$$\eta_{ij} = \eta_0 \delta_{ij} + 3\kappa(\hat{u}_i \hat{u}_j - \frac{1}{3} \delta_{ij}), \quad (2.3)$$

where $\kappa = (\eta_0 - \eta_\perp)$ and η_\perp is the eigenvalue of η_{ij} along the directions perpendicular to the axially polarized axis i.e., direction of nafen strands [96]. The dimensionless parameters η_0 and κ describe the common gap shifts of all angular momentum states in the presence of aerogel and the discrepancies of the gap shifts between different angular momentum states because of the uniaxial anisotropy respectively [45, 50, 60, 73]. The unit vector $\hat{\mathbf{u}}$ represents the direction of nafen strands.

In the case with $\kappa < 0$, the $l_z = 0$ angular momentum state has biggest gap and highest superfluid transition temperature [60, 61]. As a result, polar phase with uniaxially polarized orbital vector $\hat{\mathbf{z}}$ is system-favorable when temperature decreases [35]. The relative direction between $\hat{\mathbf{z}}$ and $\hat{\mathbf{u}}$ of bulk equilibrium state is determined by minimum of Eq. (2.1). For polar phase with order parameter $A_{\alpha i} \sim \Delta_P \hat{d}_\alpha \hat{z}_i$, Eq. (2.1) suggests $\hat{\mathbf{z}} \parallel \hat{\mathbf{u}}$ immediately. These influences induced by the nafen aerogel to superfluid ^3He significantly modify the symmetry of this p-wave system. In fact the orbital three dimensional rotation symmetry group $SO_L(3)$ of pure ^3He is reduced to $O_L(2)$ because the orbital $\hat{\mathbf{z}}$ vector is parallel to the nafen strands in all cases [74, 97]. This situation is equivalent to say the normal phase vacuum has the following primary symmetries:

$$O_L(2) \times SO_S(3) \times U(1) \times T \times P, \quad (2.4)$$

where $SO_S(3)$ is the group of spin rotations; $U(1)$ is the global gauge group of phase degree of freedom, which is broken in superfluid states; T is time reversal symmetry; P is parity; $O_L(2) \cong SO_L(2) \rtimes C_{2x}^L$ where C_{2x}^L is π rotation in orbital space about the traverse axis.

Microscopic theories have predicted that the polar phase is the stable phase in this nafen distorted system [51, 62] and this predictions was experimentally identified later [66, 67]. However, the unexpected part of story is polar phase dominates a huge part of phase diagram. Later it became clear that the main reason of the domination of the polar phase in nafen distorted ^3He is the extension of the Anderson theorem [68] – the Anderson-Fomin theorem of the polar phase with columnar impurities i.e., the transition temperature to the polar phase is practically not suppressed by the strands of nafen [69–71], as distinct from the other superfluid phases. Similar extension of the Anderson theorem was also discussed in multi-orbital superconductors [98]. Recently, another signature of the Anderson-Fomin theorem in polar distorted ^3He is the detected T^3 dependence of the gap amplitude that results from the non-suppression of Dirac nodal line of the spectrum of Bogoliubov quasiparticles in the polar phase [99].

In what follows, we ignore the time reversal symmetry, since it is not broken

in the polar and in PdB phases, and also ignore the parity P which is reduced to $Pe^{i\pi}$ in all p -wave superfluid phases, where $e^{i\pi}$ is the π -rotation in phase space. Also, because we focus on the topological objects related to the spin and $U(1)$ gauge parts of the order parameter, the $\mathbb{Z}_2 = \{0, C_{2x}^L\}$ symmetry coming from C_{2x}^L could be neglected in the rest parts of this review. Then the referring starting group G of symmetry breaking schemes in this review is

$$G = SO_L(2) \times SO_S(3) \times U(1). \quad (2.5)$$

Starting from this normal phase vacuum, we discuss three different of phase transition: (a) from the normal phase to the polar phase; (b) from the polar phase to the PdB phase; and (c) Direct transition from the normal phase to the PdB phase. In Sec. 2.3 we consider the topological objects related to these symmetry breaking scenarios, using the conventional approaches of homotopy groups.

2.2 Conventional Symmetry Breaking Scheme of Nafen Distorted ^3He and Vacuum Manifolds

2.2.1 Transition from normal phase to polar phase

As we mentioned, the order parameter in the p -wave spin-triplet superfluids is the dyadic tensor $A_{\alpha i}$, which transforms as a vector under spin rotation (the greek index) and as a vector under orbital rotations (the latin index). In the polar phase it has the form:

$$A_{\alpha i}^P = \Delta_P \hat{d}_\alpha \hat{z}_i e^{i\Phi}, \quad (2.6)$$

where Φ is the phase, $\hat{d}_\alpha (\equiv \hat{\mathbf{d}})$ and $\hat{z}_i (\equiv \mathbf{u})$ are unit vectors of spin and orbital uniaxial anisotropy respectively, and Δ_P is the gap amplitude. The residual symmetry group of the polar phase, the stabilizer of the order parameter in Eq. (2.6), is

$$H_P = SO_L(2) \times SO_S(2) \rtimes \mathbb{Z}_2^{S-\Phi} \subset G. \quad (2.7)$$

Here $\mathbb{Z}_2^{S-\Phi} = \{1, C_{2x}^S e^{i\pi}\}$, where C_{2x}^S is π -rotation of the vector $\hat{\mathbf{d}}$ about perpendicular axis and $e^{i\pi}$ is the phase rotation by π , i.e. $\Phi \rightarrow \Phi + \pi$. Then the vacuum manifold of the polar phase is given as

$$R_P \cong G/H_P \cong (S^2 \times U(1))/\mathbb{Z}_2. \quad (2.8)$$

The coherence length $\xi = \hbar v_F / \Delta_P$ in the polar phase is the smallest length scale in our question, which determines the size of singular (hard core) topological defects in the polar phase.

2.2.2 From polar phase to PdB phase

Let us now consider the second symmetry breaking phase transition: from the polar phase vacuum with fixed $\hat{\mathbf{d}}$ and Φ to the PdB phase. In the vicinity of this transition the order parameter in Eq. (2.6) acquires the symmetry breaking term with amplitude $q \ll 1$:

$$A_{\alpha i}^{PdB} = e^{i\Phi} \Delta_P [\hat{d}_\alpha \hat{z}_i + q(\hat{\mathbf{e}}_\alpha^1 \hat{x}_i + \hat{\mathbf{e}}_\alpha^2 \hat{y}_i)]. \quad (2.9)$$

Here $\hat{\mathbf{e}}^1$, $\hat{\mathbf{e}}^2$ and $\hat{\mathbf{d}}$ are three orthogonal vectors in spin space. The corresponding coherence length of the second transition ξ/q is large in the vicinity of this transition. This provides the hierarchy of the length scales, ξ and $\xi/q \gg \xi$.

The residual symmetry subgroup of the PdB phase in the symmetry breaking from the polar phase is

$$H_{\text{PdB}} = SO_{S-L}(2) \subset H_P, \quad (2.10)$$

where $SO_{S-L}(2)$ represents the common rotations of spin and orbital spaces. The manifold of the vacuum states, which characterizes the second symmetry breaking is:

$$R_2 \equiv R_{P \rightarrow \text{PdB}} = H_P / H_{\text{PdB}} \cong SO_{L-S}(2) \times \mathbb{Z}_2^{S-\Phi}. \quad (2.11)$$

Here PdB phase breaks one of $SO(2)$ symmetries of H_P respecting to relative rotations of spin and orbital spaces.

2.2.3 From normal phase to PdB phase

Here we consider the two-step symmetry breaking from normal phase to PdB phase with a general view point, which the parameter q is not necessarily small. In this general case there is only a single length scale which is relevant i.e., the coherent length ξ_{PdB} of Cooper pairing in PdB phase, and thus this situation becomes similar to that of the direct transition from the normal state to the PdB phase, $G \rightarrow H_{\text{PdB}}$. The order parameter Eq. (2.9) of the PdB phase could be written as

$$A_{\alpha i}^{\text{PdB}} = e^{i\Phi} [\Delta_{\parallel} \hat{d}_{\alpha} \hat{z}_i + \Delta_{\perp} (\hat{\mathbf{e}}_{\alpha}^1 \hat{x}_i + \hat{\mathbf{e}}_{\alpha}^2 \hat{y}_i)], \quad (2.12)$$

where $\Delta_{\perp} \leq \Delta_{\parallel}$. The corresponding residual symmetry group is still Eq. (2.10), and the vacuum manifold of PdB phase in this scenario of symmetry breaking is:

$$R_1 \equiv R_{\text{normal} \rightarrow \text{PdB}} \cong G / H_{\text{PdB}} \cong SO_{S-L}(3) \times U(1). \quad (2.13)$$

2.3 Topological Objects Generated from Different Symmetry Breakings

In this Section we consider the topologically stable defects, which emerge at each of three symmetry breaking transitions discussed in Sec. 2.2.

2.3.1 Defects in polar phase

The polar phase vacuum manifold Eq. (2.8) has the homotopy groups

$$\pi_1(R_P) = \tilde{\mathbb{Z}}, \quad \pi_2(R_P) = \mathbb{Z}, \quad \pi_0(R_P) = 0. \quad (2.14)$$

And the calculation details of $\pi_n(R_P)$ are put into Appendix. A.1.1. The group $\pi_1(R_P) = \tilde{\mathbb{Z}} = \{n/2 | n \in \mathbb{Z}\}$ includes the integers of the group \mathbb{Z} via inclusion map: $n \in \mathbb{Z} \hookrightarrow n \in \tilde{\mathbb{Z}}$, which describes the free quantized vortices with integer winding number. More significantly, $\pi_1(R_P)$ contains the set of half-odd integers, i.e., $\{n + 1/2 | n \in \mathbb{Z}\}$. This subset describes vortices containing HQV, which has one-half circulation of a conventional quantized vortex. The reason which polar phase has HQVs can be retrospected to the discussion about the disconnected residual symmetry of a given symmetry breaking phase in Chapter. 1. From the Eq. (2.7), we can see the $\mathbb{Z}_2 = \{1, C_{2x}^S e^{i\pi}\}$ is subgroup of H_P , then there are two possible ways

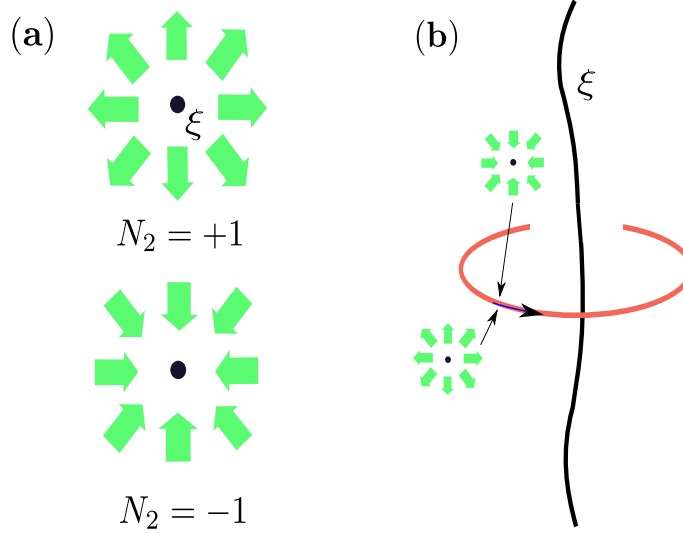


FIGURE 2.1: Topological defects in the polar phase. We omit the free conventional vortices of group \mathbb{Z} . (a) $\hat{\mathbf{d}}$ -vector monopole and anti-monopole described by the homotopy group $\pi_2(R_P)$ with topological charges $N_2 = \pm 1$ respectively. Their core size are on the order of the coherence length ξ . The green arrows depict the configuration of $\hat{\mathbf{d}}$ vectors. (b) Half-quantum vortex (HQP) described by the \mathbb{Z}_2 subgroup of $\pi_1(R_P)$ with core size $\sim \xi$. This object also got the name "Alice string", because the $\hat{\mathbf{d}}$ monopole transforms to the anti-monopole after going around the HQV, in the same manner as it happens for the charge going around Alice string [34]. The red circle shows the path.

to move around linear defect in polar phase, one is moving back to the starting point state, while the other one is continuously moving to the π -rotation state (analog to Charge conjugation state) as shown in Fig. 2.1(b), which is transferred from the starting point state by action of $C_{2x}^S e^{i\pi}$. This means the HQVs with the topological charges $N = \pm 1/2$ are the analogs of the cosmological Alice strings [33, 34].

The group $\pi_2(R_P) = \mathbb{Z}$ describes the hedgehogs (monopoles) in the $\hat{\mathbf{d}}$ -field, as shown in Fig. 2.1(a). The core sizes of vortices and monopoles in polar phase are on the order of the coherence length $\xi = \hbar v_F / \Delta_P$. In the presence of HQVs, The topological classification of hedgehogs is modified to \mathbb{Z}_2 from \mathbb{Z} because of the Charge conjugation symmetry. The monopole transforms to anti-monopole when circling around the Alice string (HQP), and thus in the presence of HQVs the hedgehogs (monopoles) of the group \mathbb{Z} is degenerated with the anti-monopole of group \mathbb{Z} . This phenomenon is an example that $\pi_2(R)$ group may be influenced by $\pi_1(R)$ topology [100].

The HQVs have been identified in NMR experiments of polar phase [35]. By applying static magnetic field tilted with respect to nafen strands, one creates the soliton as extended structure, which has dipole length scale, attached to the HQVs. This mesoscopic extended structure produces the measured frequency shift in the NMR spectrum under RF magnetic drive. Unfortunately, Hedgehogs (monopoles) are still not identified in superfluid ^3He .

2.3.2 Defects in PdB phase with R_1

The vacuum manifold R_1 of the PdB phase in Eq. (2.13) has homotopy groups

$$\pi_1(R_1) = \mathbb{Z} \times \mathbb{Z}_2, \quad \pi_2(R_1) = 0, \quad \pi_0(R_1) = 0. \quad (2.15)$$

Different with the polar phase, which has QHVs and monopoles, the topologically protected defects of PdB phase are integer-quantized phase vortices of \mathbb{Z} and spin vortices with \mathbb{Z}_2 in the general case as we mentioned in Sec. 2.2.3. The hard core (sized by ξ) defects (HQVs and hedgehogs) of polar phase are not supported by topology any more. Moreover, the new topological object – the \mathbb{Z}_2 spin vortices are similar to that which have been observed in the bulk B-phase [101].

2.3.3 Defects in PdB phase with R_2

The vacuum manifold R_2 of the PdB phase generating at the symmetry breaking transition from the polar phase vacuum in Eq. (2.11) has homotopy groups:

$$\pi_1(R_2) = \mathbb{Z}, \quad \pi_2(R_2) = 0, \quad \pi_0(R_2) = \mathbb{Z}_2. \quad (2.16)$$

These homotopy groups are responsible for the topological defects formed in the symmetry breaking transition from the fixed degenerate vacuum of the polar phase (with $\hat{\mathbf{d}} = \text{const}$ and $\Phi = \text{const}$) to the PdB phase. These topological defects are such important because they connect to defects with higher spatial dimension and then form the composite topological defects in the vicinity of the second time symmetry breaking transition. We will discuss this soon in Chapter. 3. Before that, Let us consider them in details separately.

Spin vortices

The homotopy group $\pi_1(R_2) = \mathbb{Z}$ describes the spin vortices with $2\pi n$ rotation of vectors $\hat{\mathbf{e}}^1$ and $\hat{\mathbf{e}}^2$ about the fixed $\hat{\mathbf{d}}$ vector of the polar phase. The winding number is:

$$n_1 = \frac{1}{2\pi} \oint dx^i \hat{\mathbf{e}}^1 \cdot \nabla_i \hat{\mathbf{e}}^2. \quad (2.17)$$

This relation is analogy with the winding number of integer-quantized vortices of superfluid A-phase, in which the differential 1-form is formed by the two perpendicular unit vectors in orbital degree of freedom [102]. In the vicinity of the transition, these spin vortices get the soft core of size $\xi/q \gg \xi$, which corresponds to the coherent length of symmetry breaking from the polar to the PdB phase. As distinct from the topological defects in the polar phase, which have the "normal phase" core of size ξ , the spin vortices in the PdB phase with R_2 have the "polar phase" core. Then we get a multicomponent systems, in which the order parameter is not necessarily equal to zero on the axis of the topological defects. This fact may modify the model of continuous phase transition of symmetry breaking to the model of first order phase transition via the appearance of the nucleation of new phase [103–105]. When the PdB phase with R_2 transform to the polar phase, the proliferation of spin vortices of $\pi_1(R_2)$ in PdB marks this kind of modification.

Unstable monopoles and spin vortices

Since in the PdB phase $\pi_2(R_1) = \pi_2(R_2) = 0$, there is no way to protect hedgehog (monopole) of polar phase topologically when the second time symmetry breaking to PdB phase occurs. In fact, the $\hat{\mathbf{d}}$ -vector hedgehog converts to the termination point of the spin vortices of $\pi_1(R_2)$ with two quanta, as we will discuss in detail in the Chapter. 3. As a result the spin-vortices-dressed $\hat{\mathbf{d}}$ -hedgehog in PdB phase, which is generated by two-step successive symmetry breaking transition, becomes the analog of Nambu monopole, which terminates the electroweak cosmic string [88].

HQVs and the KLS domain wall

Similar situation takes place with the HQVs of polar phase, which are not topologically stable in the PdB phase. They become the termination lines of the domain walls of $\pi_0(R_2)$. We will discuss this mechanism in Chapter. 3, and we will see this process actually is analogy of the mechanism, though which the Kibble-Lazarides-Shafi (KLS) domain wall appears [28]. In ^3He experiments, after transition from the polar phase to the PdB phase in the presence of HQVs, the KLS walls appear between the neighboring vortices, and in spite of the tension of domain walls, the HQVs remain pinned by the nafen strands [52, 56, 74, 97].

In general the KLS wall is not topologically stable, and can be stabilized only due to symmetry reasons [106]. However, in the vicinity of the transition to PdB phase from the polar phase vacuum, the KLS wall becomes topological by the meaning of fibration of between vacuum manifolds R_1 and R_P . The topological domain wall of the thickness ξ/q is described by the nonzero element of the homotopy group $\pi_0(R_{P \rightarrow \text{PdB}}) = \mathbb{Z}_2$. Example of such a wall is the domain wall between the domains with $A_{\alpha i} = \Delta_P \text{Diag}(1, q, q)$ and $A_{\alpha i} = \Delta_P \text{Diag}(1, q, -q)$.

Chapter 3

Fibration and Composite Cosmological Objects

In this Chapter, we discuss how to practice the method of relative homotopy group within the case of two-step successive symmetry breaking transition in polar distorted superfluid ^3He . We also discuss how fibration between different vacuum manifolds emerges and significantly influence physics of topological defects. The nexus object consisting of vortex skyrmion and string monopole in the presence of orientation energy — the magnetic energy, is discussed in Sec. 3.3.

3.1 Relative Homotopy Groups and Fibration between Vacuum Manifolds

As mentioned before, in the vicinity of the second transition, the system has two well separated length scales (gap energy scales), ξ and $\xi/q \gg \xi$. This leads to the new classes of objects, which combine the topology of both vacuum spaces, R_1 and R_2 . That is because the order parameter fields are mapped into different degenerate vacuum manifolds of PdB phase at different spatial regions when ξ and ξ/q are well separated, thus the homotopy classes of these unusual n -loops of order parameters constitute $\pi_n(R_1, R_2)$ [91, 108–110].

This combined topology can be illustrated by the following example of the KLS string wall. At small distances $\xi \ll r \ll \xi/q$ from the core of HQV, the HQV is described by the homotopy group $\pi_1(R_P)$. However, at larger distances $r \gg \xi/q$, the HQV becomes the termination line of the wall, which is described by the $\pi_0(R_2)$ topology and has size of ξ/q . As shown in Fig. 3.1(a), in this case, the 1-loop with big enough size ($\gg \xi/q$) is continuous mapping of R_1 , such that the two end-points of the 1-loop are mapped into R_2 . This kind of 1-loop is named as relative 1-loop [107]. All the equivalence classes of relative 1-loops constitute the relative homotopy group $\pi_1(R_1, R_2)$.

The similar physics takes place for string monopoles [88]. At small distances $\xi \ll r \ll \xi/q$ from the core of the hedgehog, it is described by the homotopy group $\pi_2(R_P)$, while at larger distances $r \gg \xi/q$, the monopole becomes the termination point of spin vortices described by the $\pi_1(R_2)$ topology, see Fig. 3.1(b). The relative 2-loop maps the order parameter fields into R_1 , of which one of the boundary manifold S^1 is mapped in to R_2 in the region with constant $\hat{\mathbf{d}}$ vector. Again, all the homotopy classes of relative 2-loops constitute the $\pi_2(R_1, R_2)$ group.

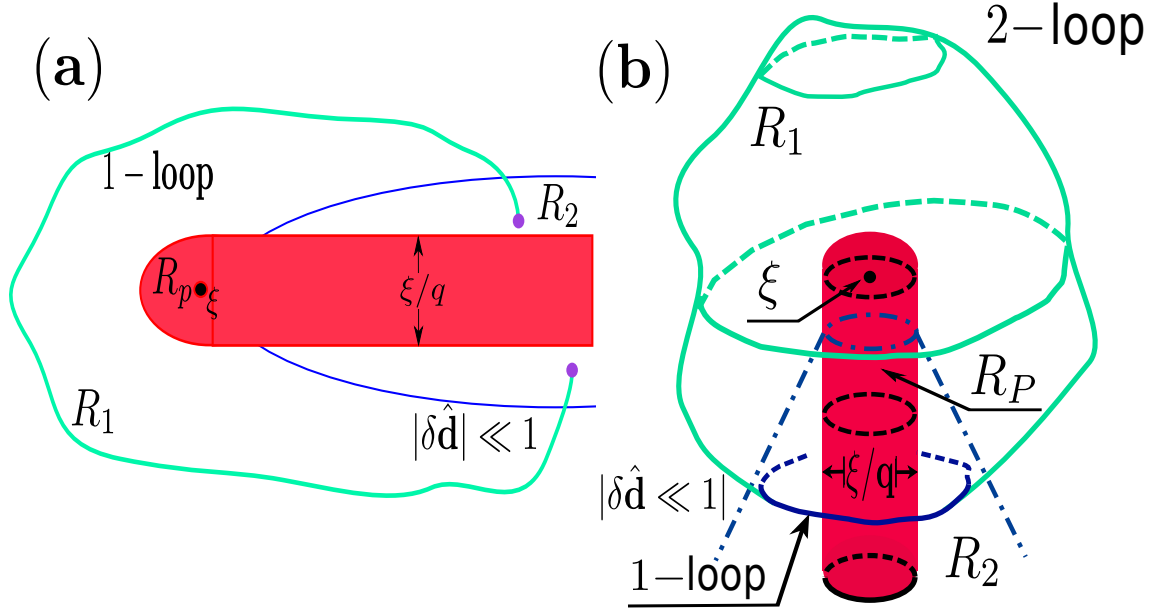


FIGURE 3.1: Illustration of relative n -loops describing the combined defects, which emerge in the two-step symmetry breaking transition in polar distorted ${}^3\text{He}$. (a) KLS string wall. In general the KLS wall is non-topological, but it acquires the nontrivial topology in the vicinity of the second phase transition. In this limit case there are two well separated length scales: the coherence length ξ of the first transition, which determines the size of the hard core of string (the black dot), and the much larger coherence length $\xi/q \gg \xi$ of the second transition, which determines the soft core size of the wall (the pink region). The hierarchy of scales gives rise to two types of the vacuum manifolds in the PdB phase, R_1 and R_2 . The R_1 includes all the degenerate vacua of the PdB phase, while the R_2 consists of those, which are obtained from the fixed order parameter of the polar phase, i.e. at fixed $\hat{\mathbf{d}}$ and Φ in Eq. (2.6). There exists spatial region, where the asymptotic condition $|\delta\hat{\mathbf{d}}| \ll 1$ is achieved. The blue line shows the characteristic border between the regions of two classes of vacuum manifolds. The topology of the string wall is determined by relative homotopy group $\pi_1(R_1, R_2)$, in which the green relative 1-loop is mapped to the space R_1 , with the ends of the loop mapped to R_2 [107]. (b) The string monopole is described by relative homotopy group $\pi_2(R_1, R_2)$. In this case the black dot shows the core of the hedgehog in the $\hat{\mathbf{d}}$ -field and the pink region is the core of 4π spin vortex, which is terminated by the hedgehog. The green 2-loop is mapped to the space R_1 , with its 1-loop edge mapped to R_2 [107]. The spatial boundary between R_1 and R_2 is shown as a cone-surface by blue-dash line.

In order to calculate $\pi_n(R_1, R_2)$ and properly understand the composite objects described by them, we need the help of exact sequence of homomorphisms of relative homotopy groups. All calculation details about these are put into Appendix. A. Even though $\pi_n(R_1, R_2)$ could be directly calculated, it is always good that we can get understanding of them from different viewpoint. For our case of two-step symmetry breaking phase transition, this part of story is the most excited.

Recalling the Eq. (2.7) and Eq. (2.10) in last chapter, we have $H_{PdB} \subset H_P$ and $H_P \subset G$, then we get

$$\frac{G/H_{PdB}}{H_P/H_{PdB}} = R_1/R_2 \cong R_P = G/H_P, \quad (3.1)$$

by the meaning of the third isomorphism theorem [111]. Equation. (3.1) suggests that there is continuous map

$$p : R_1 \rightarrow R_P, \quad (3.2)$$

through which the cosets kR_2 are mapped to elements of R_P isomorphically, where $k \in R_1$. Then (i) p is surjection from R_1 to R_P . Moreover, because p maps cosets of R_1 to elements of R_P , (ii) the image of inverse mapping $p^{-1}(U)$ with $U \subset R_P$ are disjoint union of cosets in R_1 because all cosets are disjoint [112, 113]. These two properties of p indicate the isomorphism $p : R_1 \rightarrow R_P$ is covering mapping and R_1 is covering space of R_P [114]. This important fact gives rise to fibration sequence

$$R_2 \hookrightarrow R_1 \xrightarrow{p} R_P \quad (3.3)$$

between vacuum manifolds R_1 and R_P , where R_2 is mapped into R_1 by inclusion. Fibration Eq. (3.3) immediately suggests

$$\pi_n(R_1, R_2) \cong \pi_n(R_P) \quad (3.4)$$

by applying an theorem in Appendix. A.3 [90]. In this case, we can see R_2 actually is fiber of this fibration. This means the vacuum manifold R_2 of PdB phase with fixed $\hat{\mathbf{d}}$ is generated from given vacuum state of polar phase, which corresponds to element of R_P , because $p^{-1}(e)$ with $e \in R_P$ homotopically equivalent to R_2 for fibration Eq. 3.3. Then we can get a natural and self-consistent result that

$$\pi_n(R_2^e) = \pi_n(R_2^f), \quad (3.5)$$

where $e, f \in R_P$ correspond to polar phase vacua with different $\hat{\mathbf{d}}$. More details see Appendix. A.3.

Equation. (3.4) is the kernel of this chapter, it demonstrates that in the vicinity of the phase transition from the first (polar) phase to the second (PdB) phase, all the topological objects of the first phase described by the group $\pi_n(R_P)$ retain their topological charges in the second phase, and thus convert to the topological objects in the second (PdB) phase. Some of these defects remain free, while the other become the parts of the composite defects – the string monopole and for the KLS string wall in Sec. 3.2.2 and Sec. 3.2.1 respectively. However, Eq. (3.4) does not resolve between the free and the composite objects of the second (PdB) phase. The full classification of the topological objects in the second phase depends not only on $\pi_n(R_1, R_2)$, but also on the details of the mappings in the exact sequence of homomorphisms

of $\pi_n(R_1, R_2)$, which is calculated in Appendix. A.2. The mapping diagram of the long exact sequence (LES) Eq. (A.6) in Fig. 3.2 depicts the relation between different topological objects in R_1 and R_2 .

3.2 Composite Cosmological Objects and Exact Sequences

3.2.1 Strings terminated by monopole – String Monopole

The relative homotopy group

$$\pi_2(R_1, R_2) \cong \pi_2(R_P) = \mathbb{Z}, \quad (3.6)$$

describes monopoles (hedgehogs) of $\hat{\mathbf{d}}$ field. They survive in the vicinity of the second transition as the topological objects which terminate the spin vortices. To demonstrate this, we need the short exact sequence (SES)

$$0 \rightarrow 0 \xrightarrow{i^*} \pi_2(R_1, R_2) \xrightarrow{\partial^*} 2\mathbb{Z} \rightarrow 0, \quad (3.7)$$

of $\pi_1(R_1, R_2)$, see calculation details in Appendix. A.2. The boundary homomorphism ∂^* describes the possible string defects connecting on the $\hat{\mathbf{d}}$ -monopoles. As shown both in Fig. 3.2 and in Eq. (A.2), $\text{im} \partial^* = 2\mathbb{Z}$, then there are spin vortices with even winding number connecting on non-trivial $\hat{\mathbf{d}}$ -monopole. This means the corresponding composite object – the string monopole – has two topological charges, n_2 and n_1 , which are related as:

$$n_2 = \frac{1}{8\pi} \epsilon^{ijk} \int_{S^2} dS_k \hat{\mathbf{d}} \cdot (\nabla_i \hat{\mathbf{d}} \times \nabla_j \hat{\mathbf{d}}) = \frac{1}{2} n_1. \quad (3.8)$$

Here S^2 is the surface encircling monopole and the group \mathbb{Z} is the group of integers n_2 – the topological charges of the hedgehog. While n_1 is the winding number of spin vortices in Eq. (2.17). The equation $n_1 = 2n_2$ in Eq. (3.8) shows that monopole is termination point of spin vortices with the even total charge n_2 in vicinity of the second time symmetry breaking. This situation is similar to the monopole in the chiral A-phase [89, 115–117], which either terminates a single vortex with $n_1 = 2$, or forms the nexus with two singly quantized vortices with $n_1 = 1 + 1 = 2$, or with four HQVs with $n_1 = 1/2 + 1/2 + 1/2 + 1/2 = 2$. Those vortices, which connect with monopoles ($n_2 > 0$) or antimonopoles ($n_2 < 0$) allow the existences of complex monopole-antimonopole networks [118–122].

Fig. 3.3 illustrates the configuration of the string monopole, which consists of the hedgehog with $n_2 = 1$ and two strings – spin vortices each with $n_1 = 1$. The spin vortices have a soft core with size ξ/q .

3.2.2 Wall bounded by string – KLS string wall

The relative homotopy group for KLS string wall is

$$\pi_1(R_1, R_2) \cong \pi_1(R_P) = \tilde{\mathbb{Z}}. \quad (3.9)$$

Even though Eq. (3.9) shows that the topological charges of string wall in the second (PdB) phase are the same as those in the first (polar) phase and they form the group of integer and half-odd integers in both phases, the physical realizations of these

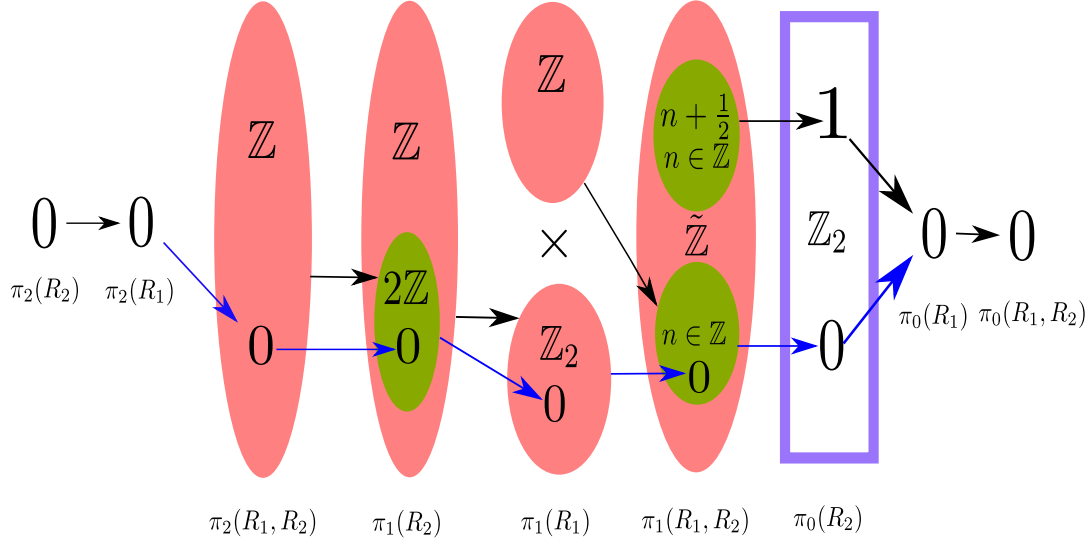


FIGURE 3.2: Illustration of the exact sequence of homomorphisms for $\pi_n(R_1, R_2)$ in Eq. (A.6). This demonstrates that the elements of $\pi_n(R_1, R_2)$ group have two sources: the kernel of the mapping $\pi_{n-1}(R_2) \rightarrow \pi_{n-1}(R_1)$ and the quotient space of $\pi_n(R_1)$ over the image of the mapping $\pi_n(R_2) \rightarrow \pi_n(R_1)$. The black arrows represent the image of homomorphisms, while the blue arrows represent the kernel of every homomorphism. This mapping diagram prescribes the relation between the elements of the composite topological defects. In particular, it shows that the relative homotopy group $\pi_2(R_1, R_2)$ is determined by the kernel of the mapping $\pi_1(R_2) \rightarrow \pi_1(R_1) = 2\mathbb{Z} \cong \mathbb{Z}$. It demonstrates that the nontrivial monopoles are termination points of spin vortices with the total winding number being even. As we will see in next section, this mapping relations is identical with that describing vortex skyrmions. On the other hand, the relative homotopy group $\pi_1(R_1, R_2) \cong \tilde{\mathbb{Z}}$ is determined by both sources: \mathbb{Z}_2 which is the kernel of the homomorphism $\pi_0(R_2) \rightarrow \pi_0(R_1)$ and the quotient group of $\pi_1(R_1)/\text{im } m_*$ with $m_* : \pi_1(R_2) \rightarrow \pi_1(R_1)$. As a result, there are two different kinds of phase vortices, that terminate and do not terminate the KLS wall. Those two classes of vortices consist of the two cosets of quotient $\tilde{\mathbb{Z}}/\mathbb{Z} \cong \mathbb{Z}_2$. Correspondingly, These are the vortices with half-odd integer circulation numbers and the vortices with integer circulation quanta.

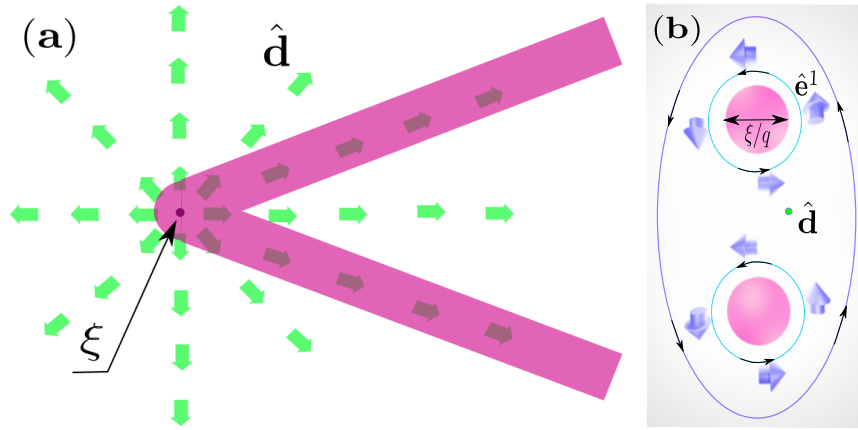


FIGURE 3.3: Illustration of string monopole in the PdB phase. The monopole in the $\hat{\mathbf{d}}$ -field has topological charge $n_2 = 1$ and hard core of the coherence length size ξ (black dot). This string monopole terminates two spin vortices with the soft core size ξ/q and with the total topological charge $n_1 = 1 + 1 = 2 = 2n_2$ according to Eq. (3.8). (a) Texture of $\hat{\mathbf{d}}$ vector string monopole with $n_2 = 1$ terminating two spin vortices. The green arrow corresponds to $\hat{\mathbf{d}}$ vector. The pink region is the soft core of spin vortex of size ξ/q . (b) The cross sections of two spin vortices with $n_1 = 1$ each. The blue arrows represent the $\hat{\mathbf{e}}$ vectors. In these cross sections, $\hat{\mathbf{e}}_1$ and $\hat{\mathbf{e}}_2$ vectors rotate around $\hat{\mathbf{d}}$ vector by 2π for every spin vortex. The core size of every spin vortex is ξ/q . The blue line, which surround two cores of spin vortices, is the field line of $\hat{\mathbf{e}}$ vectors rotation, while the cyan lines, which surround core of every spin vortices, illustrate the winding of $\hat{\mathbf{e}}$ vectors around the core of spin vortex.

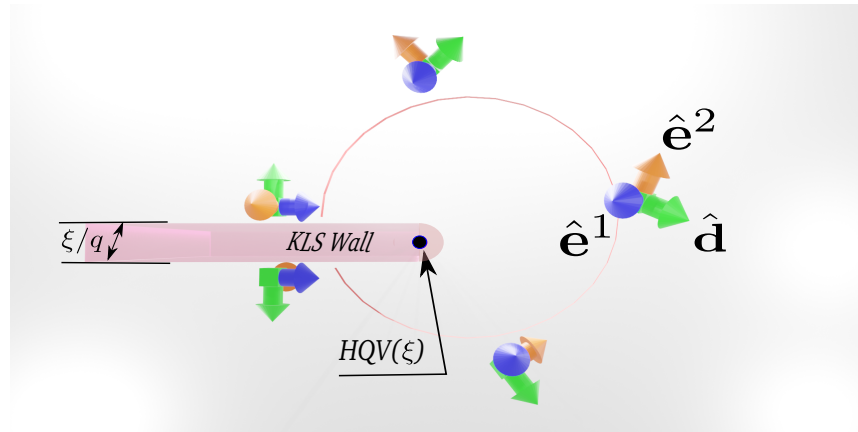


FIGURE 3.4: Illustration of the KLS string wall. The wall itself is topologically protected by $\pi_0(R_2)$ if the order parameter takes values from disconnected parts of R_2 . In the case of two-step successive symmetry breaking, it convert to the combined object – the HQV, which terminates the KLS wall. The pink region is the topological KLS wall with thickness ξ/q , while the black small dot is HQV string, which diameter is ξ . The spin tripods show the configurations of order parameter around the HQVs string. The flipping of the tripods on two sides of KLS wall demonstrates the Domain wall feature.

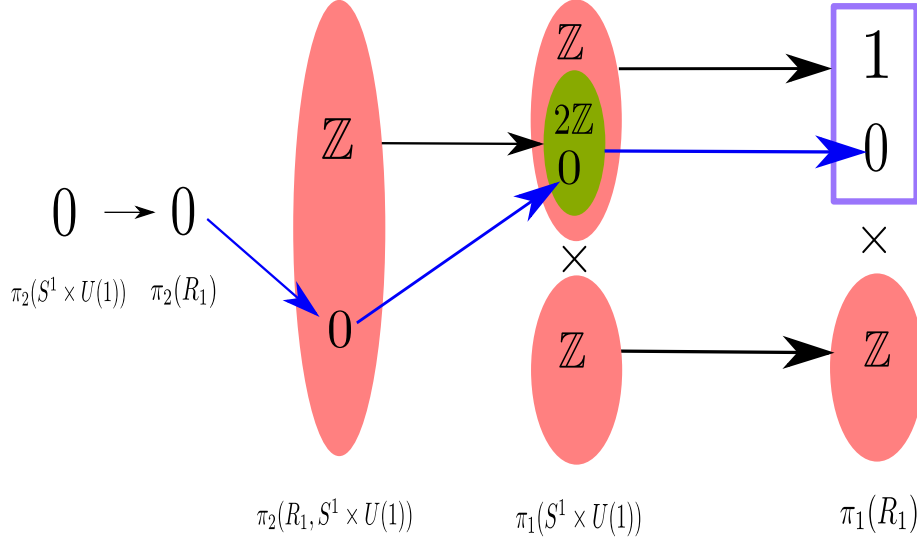


FIGURE 3.5: Mapping diagram of exact sequence between R_1 and $S^1 \times U(1)$. The black arrows represent the image of homomorphisms, while the blue arrows represent the kernel of every homomorphism. This diagram shows that the skyrmions soften the core of \mathbb{Z} spin vortices with size ξ/q to size ξ_H in the presence of magnetic field. In regions larger than ξ_H , vortex skyrmions can be connected with spin vortices via string monopole, if their total topological charge is even according to Eq. (3.13). This is because $\pi_2(R_1, R_2) \cong \pi_2(R_1, S^1 \times U(1))$. There are also phase vortices described by \mathbb{Z} , but here we ignore them because they do not influence the connection between the spin vortices and skyrmions.

(composite) objects are different in the two phases. Similar with the case of string monopole, we recall the SES

$$0 \rightarrow \mathbb{Z} \xrightarrow{i^*} \pi_1(R_1, R_2) \xrightarrow{\partial^*} \mathbb{Z}_2 \rightarrow 0 \quad (3.10)$$

of $\pi_1(R_1, R_2)$ to demonstrate the details of KLS string wall (calculation details see Appendix. A.2). Because the image of boundary homomorphism ∂^* is $\pi_0(R_2) = \mathbb{Z}_2$, there are two kinds of string defects in the vicinity of the second time symmetry breaking. One is free vortex with integer winding number $n \in \mathbb{Z}$, while the other one is vortex with half-odd integers, $k = n + 1/2$, terminate the wall bounded by string – the KLS string wall. Thus we can see from Fig. 3.2 and Eq. (3.10) the $\text{im } i^*$ of SES of $\pi_1(R_1, R_2)$ are vortices of integer winding number because of $\text{im } i^* \cong \ker \partial^*$.

Fig. 3.4 illustrates the configuration of the composite object. This kind of topologically protected KLS string wall induces the cosmological catastrophe in the axion solution of strong CP problem [76–87].

3.3 Skyrmions and Nexus in the presence of magnetic field

In the presence of magnetic field \mathbf{H} , a new length scale appears in the PdB phase – the magnetic length $\xi_H \propto |\mathbf{H}|^{-1}$. The magnetic length ξ_H is the longest length scale if we neglect the spin-orbit coupling. As a result, we have the order parameter

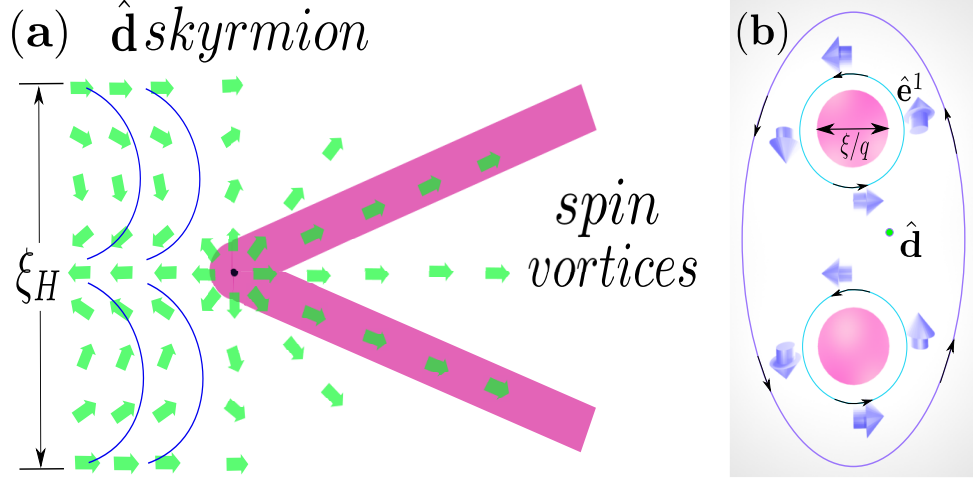


FIGURE 3.6: Illustration of nexus object in presence of magnetic field. The nexus connects spin vortices with core size ξ/q and the vortex skyrmion with core size ξ_H , where $\xi_H \gg \xi/q$. (a) the texture configuration of nexus object with $n_2 = 1$ and $n_1 = 2$. The green arrows are the $\hat{\mathbf{d}}$ vectors and the pink regions are core regions of defects. The black dot is the core of string monopole with size ξ , while the pink regions are the cores of spin vortices with size ξ/q . The green arrows represent the distribution of $\hat{\mathbf{d}}$ vectors. The vortex skyrmion with core size ξ_H transforms to two spin vortices via nexus. (b) the cross section of two spin vortices. Every spin vortex has the 2π rotation of $\hat{\mathbf{e}}^1$ and $\hat{\mathbf{e}}^2$ vectors around fixed $\hat{\mathbf{d}}$ vector. The blue arrows represent the field of the $\hat{\mathbf{e}}^1$ vector.

vacuum manifold R_1 at short distances where the magnetic energy can be neglected, and a submanifold $R_1^H \subset R_1$ at large distances ($> \xi_H$), where the space of the order parameter is restricted by magnetic interaction [91, 101, 123, 124]. In the region with length scale larger than ξ_H , the magnetic anisotropy locks the directions of $\hat{\mathbf{d}}$ vector in the plane perpendicular to \mathbf{H} to minimize the magnetic energy, which is proportional to $|\mathbf{H} \cdot \hat{\mathbf{d}}|^2$. The degenerate space of the order parameter is reduced from $R_1 = SO_{S-L}(3) \times U(1)$ in Eq. (2.13) to $R_1^H = S^1 \times S^1 \times U(1)$ in the regions larger than ξ_H . The first S^1 is the manifold of in plane $\hat{\mathbf{d}}$ vector, while the second S^1 is the manifold of rotations of $\hat{\mathbf{e}}^1$ and $\hat{\mathbf{e}}^2$ about the $\hat{\mathbf{d}}$ -axis. However, for $q \ll 1$, the gradient energy of the $\hat{\mathbf{d}}$ -textures is much larger than that of the textures in $\hat{\mathbf{e}}^1$ and $\hat{\mathbf{e}}^2$ fields and intensively increase the free energy of system [94]. That is why we consider only the S^1 manifold of $\hat{\mathbf{e}}^1$ and $\hat{\mathbf{e}}^2$, and neglect the S^1 manifold of $\hat{\mathbf{d}}$. Then the relative second homotopy group which we need in this case is

$$\pi_2(R_1, S^1 \times U(1)) = \mathbb{Z}. \quad (3.11)$$

The results for the relative homotopy group have been confirmed by calculations using the exact sequence, see details in appendices Sec. A.2.2. The mapping diagram of LES of $\pi_2(R_1, S^1 \times U(1))$ i.e., Eq. (A.9) is shown in Fig. 3.5.

Following the convention in Sec. 3.2, we introduce the SES (for details see Appendix. A.2.2)

$$0 \rightarrow 0 \xrightarrow{i^*} \pi_2(R_1, S^1 \times U(1)) \xrightarrow{\partial^*} 2\mathbb{Z} \rightarrow 0 \quad (3.12)$$

of $\pi_2(R_1, S^1 \times U(1))$ to discuss the corresponding topological objects. Because the $im\partial^* \cong 2\mathbb{Z}^S \subset \pi_1(S^1 \times U(1))$, this kind of object has spin vortices with even winding number on its boundary. As a result, the object described by $\pi_2(R_1, S^1 \times U(1))$ is the vortex skyrmion in the presence of magnetic field, which has the soft core of size ξ_H represented as skyrmion, see Fig. 3.6. The topological charge of skyrmion is

$$n_2 = \frac{1}{8\pi} e^{ijk} \int_{D_2} dS_k \hat{\mathbf{d}} \cdot (\nabla_i \hat{\mathbf{d}} \times \nabla_j \hat{\mathbf{d}}) = \frac{1}{2} n_1, \quad (3.13)$$

where $n_2 \in \pi_2(R_1, S^1 \times U(1))$, D_2 is the cross-section of skyrmion and n_1 is the winding number of spin vortices in Eq. (2.17).

The Eq. (3.13) is the analog of the Mermin-Ho relation in $^3\text{He-A}$ [125]. However, there is a more prominent feature of this relation, that is Eq. (3.13) is identical with Eq. (3.8). In fact, the SESes of $\pi_2(R_1, R_2)$ in Eq. (3.10) and $\pi_2(R_1, S^1 \times U(1))$ in Eq. (3.12) are exactly same as well. This means

$$\pi_2(R_1, S^1 \times U(1)) \cong \pi_2(R_1, R_2). \quad (3.14)$$

As a result, their topological invariants are same. Due to this relation the vortex skyrmion can be connected to \mathbb{Z} spin vortices with core size ξ/q via the string monopole. Such composite objects, where the monopole connects several linear objects with different characteristic length scales is called nexus. It demonstrates the interplay between π_1 and π_2 topologies. In spite of its novel and complicated structure, nexus actually connect topological objects with different characteristic energies in a topological protected binding in Eq. (3.14). This property allow researchers to detect topological objects with small length scale via low energy dynamic process. We will see this in next two chapters.

Originally vortex skyrmions formed by orbital and phase degenerate parameters have been suggested in $^3\text{He-A}$ by Anderson and Toulouse [126] and by Chechetkin [127]. The lattice of vortex-skyrmions in rotating $^3\text{He-A}$ has been discussed in Ref. [128]. These objects have been identified in different experiments under rotation [129, 130]. The dynamics of the vortex skyrmions provides an effective electromagnetic fields, which induces the observed effect of chiral anomaly experienced by fermionic excitations (Weyl fermions) living in the soft core of a vortex skyrmion [131].

Chapter 4

Equilibrium Configurations of the Extended Structures of KLS String Wall

As we have seen in last section of Chapter. 3, the orientation energies with different characteristic lengths reduce the vacuum manifolds and generate nexus, which connects topological objects with different characteristic energies. In this chapter, we discuss how this mechanism runs for one dimensional nexus when we take into account the dipole energy — the smallest orientation energy in superfluid ^3He . We will see the KLS string wall with length scale ξ and ξ/q connect to spin solitons with dipole length $\xi_D \gg \xi/q$ via HQV. The possible mesoscopic equilibrium state configurations are analyzed and numerically calculated. The resulted data will be directly used for spin dynamic response calculations in Chapter. 5 and compare with the experimental observations.

4.1 Vacuum manifolds in the presence of orientation energies

The PdB phase achieved by two step successive symmetry breaking phase transition, which starts from uniaxial anisotropy normal phase vacuum, has two well separated length scales ξ and ξ/q in the vicinity of transition from polar phase to PdB phase [97]. In the Chapter. 2, we discussed the vacua of order parameters of superfluid in the nafen-distorted ^3He . These vacua have dramatically different characteristic lengths determined by the energy gaps. As a result, the PdB phase in the vicinity of transition from polar phase to PdB phase has several composite topological objects with different dimensions. These novel composite objects are classified by relative homotopy groups $\pi_n(R_1, R_2)$ between vacua R_1 and R_2 . Because of fibration in Eq. (3.3), the stable objects of polar phase are stabilized again in PdB phase by forming composite objects described by relative homotopy groups $\pi_n(R_1, R_2)$. However, objects with length scales around ξ or ξ/q have higher characteristic energies than the energy scale of typical detecting method i.e., Nuclear Magnetic Resonance (NMR). In the experiment in Ref. [74], the detection of KLS string wall was done by NMR of spin solitons, which connect with KLS domain wall via HQV. Thus HQV is one dimensional (1D) nexus and KLS string wall extends its structure into mesoscopic length scale via 1D nexus. In this section, we discuss the orientation energies, their corresponding characteristic lengths and the reduced vacuum manifolds, which make this detection possible.

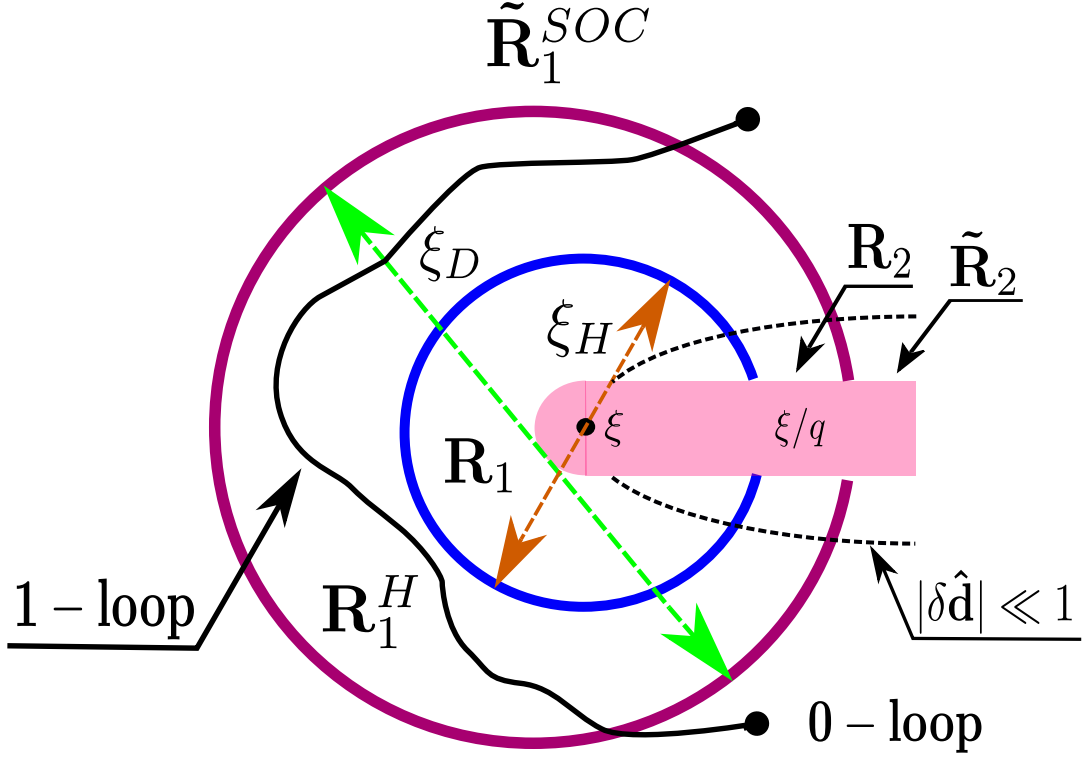


FIGURE 4.1: Illustration of vacuum manifolds with length scales $\xi_H < r < \xi_D$ and $r > \xi_D$ in the vicinity of transition from polar phase to PdB phase. As been discussed in Ref. [97], the vacuum manifolds of PdB in the vicinity of the second symmetry breaking are R_1 and R_2 in the region with $r < \xi_H$. The hierarchy of length scales extends in the presence of magnetic energy and SOC energy. We have known there is KLS string wall described by $\pi_1(R_1, R_2) \cong \mathbb{Z}$ for $r < \xi_H$. In larger region with length scale $\xi_H < r < \xi_D$, R_1 reduces to $R_1^H = S_5^1 \times U(1)^\Phi$ by magnetic energy. To minimize the magnetic energy, spin vector $\hat{\mathbf{d}}$ is perpendicular to static magnetic field $\mathbf{H}^{(0)}$, while the R_2 is unchanged. When the SOC energy is taken into account, R_1^H further reduces to $\tilde{R}_1^{SOC} = R_s^{SOC} \times U(1)^\Phi$ and R_2 reduces to $\tilde{R}_2 = \mathbb{Z}_2^{S-\Phi}$. As a results, there are linear topological objects described by $\pi_1(R_1^H, \tilde{R}_1^{SOC})$, in which the relative 1-loop (black solid curve) is mapped to R_1^H while its end points 0-loop is mapped to \tilde{R}_1^{SOC} .

In nafen-distorted ^3He system, these length scales are magnetic length ζ_H and dipole length ζ_D [35, 73, 94]. These two length scales are healing lengths and characterize the spatial ranges in which the gradient energy are larger than orientations energies. When the length scale of spatial variations is larger than these characteristic lengths, the vacuum manifolds are reduced to minimize the orientation energies. We discussed the consequence of this kinds of reduction by magnetic energy and magnetic length ζ_H i.e., the vortex skyrmions in Chapter. 3. We will see there are more interesting results when dipole length ζ_D is introduced in addition to ζ_H in rest parts of this review. ζ_H is determined by gradient energy density

$$f_{\text{grad}} = \frac{1}{2}K_1\partial_i A_{\alpha j}\partial_i A_{\alpha j}^* + \frac{1}{2}K_2\partial_j A_{\alpha i}\partial_i A_{\alpha j}^* + \frac{1}{2}K_3\partial_i A_{\alpha i}\partial_j A_{\alpha j}^* \quad (4.1)$$

where

$$A_{\alpha i} \equiv A_{\alpha i}^{\text{PdB}} = e^{i\Phi}[\Delta_P \hat{d}_\alpha \hat{z}_i + \Delta_{\perp 1} \hat{e}_\alpha^1 \hat{x}_i + \Delta_{\perp 2} \hat{e}_\alpha^2 \hat{y}_i] \quad (4.2)$$

is the order parameter of PdB phase. $\hat{\mathbf{d}} \equiv \hat{d}_\alpha$ and $\hat{\mathbf{e}}^{1(2)} \equiv \hat{e}_\alpha^{1(2)}$ are the spin degenerate parameters and they form the triad in spin space. Φ and $\hat{x}_i \equiv \hat{x}, \hat{y}_i \equiv \hat{y}, \hat{z}_i \equiv \hat{z}$ are phase and orbital degenerate parameters respectively. Here $|\Delta_{\perp 1}| = |\Delta_{\perp 2}| = |q|\Delta_P$ with $|q| \leq 1$, and $K_1 = K_2 = K_3$ [94]. The magnetic energy density is

$$f_H = -\frac{1}{2}\chi_{\alpha\beta}H_\alpha H_\beta = \frac{1}{2}\gamma^2 S_a S_b (\chi^{-1})_{ab} - \gamma H_a S_a, \quad (4.3)$$

here the $\chi_{\alpha\beta}$ is uniaxial tensor of magnetic susceptibility of PdB phase, H_α are magnetic field strengths with $\alpha = 1, 2, 3$, S_a are spin densities with $a = 1, 2, 3$ and γ is gyromagnetic ratio [94]. With the help of Eq. (4.1) and Eq. (4.3), the magnetic length is given as

$$\zeta_H = \left[\frac{K_1 \Delta_P^2}{(\chi_\perp - \chi_\parallel) H^2} \right]^{\frac{1}{2}}, \quad (4.4)$$

where χ_\perp and χ_\parallel are transverse and longitude spin magnetic susceptibilities of PdB phase. In the experiment, a static magnetic field $\mathbf{H}^{(0)}$ with fixed direction is turned on [74]. Then the degenerate space of PdB order parameter reduces to

$$R_1^H = S^1 \times U(1)^\Phi \quad (4.5)$$

from R_1 in the region where length scale of spatial variation is larger than ζ_H , as we discussed in Sec. 3.3. Because the magnetic energy locks the $\hat{\mathbf{d}}$ vector into the plane perpendicular to $\mathbf{H}^{(0)}$, R_2 keeps the same form as it is inside the region with length scale ζ_H . Then we still have $R_2 = SO(2)_{S-L} \times \mathbb{Z}_2^{S-\Phi}$ in the region where condition $|\delta\hat{\mathbf{d}}| \ll 1$ is satisfied. In Fig. 4.1, we illustrate the R_1^H and ζ_H in the presence of KLS string wall.

Following the same idea, the dipole length ζ_D is determined by gradient energy density f_{grad} and SOC energy density

$$f_{\text{soc}} = \frac{3}{5}g_D(A_{ii}^* A_{jj} + A_{ij}^* A_{ji} - \frac{2}{3}A_{ij}^* A_{ij}), \quad (4.6)$$

where g_D is strength of spin orbital coupling. Then we have

$$\zeta_D = \left(\frac{5K_1}{6g_D}\right)^{\frac{1}{2}}. \quad (4.7)$$

When the Spin-Orbit coupling (SOC) is taken into account, vacuum manifolds of order parameters are further reduced from R_1^H and R_2 . In general consideration, the requirement of minimizing SOC energy in region with length scale larger than ζ_D fixes the relative directions between spin vectors and orbital vectors. The resulted vacuum manifold always could be represented by spin degree of freedom because the broken symmetry is relative symmetry [94]. Thus R_1^H reduces to

$$\tilde{R}_1^{SOC} = R_S^{SOC} \times U(1)^\Phi \quad (4.8)$$

in the region with length scale larger than ζ_D , where R_S^{SOC} is the reduced vacuum manifold of spin degree of freedom. In general case, R_S^{SOC} is a complicated space. However R_S^{SOC} may be simplified by using parametrization of $\hat{\mathbf{d}}$ and $\hat{\mathbf{e}}^{1(2)}$ vectors of $A_{\alpha i}^{pdB}$. To facilitate comparison between experimental observations and our theoretical analysis, the parametrizations

$$\hat{\mathbf{d}} = \hat{x}\cos\theta - \hat{z}\sin\theta, \quad \hat{\mathbf{e}}^1 = -\hat{x}\sin\theta - \hat{z}\cos\theta, \quad \hat{\mathbf{e}}^2 = \hat{y}, \quad \mathbf{H}^{(0)} = H\hat{y} \quad (4.9)$$

would be used in this work, where θ is the angle between $\hat{\mathbf{d}}$ and local orbital-coordinate frame [74]. In this case, we find

$$R_S^{SOC} = \{\theta_0, \pi - \theta_0, -\theta_0, \pi + \theta_0\}, \quad (4.10)$$

where $\theta_0 = \arcsin[q/(1 - |q|)]$. There is a discrete symmetry for free energy of system and this discrete symmetry turns out to be the mirror symmetry between parametrization in Eq. (4.9) and the alternative in the presence of KLS domain wall. We discuss the details of this discrete symmetry and its violation in Sec. 4.4. Before that, we mainly use the parametrization in Eq. (4.9). In the region where condition $|\delta\hat{\mathbf{d}}| \ll 1$ is satisfied, SOC energy fixes the relative rotation of $SO(2)_{S-L}$, thus R_2 reduces to

$$\tilde{R}_2 = \mathbb{Z}_2^{S-\Phi} \quad (4.11)$$

in the region with length scale larger than ζ_D .

From illustration of R_1^H , \tilde{R}_1^{SOC} and \tilde{R}_2 in Fig. 4.1, we find again the possibility of utilizing the relative homotopy group to investigate the novel topological objects because of the presence of multiple characteristic length scales [107]. This multilength-scales system belongs to type (i) of the classifications in Ref. [97]. Recently, other example of this class is solitons terminated by HQVs observed in spinor Bose condensate with quadratic Zeeman energy [123, 124]. Both of these systems can be described by the first relative homotopy group. In next section, we discuss this topic.

4.2 1D nexus objects and spin solitons

4.2.1 Spin configuration of KLS string wall – half spin vortices

In the region with length scale $\xi_H \leq r \leq \xi_D$, we have the long exact sequence (LES) of homomorphism of $\pi_1(R_1^H, R_2)$ (for the details of LES, see Appendix. A.1)

$$\begin{array}{ccccccc} \pi_1(R_2) & \xrightarrow{i^*} & \pi_1(R_1^H) & \xrightarrow{j^*} & \pi_1(R_1^H, R_2) & \xrightarrow{\partial^*} & \pi_0(R_2) \xrightarrow{k^*} \pi_0(R_1^H), \\ | & & | & & | & & | \\ \mathbb{Z}^S & \xrightarrow{i^*} & \mathbb{Z}^S \times \mathbb{Z}^\Phi & \xrightarrow{j^*} & \pi_1(R_1^H, R_2) & \xrightarrow{\partial^*} & \mathbb{Z}_2 \xrightarrow{k^*} 0 \end{array} \quad (4.12)$$

where i^* projects spin vortices of $\pi_1(R_2)$ to the spin vortices of $\pi_1(R_1^H)$ [107, 112]. And boundary homomorphism ∂^* maps all relative 1-loops of $\pi_1(R_1^H, R_2)$ to their 0-loops of $\pi_0(R_2)$. Because $\pi_0(R_2) = \mathbb{Z}_2$, the end-points of relative 1-loop may take values from connected or disconnected subsets of R_2 . This LES can be split to the short exact sequence (SES)

$$0 \rightarrow \mathbb{Z}^\Phi \xrightarrow{\iota} \pi_1(R_1^H, R_2) \xrightarrow{\pi} \mathbb{Z}_2 \rightarrow 0, \quad (4.13)$$

where ι and π are inclusion and surjection respectively. Eq. (4.13) suggests

$$\pi_1(R_1^H, R_2) \cong \tilde{\mathbb{Z}}, \quad (4.14)$$

which is isomorphic to $\pi_1(R_1, R_2)$ in the region smaller than ξ_H [97]. This means KLS string wall, which determined by two length scales ξ and ξ/q in two-step phase transition, extends into the region with length scale $\xi_H \leq r \leq \xi_D$. However Eq. (4.13) only contains degree of freedom (DOF) of phase factor Φ , all information about spin degree of freedom lose because they are trivial elements of $\pi_1(R_1^H, R_2)$. To understand the spin part of KLS string wall, we should take account the continuity of order parameter. The continuity of order parameter $A_{\alpha i}^{PdB}$ requires spin vectors simultaneously change by $(2n+1)\pi$ in the present of KLS string wall [132]. This consideration suggests that the spin textures of KLS string wall in the spatial region with length scale $\xi_H \leq r \leq \xi_D$ are classified by group

$$M \equiv \{n^s/2 | n^s \in \mathbb{Z}\}, \quad (4.15)$$

such that $M/\pi_1(S_1^1) \cong \mathbb{Z}_2 = \{[0], [1/2]\}$. The cosets $[1/2]$ and $[0]$ correspond to the presence or absence of the KLS string wall in the region $\xi_H < r \leq \xi_D$ respectively. Coset $[0] \cong 2\mathbb{Z}$ contains all free spin vortices. While Coset $[1/2] \cong \{n+1/2 | n \in \mathbb{Z}\}$ contains all spin vortices with half-odd winding number i.e., it is set of half spin vortices.

4.2.2 Spin soliton described by $\pi_1(R_1^H, \tilde{R}_1^{SOC})$

When taking into account SOC, R_1^H reduces to $\tilde{R}_1^{SOC} = R_1^{SOC} \times U(1)$ as mentioned in Sec. 4.1. As a result, there are linear objects which classified by $\pi_1(R_1^H, \tilde{R}_1^{SOC})$. $\pi_1(R_1^H, \tilde{R}_1^{SOC})$ has LES

$$\begin{array}{ccccccc} \pi_1(\tilde{R}_1^{SOC}) & \xrightarrow{i^*} & \pi_1(R_1^H) & \xrightarrow{j^*} & \pi_1(R_1^H, \tilde{R}_1^{SOC}) & \xrightarrow{\partial^*} & \pi_0(\tilde{R}_1^{SOC}) \xrightarrow{k^*} \pi_0(R_1^H), \\ | & & | & & | & & | \\ \mathbb{Z}^\Phi & \xrightarrow{i^*} & \mathbb{Z}^S \times \mathbb{Z}^\Phi & \xrightarrow{j^*} & \pi_1(R_1^H, \tilde{R}_1^{SOC}) & \xrightarrow{\partial^*} & \mathbb{Z}_4 \xrightarrow{k^*} 0 \end{array} \quad (4.16)$$

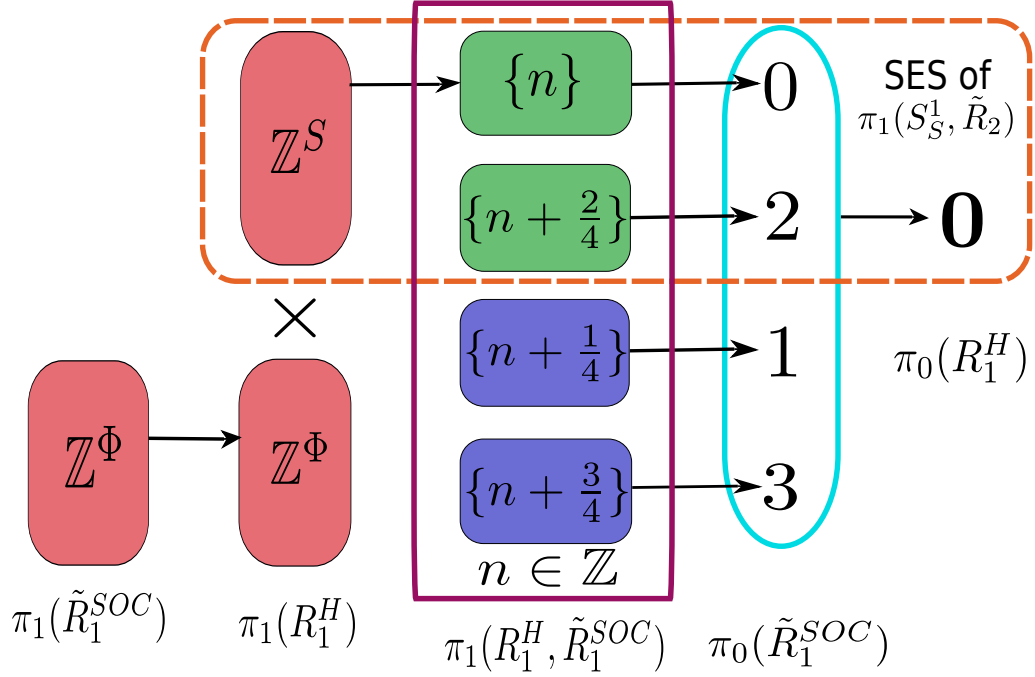


FIGURE 4.2: Illustrations of LES of homomorphism for $\pi_1(R_1^H, \tilde{R}_1^{SOC})$ and short exact sequence of homomorphism for $\pi_1(S_S^1, \tilde{R}_2)$. The black arrows represent the image of homomorphisms between homotopy groups. This mapping diagram demonstrates the linear objects of $\pi_1(R_1^H, \tilde{R}_1^{SOC})$ are spin solitons. This is because the mapping between $\pi_1(\tilde{R}_1^{SOC})$ and $\pi_1(R_1^H)$ is projection, the image of homomorphism $i^* : \pi_1(\tilde{R}_1^{SOC}) \rightarrow \pi_1(R_1^H) = \mathbb{Z}^\Phi$ i.e., topological invariant of all phase vortices. As a result, the trivial linear objects of $\pi_1(R_1^H, \tilde{R}_1^{SOC})$ are all phase vortices because of $\text{im } i^* \cong \ker j^*$. We found there are one kind of spin vortices and three kinds of spin solitons because $\ker k^* \cong \text{im } \partial^* = \mathbb{Z}_4$ and j^* is projection. Moreover, we found from this illustration that the subgroup $G = \{[n], [n + 2/4]\}$ of $\pi_1(R_1^H, \tilde{R}_1^{SOC})$ is extension of \mathbb{Z}^S by $\pi_0(\tilde{R}_2^{SOC}) = \mathbb{Z}_2$ and then isomorphic to M . In the orange dash line panel, we shows the corresponding SES of G . As a result, HQV is 1D nexus between spin soliton of coset $[2/4]$ and KLS domain wall in PdB phase.

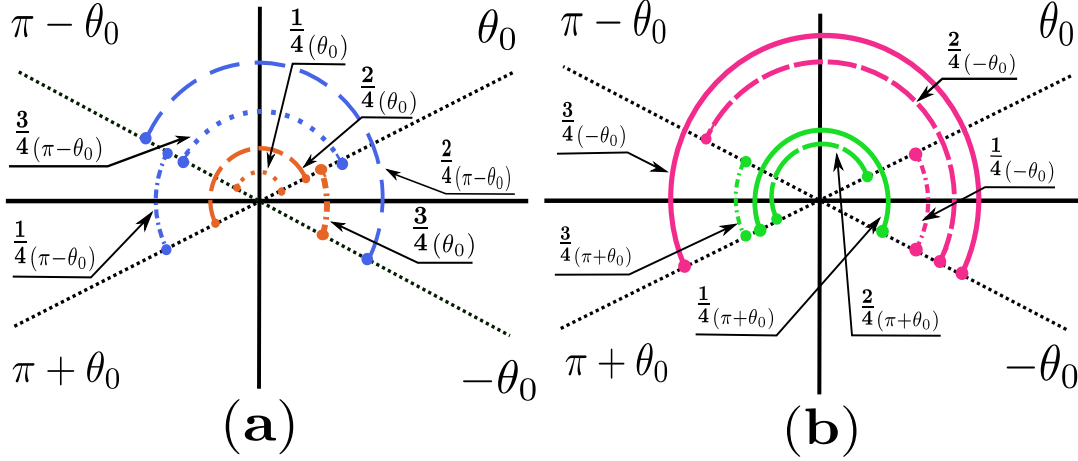


FIGURE 4.3: Illustrations of three kinds of spin solitons of $\pi_1(S_S^1, R_S^{SOC})$. The black dot lines represent the four elements of R_S^{SOC} i.e., $\pm\theta_0$ and $\pi \pm \theta_0$. The dash line, dot line, dash-dot line and solid line correspond to π -soliton ($|\Delta\theta| = \pi$), soliton ($|\Delta\theta| = \pi - 2\theta_0$), KLS-Soliton ($|\Delta\theta| = 2\theta_0$) and big-soliton ($|\Delta\theta| = \pi + 2\theta_0$) respectively. (a) Spin solitons with topological invariants $1/4$, $2/4$ and $3/4$ for θ_0 (orange) and $\pi - \theta_0$ (blue) respective. (b) Spin solitons with topological invariants $1/4$, $2/4$ and $3/4$ for $-\theta_0$ (pink) and $\pi + \theta_0$ (green) respective.

where i^* is projection and ∂^* is boundary homomorphism [107, 112, 133]. Figure 4.2 depicts the mapping relation of Eq. (4.16). The relative 1-loop of $\pi_1(R_1^H, \tilde{R}_1^{SOC})$ and the boundary 0-loop are shown in Fig. 4.1. Because $\text{im } \partial^* \cong \ker k^* = \mathbb{Z}_4$, the boundary 0-loop (two end points) of 1-loop takes values from four disconnected subsets of \tilde{R}_1^{SOC} . For every element of \tilde{R}_1^{SOC} , there are four possible combinations of elements of \tilde{R}_1^{SOC} for 0-loop because of $\pi_0(\tilde{R}_1^{SOC}) = \mathbb{Z}_4$. As a result, we found there are four kinds of linear objects in general, which might be distinguished by four boundary homotopy classes of $\pi_0(\tilde{R}_1^{SOC})$.

Now we split the LES in Eq. (4.16) into SES (see details in Sec. A.1)

$$0 \rightarrow \mathbb{Z}^S \xrightarrow{i^*} \pi_1(R_1^H, \tilde{R}_1^{SOC}) \xrightarrow{\partial^*} \mathbb{Z}_4 \rightarrow 0. \quad (4.17)$$

Then we find

$$\pi_1(R_1^H, \tilde{R}_1^{SOC}) = \{n^S / 4 | n^S \in \mathbb{Z}\} \cong \mathbb{Z}, \quad (4.18)$$

such that

$$\pi_1(R_1^H, \tilde{R}_1^{SOC}) / \mathbb{Z}^S \cong \mathbb{Z}_4. \quad (4.19)$$

Because Eq. (4.17) is merely determined by $\mathbb{Z}^S = \pi_1(S_S^1)$ and $\mathbb{Z}_4 = \pi_0(R_S^{SOC})$, $\pi_1(R_1^H, \tilde{R}_1^{SOC})$ actually is isomorphic to $\pi_1(S_S^1, R_S^{SOC})$ i.e.,

$$\pi_1(R_1^H, \tilde{R}_1^{SOC}) \cong \pi_1(S_S^1, R_S^{SOC}). \quad (4.20)$$

This means the linear objects classified by $\pi_1(R_1^H, \tilde{R}_1^{SOC})$ are spin solitons and spin vortices [133, 134]. And the four cosets of $\pi_1(S_S^1, R_S^{SOC})$ are

$$[0] = \{n^S\}, \left[\frac{1}{4}\right] = \{n^S + \frac{1}{4}\}, \left[\frac{2}{4}\right] = \{n^S + \frac{2}{4}\}, \left[\frac{3}{4}\right] = \{n^S + \frac{3}{4}\}. \quad (4.21)$$

These cosets give out the topological invariants of the four different kinds of linear objects distinguished by four classes of boundary 0-loop of $\pi_0(R_S^{SOC})$. They correspond to free spin vortices and three kinds of spin solitons respectively. Figure. 4.3 shows the representatives of the three classes of spin solitons for every element of R_S^{SOC} . We omit the spin vortices of $[0]$ from now because it is not energy-favored. From Fig. 4.3, we found there are four types of spin solitons distinguished by $|\Delta\theta|$. Following the terminologies in Ref. [74], they are big-soliton ($|\Delta\theta| = \pi + 2\theta_0$), soliton ($|\Delta\theta| = \pi - 2\theta_0$), KLS-soliton ($|\Delta\theta| = 2\theta_0$) and π -soliton ($|\Delta\theta| = \pi$). To avoid terminological confusion, we claim here that we use phrase "spin soliton" to denote spin textures of $\pi_1(S_S^1, R_S^{SOC})$ in rest of this review, while use phrases "solitons", "big-solitons", "KLS-solitons" and " π -solitons" to denote particular spin textures with different $|\Delta\theta|$.

4.2.3 Short exact sequence of $\pi_1(S_S^1, \tilde{R}_2)$ and 1D nexus

A significant property of $\pi_1(S_S^1, R_S^{SOC})$ is that it has a subgroup $G \equiv \{[0], [2/4]\}$ such that $G/\mathbb{Z}^S \cong \mathbb{Z}_2$. The SES of G is given as

$$0 \rightarrow \mathbb{Z}^S \rightarrow G \xrightarrow{\partial^*} \mathbb{Z}_2 \rightarrow 0 \quad (4.22)$$

by Eq. (4.17). The mapping diagram of Eq. (4.22) is shown in the dash panel of Fig. 4.2. Because $\pi_0(\tilde{R}_2) \cong \mathbb{Z}_2$, Eq. (4.22) can be written as

$$\pi_1(\tilde{R}_2) \rightarrow \pi_1(S_S^1) \rightarrow G \xrightarrow{\partial^*} \pi_0(\tilde{R}_2) \rightarrow 0. \quad (4.23)$$

This LES suggests

$$G = \pi_1(S_S^1, \tilde{R}_2) \cong \hat{\mathbb{Z}} = M, \quad (4.24)$$

here $\hat{\mathbb{Z}} \equiv \{n^S/2 | n^S \in \mathbb{Z}\}$.

Eq. (4.24) is one of main results in this chapter. This relation means spin solitons, which are classified by coset $[2/4]$ of $\pi_1(S_S^1, \tilde{R}_2)$ can continuously transform to half spin vortices of M . In other word, KLS domain wall smoothly connects to $[2/4]$ spin soliton via HQV. Similar with 2D nexus which connects string monopole and vortex skyrmion, the HQV is 1D nexus which connects KLS domain wall and $[2/4]$ spin soliton [97]. The composite object formed by $[2/4]$ spin soliton and KLS domain wall is then named as 1D nexus object.

4.2.4 Two different configurations of 1D nexus object – separable and inseparable

Because $\pi_1(S_S^1, R_S^{SOC})/\mathbb{Z}^S \cong \mathbb{Z}_4$, we have $[2/4] = [1/4] + [1/4]$. Thus $\pi_1(S_S^1, \tilde{R}_2)$ could also be represented as $\{[0], [1/4] + [1/4]\}$ besides $\pi_1(S_S^1, \tilde{R}_2) \cong \{[0], [2/4]\}$. This means there are two kinds of spin soliton configurations connecting with KLS domain wall via HQV for a given element of $\pi_1(S_S^1, \tilde{R}_2)$. When the topological invariant is literally $2/4$, the spin soliton is spatially inseparable π -soliton in Fig. 4.3. The illustration of configuration of this kind of 1D nexus object is shown in Fig. 4.4(a).

When the topological invariant is $1/4 + 1/4$, the spin soliton is combination of two spatially separable spin solitons with topological invariant $1/4$. In order to identify these two spatially separable spin solitons, we take in account the requirement

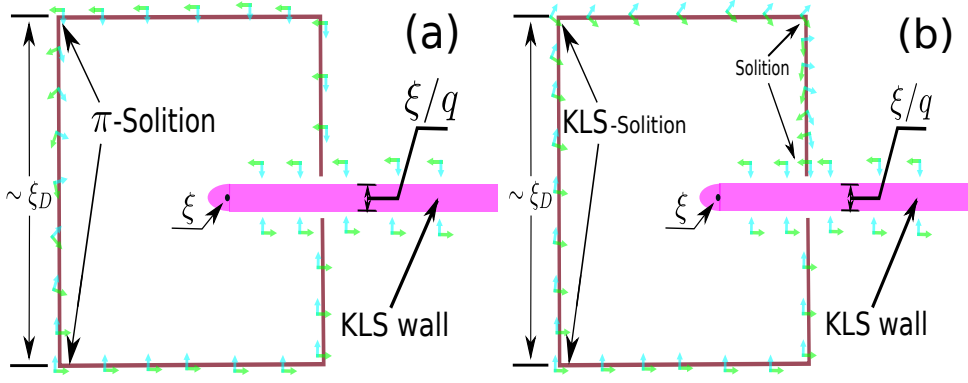


FIGURE 4.4: Illustrations of two dramatically different spin configurations of 1D nexus object, which consists of spin solitons, HQV and KLS domain wall. The green and cyan arrows represent the $\hat{\mathbf{d}}$ and $\hat{\mathbf{e}}$ vectors respectively. (a) Configuration of inseparable spin soliton. In this configuration, the topological invariant of spin soliton is literally $1/2$, which corresponds to π -soliton. In contrast, there are (b) two spin solitons with topological invariant $1/4$ when the group $\pi_1(S^1_S, \tilde{R}_2)$ is implemented in alternative way. Following the requirement of continuity of order parameter, these two spin solitons are KLS-soliton ($\Delta\theta = 2\theta_0$) and soliton ($\Delta\theta = \pi - 2\theta_0$).

of continuity of the order parameters. This requirement is equivalent to the requirement of single-value and continuity of θ . Then the accumulation of $|\Delta\theta|$ of those two spin solitons must equal to π because of the KLS domain wall. Based on the discussions of Sec. 4.2.2 and Fig. 4.3, These two spatially separated spin solitons are KLS-soliton ($|\Delta\theta| = 2\theta_0$) and soliton ($|\Delta\theta| = \pi - 2\theta_0$). As illustrated in Fig. 4.4(b), the 1D nexus object contain two spin solitons in this case.

We will see these two dramatically different spin textures of 1D nexus objects have different equilibrium free energies, different spin dynamic response properties and different NMR frequency shifts in Sec. 4.3 and Sec. 5.2. These properties help us to identify the objects which be observed in experiment.

4.3 Equilibrium textures of pseudo-random lattices

For the PdB phase generated from symmetry breaking of nonuniform polar phase, we can use the Ginzburg-Landau model to describe the system when $|q|$ is small enough. The Ginzburg-Landau (GL) free energy consists of gradient energy and orientation energies [94]. In order to quantitatively analyze the equilibrium configurations of 1D nexus objects containing spin solitons with length scale around ξ_D , we must find out the extreme point of GL free energy under given external parameters.

Because $\xi_D \gg \xi$ and the strongly uniaxial anisotropy in the presence of nafen strands, we actually did this procedure under London limit [94, 133, 135, 136]. In London limit, all gap parameters attain equilibrium structures and then their magnitudes are constants over whole calculations. This means the HQV and KLS domain wall both achieve their equilibrium structure and the contributions to free energy from them are identical constant for both spin configurations of 1D nexus objects. When the static magnetic field $\mathbf{H}^{(0)}$ is big enough, the magnetic length ξ_H is far

smaller than the dipole length ζ_D , then the magnetic energy has achieved equilibrium over the PdB superfluid as well. In this situation the Ginzburg-Landau free energy in London limit is

$$F_{London} = \int_{\Sigma} (f_{soc} + f_{grad}) d\Sigma, \quad (4.25)$$

where Σ is the volume of the PdB phase sample.

Plunging $A_{\alpha i}^{PdB}$ into Eq. (4.25) and substituting $\hat{\mathbf{d}}$, $\hat{\mathbf{e}}^1$ and $\hat{\mathbf{e}}^2$ with their parametrizations in Eq. (4.9), we get the gradient energy density and SOC energy density in term of θ and Φ

$$\begin{aligned} f_{grad}(\Phi, \theta) &= \frac{K_1}{2} (\Delta_P^2 + \Delta_{\perp 1}^2 + \Delta_{\perp 2}^2) \partial_i \Phi \partial_i \Phi + \frac{K_1}{2} (\Delta_P^2 + \Delta_{\perp 1}^2) \partial_i \theta \partial_i \theta \\ &\quad + \frac{1}{2} (K_2 + K_3) (\Delta_P^2 \partial_z \Phi \partial_z \Phi + \Delta_{\perp 1}^2 \partial_x \Phi \partial_x \Phi \\ &\quad + \Delta_{\perp 2}^2 \partial_y \Phi \partial_y \Phi + \Delta_P^2 \partial_z \theta \partial_z \theta + \Delta_{\perp 1}^2 \partial_x \theta \partial_x \theta), \\ f_{soc}(\theta) &= \frac{g_D}{5} (\Delta_P^2 + \Delta_{\perp 1}^2 + \Delta_{\perp 2}^2) \\ &\quad - \frac{3g_D}{5} (\Delta_P + \Delta_{\perp 1})^2 \cos 2\theta - \frac{6g_D}{5} (\Delta_P + \Delta_{\perp 1}) \Delta_{\perp 2} \sin \theta, \end{aligned} \quad (4.26)$$

where $i = 1, 2, 3$ are the summation indexes of spatial coordinates. In London limit, the term $(g_D/5)(\Delta_P^2 + \Delta_{\perp 1}^2 + \Delta_{\perp 2}^2)$ is constant over the sample, thus we drop it in the rest. Because spin degree of freedom does not couple with phase degree of freedom, $f_{grad}(\Phi, \theta)$ is simply the summation of $f_{grad}(\Phi)$ and $f_{grad}(\theta)$, where $f_{grad}(\Phi)$ and $f_{grad}(\theta)$ are the gradient energy densities of phase and spin vectors respectively. Then $f_{grad}(\Phi)$ achieves equilibrium independently and can be safely dropped. Moreover, because the HQVs are pinned by nafen strands, the system is translation invariant along the direction of nafen strands, thus all $\partial_z \theta$ terms vanish. Finally the free energy, which determines the equilibrium textures in London limit is

$$F(\theta)_{London} = \int_{\Sigma} [f_{soc}(\theta) + f_{grad}(\theta)] d\Sigma, \quad (4.27)$$

where $f_{grad}(\theta)$ and $f_{soc}(\theta)$ are given as

$$\begin{aligned} f_{grad}(\theta) &= \frac{K_1}{2} (\Delta_P^2 + \Delta_{\perp 1}^2) (\partial_x \theta \partial_x \theta + \partial_y \theta \partial_y \theta) + \frac{1}{2} (K_2 + K_3) \Delta_{\perp 1}^2 \partial_x \theta \partial_x \theta, \\ f_{soc}(\theta) &= - \frac{3g_D}{5} (\Delta_P + \Delta_{\perp 1})^2 \cos 2\theta - \frac{6g_D}{5} (\Delta_P + \Delta_{\perp 1}) \Delta_{\perp 2} \sin \theta. \end{aligned} \quad (4.28)$$

In this section, we utilize the nonlinear optimization BFGS algorithm to minimize the free energy functional Eq. (4.27) [137]. (We discuss the details of BFGS algorithm and its implements in Appendix. B.1 and Appendix. B.2.) The saddle points θ of free energy under different parameters are the equilibrium textures of spin solitons of 1D nexus objects. To facilitate minimization of free energy with nonlinear optimization algorithm, we reduce Eq. (4.27) to

$$\begin{aligned} \tilde{F}(\theta)_{London} &= \frac{1}{\zeta_D} \int_{\Sigma} \left[\frac{1}{2} (\gamma_1 + 2\gamma_2) \partial_x \theta \partial_x \theta + \frac{1}{2} \gamma_1 \partial_y \theta \partial_y \theta + \frac{1}{\zeta_D^2} \left(-\frac{1}{2} \gamma_4 \cos 2\theta - \gamma_3 \sin \theta \right) \right] d\Sigma \\ &= \frac{1}{\zeta_D} \int_{\Sigma} (\tilde{f}_{grad} + \tilde{f}_{soc}) d\Sigma \end{aligned} \quad (4.29)$$

by multiplying $(\xi_D K_1 \Delta_P^2)^{-1}$, where

$$q = \frac{\Delta_{\perp 2}}{\Delta_P}, \quad \gamma_1 = 1 + |q|^2, \quad \gamma_2 = |q|^2, \quad \gamma_3 = q(1 + |q|), \quad \gamma_4 = (1 + |q|)^2, \quad (4.30)$$

and

$$\begin{aligned} \tilde{f}_{grad} &= \frac{1}{2}(\gamma_1 + 2\gamma_2)\partial_x \theta \partial_x \theta + \frac{1}{2}\gamma_1 \partial_y \theta \partial_y \theta \\ \tilde{f}_{soc} &= \frac{1}{\xi_D^2} \left(-\frac{1}{2}\gamma_4 \cos 2\theta - \gamma_3 \sin \theta \right). \end{aligned} \quad (4.31)$$

$\xi_D K_1 \Delta_P^2$ is the characteristic unit of London limit free energy in this review.

Before talking about those numeric results and analyzing the corresponding physics, we discuss the random lattice of HQVs and 2/4 spin solitons formed by the random pinning effect of nafen strands [52, 56, 74]. We analyze the condition under which the coupling between spin solitons induced by random distributions of HQVs can be neglected. The random lattice of spin solitons is pseudo-random lattices as long as this condition is satisfied. This allows us to understand the network of 1D nexus objects consisting of 2/4 spin solitons and KLS string walls by calculating and analyzing unit cell of pseudo-random lattices consisting of spin solitons.

4.3.1 Pseudo-random lattices

In the experiment of PdB phase, the HQVs are pinned by nafen strands when they appear during cooling down. Hence the HQVs and KLS string walls randomly distribute in the PdB sample and form network. The statistic distribution of HQVs is uniform because there is no reason provides preferable location for HQV. This means the number of HQVs in unit area is constant for rotating PdB superfluid with angular velocity Ω . Then the average area occupied by one HQV is constant as well. We denote the average area occupied by HQV as $A = D(\Omega)^2$, where $D(\Omega)$ is the average distance between two HQVs. $D(\Omega)$ depends on the angular velocity as

$$D(\Omega) = \sqrt{A} = \sqrt{\frac{\kappa_0}{4\Omega}}, \quad (4.32)$$

where $\kappa_0 = h/2m$ is the circulation of HQV and m is mass of ^3He atom [35, 138].

In Fig. 4.5 (a) and (c), we illustrate the uniformly distributed HQVs under given Ω . These HQVs, as we have known at Sec. 4.2.3 and 4.2.4, are 1D nexuses which connect 2/4 spin solitons and KLS domain walls. Because the random distribution of HQVs, the 2/4 spin solitons are also randomly distributed over the PdB superfluid. Therefore the HQVs and spin solitons form a 2D random lattice [139]. These spin solitons have almost identical spin configuration and geometric size determined by gradient energy and SOC energy. Their spin dynamic response under weak magnetic drive are almost identical as well. As a result, the spin dynamic response of these spin solitons under weak drive is independent to the distribution of HQVs and spin solitons. The NMR frequency shift under weak magnetic drive is merely determined by the configuration of one spin soliton, and the total ratio intensity of system is the summation of ratio intensities of all spin solitons. We call this kind of random lattice of HQVs and spin solitons as pseudo-random lattice. This means

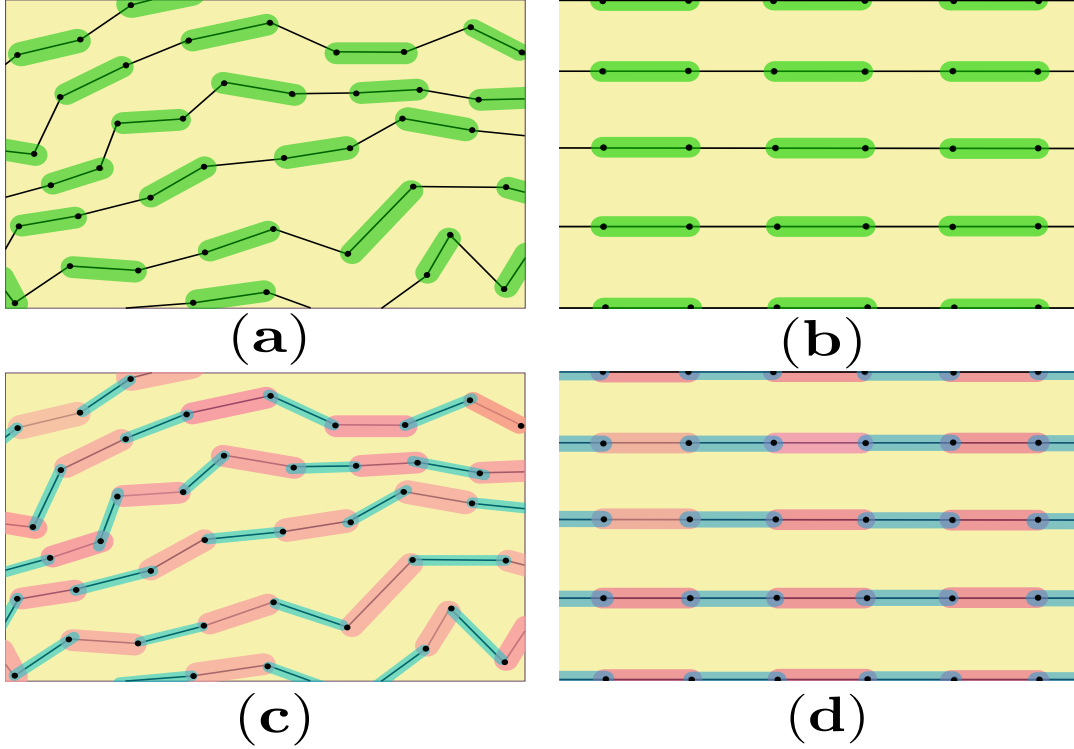


FIGURE 4.5: Illustrations of pseudo-random lattices of 1D nexus objects and their equivalent regular lattices. The black dots represent the HQVs and the black solid lines represent the KLS domain walls. Because every HQV is 1D nexus, two HQVs connect with each others via separable or inseparable $2/4$ spin solitons. These topological objects with different characteristic lengths and spatial dimensions give rise to the network of 1D nexus objects with complex hierarchy of length scales. Thus this network is an instance of the interplay between different homotopy groups of topological objects with dramatically different length scales. The small green filled rectangles represent the inseparable spin solitons, while pink and blue filled rectangles represent separable spin solitons. (a) pseudo-random lattice of inseparable spin solitons (π -solitons) when $\Omega \ll \Omega_c$. The spin solitons are almost identical and well spatially separated with each others. The spin dynamic response properties of pseudo-random lattice is equivalent to (b) 2D regular lattice of π -solitons. Similarly, (c) pseudo-random lattice of separable spin solitons (KLS-solitons and solitons) has same spin dynamic response with (d) 2D regular lattice consisting of KLS-solitons ($|\Delta\theta| = 2\theta_0$) and solitons ($|\Delta\theta| = \pi - 2\theta_0$).

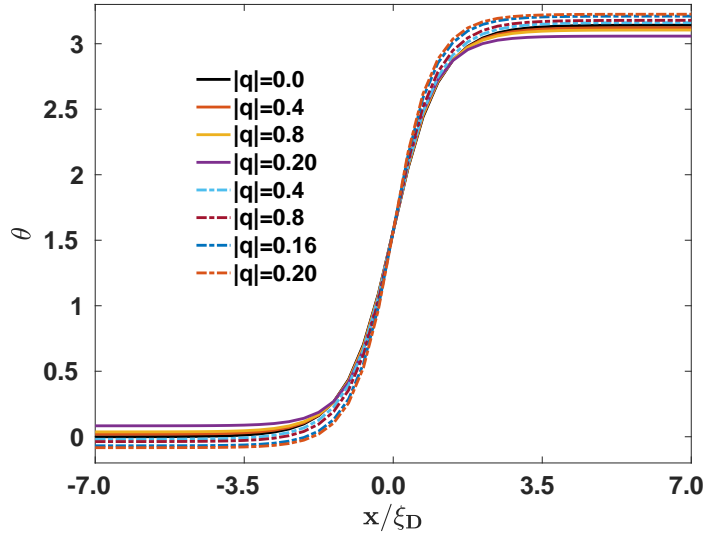


FIGURE 4.6: Equilibrium spin configurations of solitons ($|\Delta\theta| = 2\pi - \theta_0$) and big-solitons ($|\Delta\theta| = 2\pi + \theta_0$) in uniform domains. Black solid line represents spin soliton of polar phase ($|q| = 0$). The colored dash lines represent big-solitons of PdB phase with $q < 0$ from $|q| = 0.04$ until $|q| = 0.2$. The colored solid lines represent solitons of PdB phase with $q > 0$ from $q = 0.04$ until $q = 0.2$. The spin vectors of all solitons and big-solitons have same relative direction respect to orbital frame because $\theta = \pi/2$ is the stationary point of $\partial_x \theta$.

the spin dynamic response properties of pseudo-random lattice of 2/4 spin solitons are equivalent to the spin dynamic properties of regular lattice of 2/4 spin solitons. There are two types of regular lattices as shown in Fig. 4.5 (b) and (d), which correspond to inseparable and separable 2/4 spin solitons respectively.

However, the pseudo-random lattice model doesn't work any more when the angular velocity of PdB system increase up to critical value Ω_c . Recalling that the average distance $D(\Omega)$ between two HQVs is proportional to $1/\sqrt{\Omega}$ as shown in Eq. (4.32). This means spin solitons overlap and couple with each others when Ω is big. This is because the characteristic thickness of spin soliton i.e., $\sim 2\xi_D$ is constant under given external parameters. The independence of the spin solitons between two 1D nexus objects loses when $D(\omega) \sim 2\xi_D$ and the static textures of spin solitons strongly depend on the distribution of HQVs. As a result, the spin dynamic response of the random lattice of spin solitons under weak magnetic drive strongly depends on the distribution of HQVs as well. Thus the upper limit of Ω , under which pseudo-random lattice model works, is determined by $\sqrt{\kappa_0/4\Omega_c} \sim 2\xi_D$ and then

$$\Omega_c \sim \frac{\kappa_0}{16\xi_D^2}. \quad (4.33)$$

For PdB system with $\kappa_0 = 6.62 \times 10^{-8} \text{ m}^2/\text{s}$ and $\xi_D \sim 10^{-6} \text{ m}$ to $\sim 10^{-5} \text{ m}$, Eq. (4.33) suggests $\Omega_c \sim 10^1 \text{ rad/s}$ to $\sim 10^3 \text{ rad/s}$. These values is larger enough than the angular velocity of PdB system in the experiment of Ref. [74], then pseudo-random lattice model is good and we keep working with it in the rest parts of this review.

4.3.2 Spin solitons in the absence of KLS string walls – solitons and big-solitons

In order to understand the 1D nexus object consisting of $2/4$ spin soliton and KLS string wall, we start from the simpler situation in which there is absence of KLS string wall. In this case $\Delta_{\perp 2}$ is single valued over the sample of superfluid, then only solitons ($|\Delta\theta| = \pi - 2\theta_0$) with topological invariant $1/4_{(\theta_0)}$, $3/4_{(\pi-\theta_0)}$ and big-solitons ($|\Delta\theta| = \pi + 2\theta_0$) with topological invariant $1/4_{(\pi+\theta_0)}$, $3/4_{(-\theta_0)}$ are possible in the system. These two different cases correspond to spin solitons in uniform domain with $\Delta_{\perp 2} = +|q|\Delta_P$ or $\Delta_{\perp 2} = -|q|\Delta_P$ respectively. Moreover, the spin textures have translation symmetry along transverse direction of spin solitons, then the question reduces to one dimensional question. As mentioned before, we use the BFGS non-linear optimization algorithm on Eq. (4.29) to get the equilibrium configuration of spin solitons [137]. (We discuss the details of BFGS algorithm and its implements in Appendix. B.1 and Appendix. B.2.)

In Fig. 4.6, we show the equilibrium configuration of solitons and big-solitons from $|q| = 0$ to $|q| = 0.2$. The spin textures with $q > 0$ are solitons, while the spin textures with $q < 0$ are big-solitons. We find that the spin vectors of all solitons and big-solitons have common direction $\theta = \pi/2$. This is because $\theta = \pi/2$ is stationary point of $\partial_x \theta$, then $\partial_x \partial_x \theta|_{\theta=\pi/2} = 0$ for all solitons and big-solitons. We will soon see this important feature helps us to set appropriate boundary condition for searching equilibrium textures of pseudo-random lattices consisting of π -solitons.

4.3.3 Spin solitons in the presence of KLS string walls – Boundary conditions on wall

As we have discussed in Sec. 4.2.3 and Sec. 4.2.4, the HQV is 1D nexus connecting KLS domain wall and $2/4$ spin solitons. In London limit, the free energy of network of 1D nexus objects is free energy of pseudo-random lattices consisting of $2/4$ spin solitons. The equilibrium configuration of pseudo-random lattices is the saddle point of Eq. (4.29). The only complexity here is the topological invariant $2/4$ has two different representations i.e., literal $2/4$ or $1/4 + 1/4$. Based on the topological analysis, we have known these two cases correspond to inseparable π -soliton configuration and separable configurations of KLS-soliton ($|\Delta\theta| = 2\theta_0$) and soliton ($|\Delta\theta| = \pi - 2\theta_0$).

In order to quantitatively get the equilibrium spin textures for both configurations, we minimize the London limit free energy Eq. (4.29) in the presence of KLS string wall. For parametrization Eq. (4.9), KLS string wall separates two domains with opposite $\Delta_{\perp 2}$ in an unit cell of pseudo-random lattice of spin solitons.

However, different from the situation with uniform domain for soliton and big-soliton in Sec. 4.3.2, the existence of KLS domain wall induces a singularity of the London limit free energy $\tilde{F}(\theta)$. That is because the order parameter $A_{\alpha i}^{PdB}$ in the London limit is ill-defined on the KLS domain wall. As a result, the free energy Eq. (4.29) and corresponding Lagrangian equation of θ are also ill-defined on the KLS domain wall. On the other hand, we know θ is a continuous function everywhere for $2/4$ spin soliton because the relative 1-loop of $\pi_1(S_S^1, \tilde{R}_2)$ is continuous mapping. Then θ keeps single-valued and continuous. These facts require us to set a proper boundary condition of θ on the KLS domain wall. The London limit free energy Eq. (4.29) can

be minimized with this boundary condition.

Because the free energy and Lagrangian equation of θ is ill-defined on the KLS domain wall in London limit, θ of different domains in the vicinity of the KLS domain wall does not relate to each other by Lagrangian equation. Then θ in two different domains, which are separated by KLS domain wall, are determined independently in two uniform domains with opposite $\Delta_{\perp 2}$. In this situation, to keep the continuity of θ on the KLS domain wall, the boundary condition of θ must be a common value of spin solitons in both two domains with opposite $\Delta_{\perp 2}$. For the inseparable spin soliton with literally topological invariant $2/4$, the natural choice is the stationary point of big-soliton and soliton i.e., $\theta_{KLS} = \pi/2$. This boundary condition indicates the π -soliton may be understood as a hybrid of big-soliton and soliton in London limit. As for the separable spin soliton with topological invariant $1/4 + 1/4$, because all KLS-solitons have common values $\theta = 0$ or $\theta = \pi$ on the KLS domain wall, there are two options of boundary condition [133]. However, these two options are identical, they give rise to same spin textures of pseudo-random lattices consisting of separable spin solitons, see details in Appendix. D.1. Thus in the rest of this review, we exclusively use $\theta_{KLS} = 0$ for all calculations about separable spin solitons in main text.

4.3.4 Equilibrium spin textures and free energies of pseudo-random lattices consisting of inseparable and separable $2/4$ spin solitons

In Fig. 4.7, we show the equilibrium textures of pseudo-random lattices consisting of inseparable and separable $2/4$ spin solitons with $|q| = 0.18$ and $D = 18\zeta_D$. These two equilibrium configurations of a pair of 1D nexus objects are two kinds of unit cells of pseudo-random lattices. Both of them are axially symmetric about $x = 0$ as suggested in Sec. 4.3.1. This property allows me to increase the precision of calculation by just calculating one-half of unit cell. As an example, the equilibrium structures of spin solitons, which were gotten from BFGS optimization in one-half unit cell, are shown in Fig. 4.8. To collect enough data which could be used to calculate spin dynamic response and compare with experiment, I calculated spin textures with parameters $|q|$ from 0 to 0.2 and D from $4\zeta_D$ to $18\zeta_D$. Based on these data, we further calculated the reduced London limit free energy Eq. (4.29) of these two types of pseudo-random lattices, the results are shown in Fig. 4.9. Before we discussing these numeric results, we first evaluate the Eq. (4.29) for one-half of unit cell when $D \geq 10\zeta_D$. In this case,

$$\begin{aligned} \int_{\Sigma} \tilde{f}_{grad} d\Sigma &\sim \frac{1}{2}(1 + |q|^2) \frac{\pi^2}{4\zeta_D^2} \int_{\Sigma'} d\Sigma, \\ \int_{\Sigma} \tilde{f}_{soc} d\Sigma &\sim \int_{\Sigma'} \tilde{f}_{soc} d\Sigma + \int_{\Sigma - \Sigma'} \tilde{f}_{soc} d\Sigma, \end{aligned} \quad (4.34)$$

where Σ' is the region which spin solitons occupy. Its area in x - y plane is around $D\zeta_D$. Then the integral of \tilde{f}_{soc} in Eq. (4.34) can be evaluated as

$$\begin{aligned} \int_{\Sigma'} \tilde{f}_{soc} d\Sigma &\sim 0, \\ \int_{\Sigma - \Sigma'} \tilde{f}_{soc} d\Sigma &\sim \int_{\Sigma - \Sigma'} \tilde{f}_{soc}|_{y>0} d\Sigma + \int_{\Sigma - \Sigma'} \tilde{f}_{soc}|_{y<0} d\Sigma. \end{aligned} \quad (4.35)$$

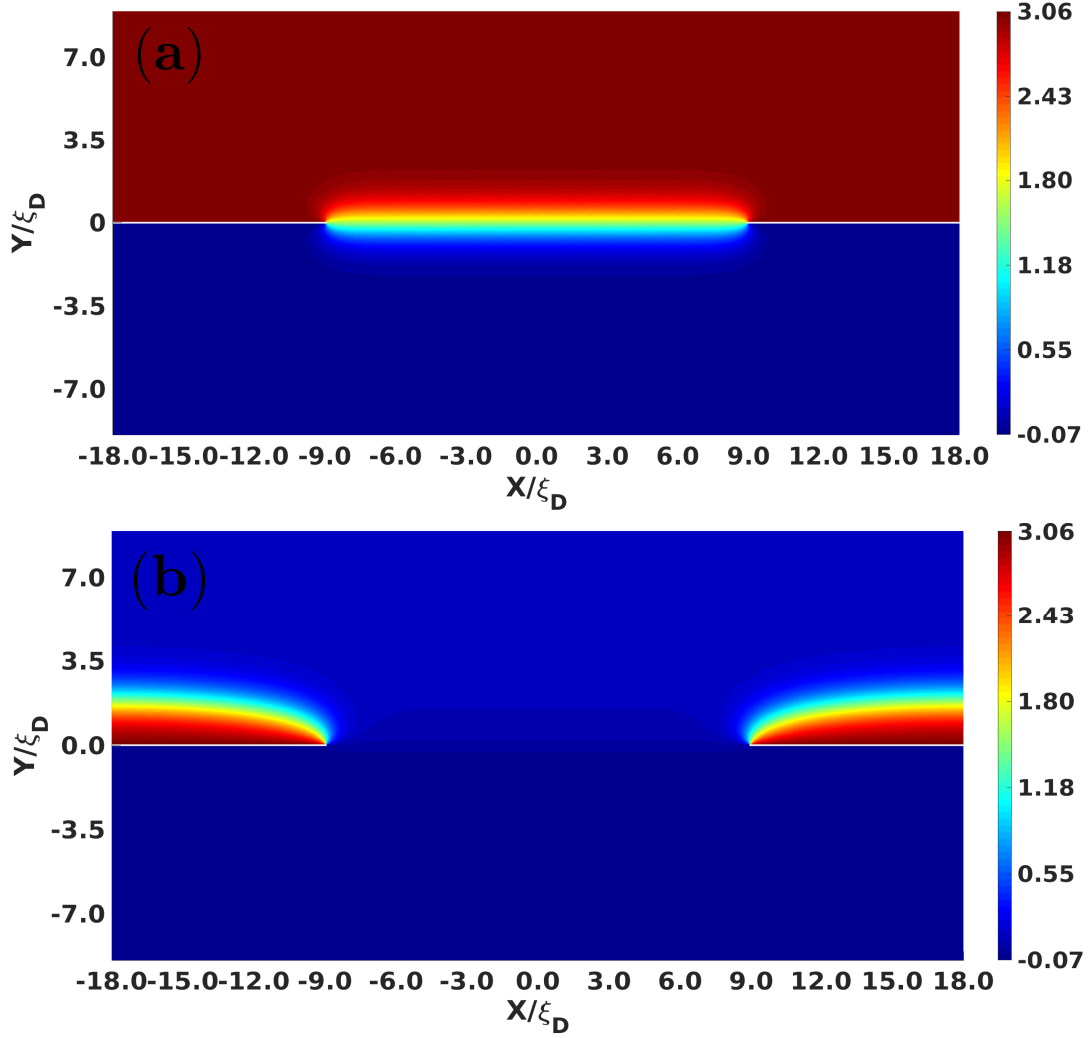


FIGURE 4.7: Two kinds of equilibrium configurations of unit cell of pseudo-random lattices [133]. These equilibrium spin textures are gotten by minimizing the reduced London limit free energy $\tilde{F}(\theta)_{\text{London}}$ in Eq. (4.29) by BFGS algorithm. The resulted equilibrium distributions of θ depict the equilibrium textures of spin vectors in a unit cell of pseudo-random lattices. (a) depicts the unit cell of pseudo-random lattice consisting of inseparable $2/4$ spin solitons (π -solitons) for $|q| = 0.18$ and $D = 18\xi_D$. (b) depicts the unit cell of pseudo-random lattice consisting of separable spin solitons (KLS-Solitons and solitons) with same parameters of (a) but its topological invariant is $1/4 + 1/4$.

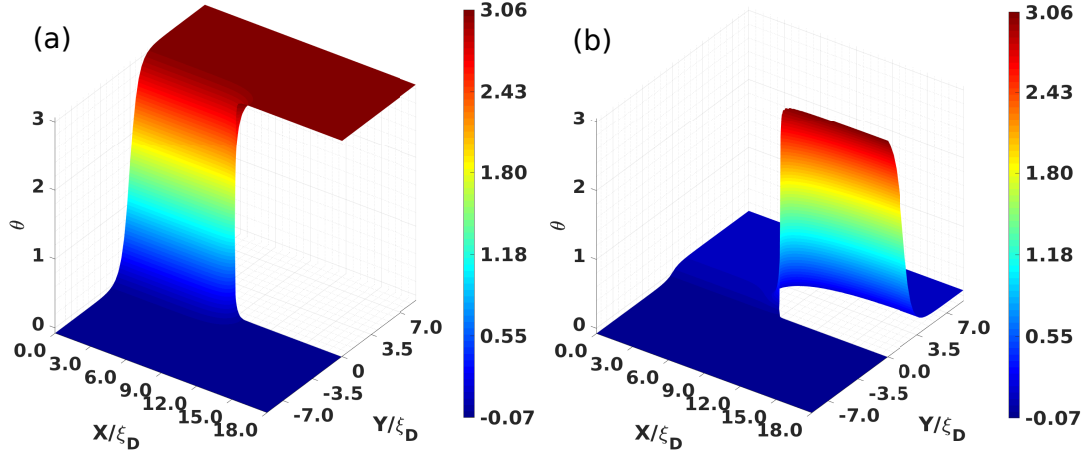


FIGURE 4.8: The equilibrium configurations of inseparable and separable spin solutions in one-half unit cell with $|q| = 0.18$ and $D = 18\zeta_D$. (a) Inseparable (π -soliton) configuration; (b) Separable (KLS-soliton and soliton) configuration.

The first integral in Eq. (4.35) vanishes because \tilde{f}_{soc} is not negative-definite function in Σ' . In contrary, \tilde{f}_{soc} has negative-definite equilibrium values in regions $(\Sigma - \Sigma')_{y>0}$ and $(\Sigma - \Sigma')_{y<0}$. Hence

$$\int_{\Sigma - \Sigma'} \tilde{f}_{soc} d\Sigma \sim \frac{\zeta_D D (D - \zeta_D)}{2} [\tilde{f}_{soc}|_{y>0} + \tilde{f}_{soc}|_{y<0}] q. \quad (4.36)$$

As a result, the reduced London limit free energy is evaluated as

$$\begin{aligned} \tilde{F}(\theta)_{London} &\sim \frac{1}{8}(1 + |q|^2) \frac{\pi^2 D}{\zeta_D} + \frac{D(D - \zeta_D)}{2} [\tilde{f}_{soc}|_{y>0} + \tilde{f}_{soc}|_{y<0}] q \\ &\sim \frac{1}{8}(1 + |q|^2) \frac{\pi^2 D}{\zeta_D} + \frac{D(D - \zeta_D)}{2\zeta_D^2} \\ &\quad \times [-(1 + |q|)^2 \cos 2|\theta_0| - 2(1 + |q|)|q| \sin |\theta_0|]. \end{aligned} \quad (4.37)$$

Eq. (4.37) immediately suggests SOC energy is dominating energy of London limit free energy when the average distance D is big and the $\tilde{F}(\theta)_{London} < 0$ because $(\tilde{f}_{soc}|_{y>0} + \tilde{f}_{soc}|_{y<0}) < 0$ over $\Sigma - \Sigma'$. For $|q| \in [0, 0.2]$, $\tilde{F}(\theta)_{London}$ in Eq. (4.37) is around -130 to -200 with $D = 18\zeta_D$. This is exactly what the numeric results show in Fig. 4.9(b). When D decreases during the angular velocity Ω of PdB system increases, Eq. (4.37) increases monotonically as shown in Fig. 4.9 (a) and (b). Other information which Eq. (4.37) indicates is the London limit free energy of unit cell of pseudo-random lattice is decreasing function for $|q|$ as long as SOC energy is dominating energy. This is because $\tilde{f}_{soc}|_{y>0} + \tilde{f}_{soc}|_{y<0}$ is decreasing function of $|q|$. However, this is not true any more when D is small. Because SOC energy is not dominating energy in this case, the positive-definite gradient energy is competitive with SOC energy. As a result, we can find from Fig. 4.9 (a) and (b) that the $\tilde{F}(\theta)_{London}$ of one-half unit cell does not change remarkably for different $|q|$ in small unit cell with $D \sim [4\zeta_D, 8\zeta_D]$. The free energy density of per unit area of equilibrium pseudo-random lattices can be evaluated by multiplying the surface density of 1D nexues

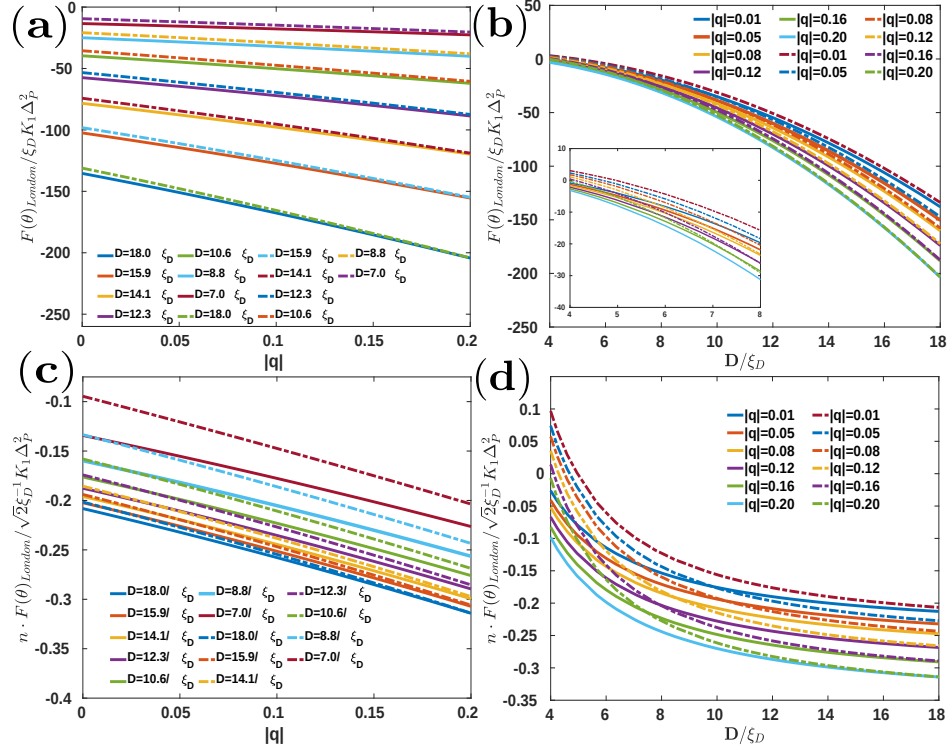


FIGURE 4.9: Free energies $F(\theta)_{London}$ of one-half unit cell and surface densities of free energies $n \cdot F(\theta)_{London}$ of pseudo-random lattices consisting of $2/4$ spin solitons. The external parameters $|q|$ are from 0.01 to 0.20 and D are from $4\xi_D$ to $18\xi_D$. The reduced free energies $\tilde{F}(\theta)_{London}$ and reduced densities of free energies $n \cdot \tilde{F}(\theta)_{London}$ are calculated based on the equilibrium spin textures of one-half unit cell of the lattices with the pseudo-random lattice model. These results depict the equilibrium free energies and energy densities of spin degree of freedom of 1D nexus objects network in PdB system. The solid lines represent the inseparable spin solitons, and the dash-dot lines represent the separable spin solitons. (a) shows the free energies $F(\theta)_{London}$ as functions of $|q|$ with different average distances D . When SOC energy dominates the system in big unit cell, $F(\theta)_{London}$ is monotonically decreasing respect to $|q|$. While $F(\theta)_{London}$ does not show remarkably change as $|q|$ changes when gradient energy is competitive to SOC energy in a small unit cell. (b) shows the free energies $F(\theta)_{London}$ are monotonically decreasing functions of D . The zooming plot between $4\xi_D$ and $8\xi_D$ in (b) demonstrates this monotonicity is held even when the gradient energy is competitive with the SOC energy. Similarly, (c) depicts the London limit free energy density $n \cdot \tilde{F}(\theta)_{London}$ is monotonically decreasing function of $|q|$. However, (d) demonstrates the London limit free energy densities $n \cdot \tilde{F}(\theta)_{London}$ asymptotically trend to constants determined by SOC energy when SOC energy is the dominating energy in big unit cell. When D is small enough ($D < 6\xi_D$) and gradient energy becomes the dominating energy, the free energy densities increase rapidly as D decrease because $n \cdot \tilde{F}(\theta)_{London}|_{D < 6\xi_D} \propto 1/D$. All these results show the equilibrium free energies of pseudo-random lattice consisting of inseparable spin solitons (π -solitons) are lower than those of separable spin solitons (KLS solitons and solitons).

$n = D^{-2}$ to the Eq. (4.37),

$$\begin{aligned} n \cdot \tilde{F}(\theta)_{\text{London}} &\sim \frac{1}{8}(1 + |q|^2) \frac{\pi^2}{\xi_D D} \\ &+ \frac{1}{2\xi_D^2} [-(1 + |q|)^2 \cos 2|\theta_0| - 2(1 + |q|)|q| \sin |\theta_0|]. \end{aligned} \quad (4.38)$$

Then we find the London limit free energy density of pseudo-random lattices trends to be a constant determined by q when SOC energy is dominating with large D . We can clearly see this from Fig. 4.9(d) when D is larger than $10\xi_D$. From Eq. (4.38), we find the magnitude of $n \cdot F(\theta)_{\text{London}}$ is around $10^{-1} \sqrt{2} \xi_D^{-1} K_1 \Delta_p^2$ for $|q| \in [0, 0.2]$ when $D > 10\xi_D$. This coincides with the numerical results in Fig. 4.9 (c) and (d). When the system is dominated by gradient energy if D is small enough, the free energy density increases rapidly as shown in Fig. 4.9 (d). If the angular velocity increases successively, the system will go into a parameters region in which pseudo-random lattice model violates.

In all cases, we find the equilibrium free energies of one-half unit cell of separable spin solitons (KLS solitons and solitons) are slightly higher than those of inseparable spin solitons (π -solitons). As a result, the equilibrium free energy densities of pseudo-random lattices consisting of separable spin solitons (KLS-solitons and solitons) are also slightly higher than those of inseparable spin solitons (π -solitons). This significant fact suggests that the equilibrium states which was observed in experiment of rotating PdB system is the pseudo-random lattice of inseparable $2/4$ spin solitons (π -solitons) of 1D nexus objects. We will see this is true in next chapter by calculating the spin dynamic response under weak magnetic drive.

4.4 The mirror symmetry of 1D nexus objects and its breaking

As we mentioned in Sec. 4.1, The London limit free energy $F(\theta)_{\text{London}}$ has a mirror symmetry when the coordinates are permuted to each other i.e., $F[\theta(x', y')] = F[\theta(x, y)]$ with $x' = y$ and $y' = x$. This mirror symmetry does not vanish even in the presence of 1D nexus object. As a result, the spin textures of $2/4$ spin solitons have this mirror symmetry as well.

This discrete symmetry originates from the reduction of degenerate space of order parameter by requirement of continuity of order parameter in the presence of KLS domain wall. In order to understand this, we start from the degenerate manifold of PdB which generates from symmetry breaking transition of polar phase vacuum. In this case, $R_{\text{PdB}} \cong SO(2)_{S-L} \times \mathbb{Z}_2^{S-\Phi}$, in which the nontrivial element of $\mathbb{Z}_2^{S-\Phi}$ corresponds to the presence of KLS domain wall [97]. The requirement of continuity of order parameter reduces the degenerate space of $\hat{\mathbf{e}}^1$ and $\hat{\mathbf{e}}^2$ on both sides of domain wall from $SO(2)_{S-L}$ to (i) $\hat{\mathbf{e}}^1 \rightarrow -\hat{\mathbf{e}}^1$, while $\hat{\mathbf{e}}^2$ keeps its direction and (ii) $\hat{\mathbf{e}}^2 \rightarrow -\hat{\mathbf{e}}^2$, while $\hat{\mathbf{e}}^1$ keeps its direction. The parametrization in Eq. (4.9), which we used in previous calculations and discussions, corresponds to the vacuum state (i) and the direction of static magnetic field $\mathbf{H}^{(0)}$ is set to parallel with the $\hat{\mathbf{e}}^2$. Because the vacuum state (ii) is another possible vacuum state with same free energy of case (i) in the presence of KLS domain wall, the London limit free energy $F(\theta)_{\text{London}}$ is invariant when we transform from vacuum state (i) to vacuum state (ii). In our case,

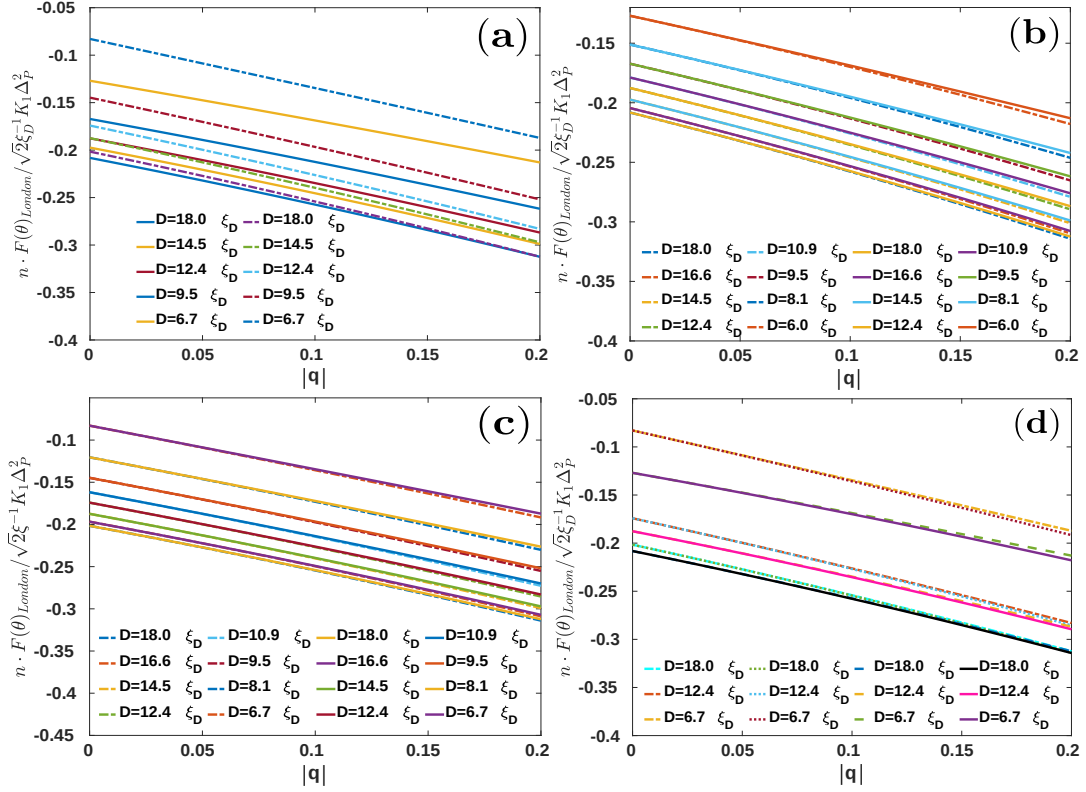


FIGURE 4.10: Surface densities of equilibrium London limit free energies of pseudo-random lattices with vacuum state (i) and vacuum state (ii) respective. These two vacuum states are not degenerated with same free energy any more when the direction of KLS domain wall is fixed. (a) The surface densities of London limit free energies of pseudo-random lattices consisting of inseparable spin solitons (π -solitons) and separable spin solitons (KLS-solitons and solitons) in the vacuum state (ii). This figure shows similar features with Fig. 4.9(c). (b) depicts the surface densities of London limit free energies of pseudo-random lattices consisting of inseparable 2/4 spin solitons of vacuum states (i) and (ii) respectively. The dash-dot lines represent the vacuum state (i) while the solid lines represent the vacuum state (ii). (c) depicts the surface densities of London limit free energies of pseudo-random lattices consisting of separable 2/4 spin solitons of vacuum states (i) and (ii) respectively. The dash-dot lines represent the vacuum state (i) while the solid lines represent the vacuum state (ii). (d) depicts the surface densities of London limit free energies of pseudo-random lattices in vacuum states (i) and (ii). The solid lines and dash lines represent the pseudo-random lattices consisting of inseparable spin solitons (π -solitons) within vacuum states (i) and (ii) respectively. The dot lines and dash-dot lines represent the pseudo-random lattices consisting of separable spin solitons (KLS-solitons and solitons) within vacuum states (i) and (ii) respectively. We found the pseudo-random lattices consisting of 2/4 inseparable spin solitons within vacuum state (i) have lowest equilibrium free energies.

the parametrization of vacuum state (ii) is

$$\hat{\mathbf{d}} = \hat{y}\cos\theta - \hat{z}\sin\theta, \hat{\mathbf{e}}^2 = -\hat{y}\sin\theta - \hat{z}\cos\theta, \hat{\mathbf{e}}^1 = \hat{x}, \mathbf{H}^{(0)} = H\hat{x}, \quad (4.39)$$

and the corresponding dimensionless London limit free energy is

$$\begin{aligned} \tilde{F}(\theta)_{London} = & \frac{1}{\xi_D} \int_{\Sigma} \left[\frac{1}{2}(\gamma_1 + 2\gamma_2)\partial_y\theta\partial_y\theta + \frac{1}{2}\gamma_1\partial_x\theta\partial_x\theta \right. \\ & \left. + \frac{1}{\xi_D^2} \left(-\frac{1}{2}\gamma_4\cos 2\theta - \gamma_3\sin\theta \right) \right] d\Sigma \end{aligned} \quad (4.40)$$

where

$$q = \frac{\Delta_{\perp 1}}{\Delta_P}, \quad \gamma_1 = 1 + |q|^2, \quad \gamma_2 = |q|^2, \quad \gamma_3 = q(1 + |q|), \quad \gamma_4 = (1 + |q|)^2. \quad (4.41)$$

Comparing Eq. (4.40) and Eq. (4.29), we can see the mirror symmetry.

However, this discrete symmetry may be destroyed if the direction of domain wall is fixed in both vacuum states (i) and (ii). In this case, the term containing γ_3 in Eq. (4.40) is invariant for both parametrizations, and thus violates this mirror symmetry. As a result, the equilibrium states of Eq. (4.40) and Eq. (4.29) are not identical any more. Then we need to check the equilibrium London limit free energy of these two different equilibrium states. We did the same numeric minimizations of London limit free energy with parametrization Eq. (4.39) and calculated the surface densities of equilibrium free energies of pseudo-random lattices in vacuum state (ii). The latter can be evaluated as

$$\begin{aligned} n \cdot \tilde{F}(\theta)_{London}|_{(ii)} & \sim \frac{1}{8}(1 + |q|^2) \frac{\pi^2}{\xi_D D} + \frac{\pi^2}{4\xi_D D} |q|^2 + \frac{1}{2} [\tilde{f}_{soc}|_{y>0} + \tilde{f}_{soc}|_{y<0}]_q \\ & \sim n \cdot \tilde{F}(\theta)_{London}|_{(i)} + \frac{\pi^2}{4\xi_D D} |q|^2. \end{aligned} \quad (4.42)$$

Then we can expect the surface densities of equilibrium London limit free energy of vacuum state (ii) are slightly higher than those of vacuum state (i) when $|q| \leq 0.2$. In Fig. 4.10, we show this for pseudo-random lattices consisting of inseparable and separable 2/4 spin solitons respectively. In all cases, the surface densities of London limit free energy of vacuum state (ii) are indeed higher than those of vacuum state (i).

Chapter 5

Spin Dynamical Response and NMR

In this chapter, we discuss how the network of mesoscopic extended structure of KLS string wall — pseudo random lattice of $[1/2]$ spin solitons response the weak magnetic drive in the NMR experiment in Ref. [74]. We firstly demonstrate the spin dynamic equation and discuss how the static spin textures modify the NMR spectrum by generating a satellite peak related to the NMR main peak. Then we use the data of static spin textures, which we got in Chapter. 4, to solve spin response equation and get the NMR frequency shift of satellite peak. The experimentally observed scaling rule of the NMR ratio intensity against the rotation angular velocity Ω also be checked.

We have talked the topological origin of network of 1D nexus objects with topological invariant $2/4$ as well as their equilibrium free energies in previous chapters. Because there are two kinds of spin solitons connecting with KLS string wall, the pseudo-random lattices consisting of them have different equilibrium free energy densities. To compare with the experiments and check the theories, we must calculate the spin dynamic response. Under weak enough magnetic drive, the nuclear spin magnetization of PdB superfluid responds a NMR signal when the frequency of magnetic drive matches the transverse spin dynamic mode. Because the spin dynamics of symmetry breaking states of ^3He is strongly influenced by SOC energy which is determined by the relative orientations between spin and orbital degenerate parameters, the NMR of continuous wave drive is a perfect tool, which can be used to detect the pseudo-random lattice of 1D nexus objects network via dynamics of spin solitons [94].

When the PdB superfluid is equilibrium, the spin density has equilibrium value $\mathbf{S}^{(0)}$ over the system. If the weak homogeneous magnetic drive is turned on, the spin density gets a tiny variation $\delta\mathbf{S}(\mathbf{r}, t)$, where \mathbf{r} and t are spatial and time coordinates respectively. In this perturbed system, the transverse spin density δS_+ may be expanded as

$$\delta S_+(\mathbf{r}, t) = \int d\sigma' \int dt' \frac{\delta S_+}{\delta H_a}(\mathbf{r}, t, \mathbf{r}', t') \delta H_a(\mathbf{r}', t') + O(\delta H_a^2), \quad (5.1)$$

where $\delta H_a \equiv \delta\mathbf{H}$ is the homogeneous weak magnetic drive and $a = 1, 2, 3$ are spatial coordinate indexes. Thus the PdB superfluid under magnetic drive is a linear response system if $|\delta\mathbf{H}| \ll |\mathbf{H}^{(0)}|$ [140]. The poles of the transverse spin dynamic response function $\delta S_+ / \delta H_a$ correspond to eigen-modes of the NMR. The most classic example of this response is the detection of Larmor frequency in homogeneous

system, and we will see soon that spin textures also put their fingerprints in the response mode. We calculate these eigen-modes for two kinds of pseudo-random lattices of 1D nexus objects with topological invariant 2/4 in this chapter.

5.1 Spin dynamic response equations

Spin-orbit coupling plays an important role in the NMR measurements of significant properties of different superfluid phases in ^3He system. This is because the coherence of superfluid states, which breaks relative symmetry between spin and orbital degree of freedom, strengthens the SOC energy [141, 142]. This gives rise to the observable NMR frequency shift of nuclear spin magnetization. In our case, the SOC energy takes into account all the information and effects of spin vectors in spin solitons, which connect to the KLS domain wall via 1D nexus. Thus, we must calculate the spin dynamic response function $\delta S_+/\delta H_a$ dominated by SOC energy.

In this section, we utilize the spin dynamic equations dominated by SOC energy to get $\delta S_+/\delta H_a$ and corresponding eigenequations of poles [143]. Because the SOC energy is much smaller than the microscopic energy scales of PdB superfluid i.e., Δ_P , the characteristic time scales of spin dynamic response function $\delta S_+/\delta H_a$ is much longer than the time scales of microscopic processes which are proportional to Δ_P^{-1} . All the microscopic processes with time scales Δ_P^{-1} are equilibrium in the spin dynamic processes under weak magnetic drive. This means the spin dynamic equations are a system of hydrodynamic equations of spin densities δS_a and spin vectors of order parameter [94, 143].

In the limit of hydrodynamics, the system of dynamic equations of spin densities S_α and spin vectors are system of Liouville equations

$$\frac{\partial S_\alpha}{\partial t} = \{F_{hydrodynamics}, S_\alpha\}, \quad \frac{\partial V_\alpha^a}{\partial t} = \{F_{hydrodynamics}, V_\alpha^a\}, \quad V_\alpha^a = \hat{e}_\alpha^1, \hat{e}_\alpha^2, \hat{d}_\alpha, \quad (5.2)$$

where $\alpha = 1, 2, 3$ are the indexes of spatial coordinates. And V_α^a denote the three spin vectors of order parameter i.e., $V_\alpha^1 = \hat{e}_\alpha^1$, $V_\alpha^2 = \hat{e}_\alpha^2$, $V_\alpha^3 = \hat{d}_\alpha$. The hydrodynamic free energy of PdB superfluid dominated by SOC energy is

$$F_{hydrodynamics} = \int_\Sigma (f_H + f_{soc} + f_{grad}) d\Sigma. \quad (5.3)$$

Thus Eq. (5.2) can be further written as

$$\begin{aligned} \frac{\partial S_\alpha}{\partial t} = & \int_\Sigma d^3r' \frac{\delta F_{hydrodynamics}}{\delta S_\beta} (r') \{S_\beta(r'), S_\alpha(r)\} \\ & + \int_\Sigma d^3r' \frac{\delta F_{hydrodynamics}}{\delta V_\beta^a} (r') \{V_\beta^a(r'), S_\alpha(r)\}, \end{aligned} \quad (5.4)$$

and

$$\frac{\partial V_\alpha^a}{\partial t} = \int_\Sigma d^3r' \frac{\delta F_{hydrodynamics}}{\delta S_\beta} (r') \{S_\beta(r'), V_\alpha^a(r)\}, \quad (5.5)$$

where $\beta = 1, 2, 3$ are indexes of spatial components of hydrodynamic variables. The

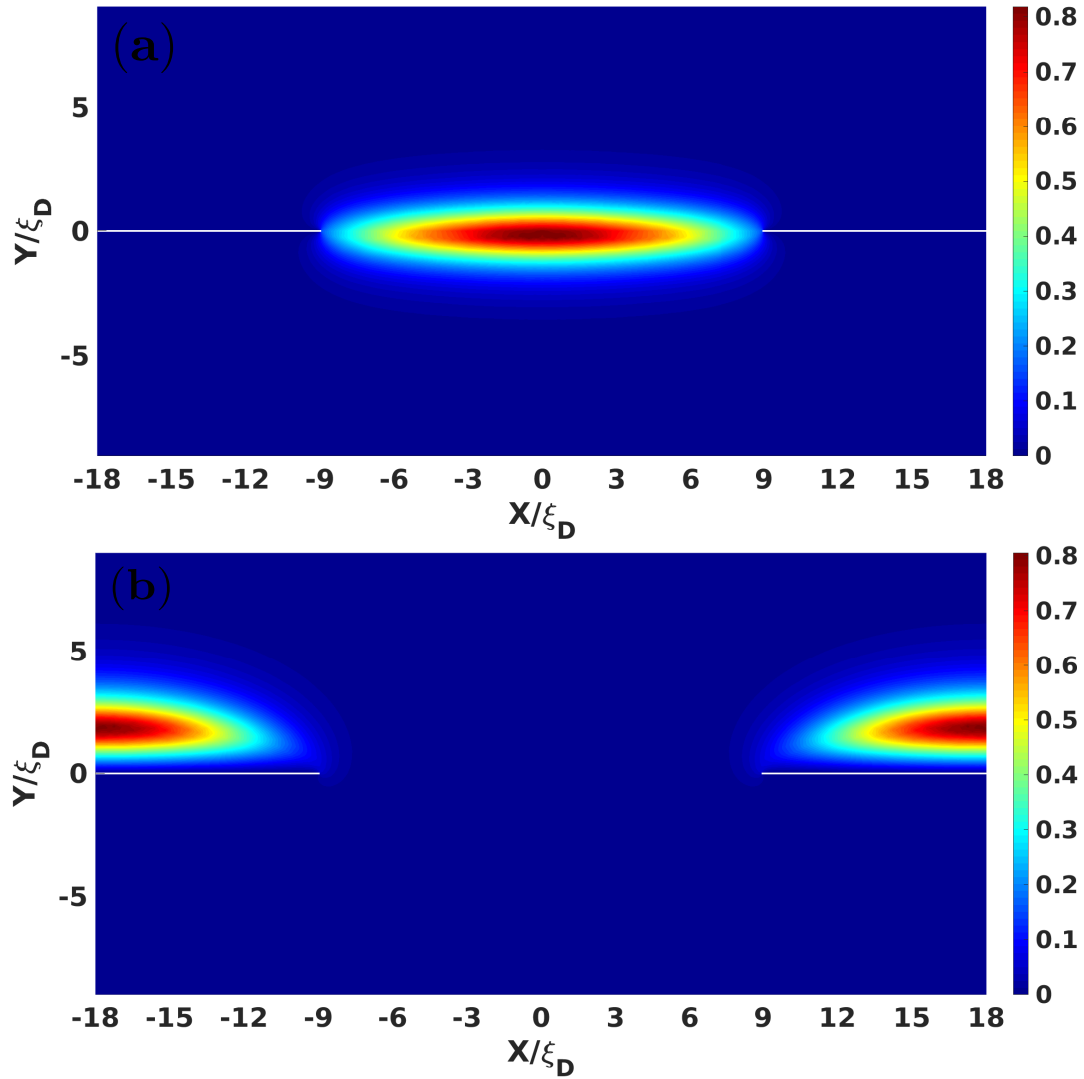


FIGURE 5.1: The modulus $|\delta S_+(\omega)|$ of the lowest transverse spin dynamic response modes located in the unit cells of pseudo-random lattices of inseparable and separable 2/4 spin solitons. In both cases, we depict the results with parameters $|q| = 0.18$ and $D = 18\xi_D$. (a) $|\delta S_+(\omega)|$ in unit cell of inseparable spin solitons (π -solitons); (b) $|\delta S_+(\omega)|$ in unit cell of separable spin solitons (KLS-solitons and Solitons).

Poisson brackets between S_α and V_α^a can be gotten by the commutators-based methods in Ref. [144] as

$$\{S_\alpha(r_1), S_\beta(r_2)\} = \epsilon_{\alpha\beta\gamma} S_\gamma \delta(r_1 - r_2), \quad \{S_\alpha(r_1), V_\beta^a(r_2)\} = \epsilon_{\alpha\beta\gamma} V_\gamma^a \delta(r_1 - r_2), \quad (5.6)$$

where r_1 and r_2 are the spatial coordinates and $\epsilon_{\alpha\beta\gamma}$ is the Levi-Civita symbol. After plugging Eq. (5.6) into Eq. (5.4) and Eq. (5.5), the coupled first order dynamic equations of spin densities S_α and V_α^a are given as

$$\frac{\partial S_\alpha}{\partial t} = \gamma H_\beta \epsilon_{\alpha\beta\gamma} S_\gamma - \frac{6}{5} g_D V_j^d V_\gamma^b \epsilon_{\alpha\beta\gamma} Q_{\beta j}^{bd} + (\partial_i \partial_j V_\beta^b) V_\gamma^a \epsilon_{\alpha\beta\gamma} K_{ij}^{ba}, \quad (5.7)$$

$$\frac{\partial V_\alpha^a}{\partial t} = \gamma H_\beta \epsilon_{\alpha\beta\gamma} V_\gamma^a - \delta \gamma^2 \chi_\perp^{-1} S_\eta V_\eta^3 V_\beta^3 \epsilon_{\alpha\beta\gamma} V_\gamma^a - \gamma^2 \chi_\perp^{-1} S_\beta \epsilon_{\alpha\beta\gamma} V_\gamma^a, \quad (5.8)$$

where $\delta = (\chi_\perp - \chi_\parallel) / \chi_\parallel$ in which χ_\perp and χ_\parallel are the transverse magnetic susceptibility and the longitude magnetic susceptibility of PdB phase respectively.

$$K_{ij}^{ba} = K_1 \delta_{ij} X_m^b X_m^a + K_2 X_j^a X_i^b + K_3 X_j^b X_i^a, \quad Q_{\beta j}^{bd} = X_\beta^b X_j^d + X_\beta^d X_j^b \quad (5.9)$$

with

$$X_i^1 = \Delta_{\perp 1} \hat{x}_i, \quad X_i^2 = \Delta_{\perp 2} \hat{y}_i, \quad X_i^3 = \Delta_\parallel \hat{z}_i. \quad (5.10)$$

The details of calculation from Eq. (5.4) to Eq. (5.8) are shown in Appendix. C.1.

Starting from the first order equations of spin densities and degenerate parameters in Eq. (5.7) and Eq. (5.8), we can further derive the second order spin dynamic response equations of δS_α under weak magnetic drive δH_α . This was done by plugging

$$S_\alpha = S_\alpha^{(0)} + \delta S_\alpha(\mathbf{r}, t), \quad V_\alpha^a = V_\alpha^{a(0)} + \delta V_\alpha^a(\mathbf{r}, t) \quad (5.11)$$

and

$$H_\alpha = H_\alpha^{(0)} + \delta H_\alpha(t) \quad (5.12)$$

into Eq. (5.7) and Eq. (5.8). Here the $S_\alpha^{(0)}$ and $V_\alpha^{a(0)}$ are the equilibrium spin densities and equilibrium degenerate parameters respectively. While the $\delta S_\alpha(\mathbf{r}, t)$ and $\delta V_\alpha^a(\mathbf{r}, t)$ are the dynamic parts of the perturbed spin densities and degenerate parameters. The $H_\alpha^{(0)}$ is the static magnetic field and $\delta H_\alpha(t) = |\delta \mathbf{H}| \hat{x} e^{-i\omega t}$ is the homogeneous RF continuous-wave drive. We put the details of calculations in Appendix. C.2 and the derived spin dynamic response equations within frequency form is

$$i\omega \delta S_\alpha(\omega) = \gamma \epsilon_{\alpha\beta\gamma} H_\beta^{(0)} \delta S_\gamma(\omega) + \gamma \epsilon_{\alpha\beta\gamma} S_\gamma^{(0)} \delta H_\beta(\omega) + \frac{\Xi_{\alpha\lambda}}{i\omega} \delta S_\lambda(\omega) + \frac{C_{\alpha\eta}}{i\omega} \delta H_\eta(\omega) \quad (5.13)$$

and

$$\begin{aligned} \Xi_{\alpha\lambda} &= \frac{\gamma^2}{\chi_\perp} K_{ij}^{ba} \Lambda_{ij\alpha\lambda}^{ba} + \frac{6g_D\gamma^2}{5\chi_\perp} R_{j\lambda\alpha\beta}^{db} Q_{\beta j}^{bd} + \frac{6g_D\gamma^2}{5\chi_\perp} V_\zeta^{d(0)} V_\gamma^{b(0)} \epsilon_{j\lambda\zeta} \epsilon_{\alpha\beta\gamma} Q_{\beta j}^{bd}, \\ C_{\alpha\eta} &= \gamma G_{ij\alpha\eta}^{ba} K_{ij}^{ba} - \frac{6g_D\gamma}{5} R_{j\eta\alpha\beta}^{db} Q_{\beta j}^{bd} - \frac{6g_D\gamma}{5} V_\zeta^{d(0)} V_\gamma^{b(0)} \epsilon_{j\eta\zeta} \epsilon_{\alpha\beta\gamma} Q_{\beta j}^{bd}, \end{aligned} \quad (5.14)$$

where

$$\begin{aligned}
R_{j\eta\alpha\beta}^{db} &= V_j^{d(0)} V_\beta^{b(0)} \delta_{\eta\alpha} - V_j^{d(0)} V_\alpha^{b(0)} \delta_{\eta\beta}, \quad G_{ij\alpha\gamma}^{ba} = (\partial_i \partial_j V_\alpha^{b(0)}) V_\gamma^{a(0)} - (\partial_i \partial_j V_\beta^{b(0)}) \delta_{\beta\gamma} V_\alpha^{a(0)}, \\
\Lambda_{ij\alpha\lambda}^{ba} &= (\partial_i \partial_j V_\beta^{b(0)}) \delta_{\beta\lambda} V_\alpha^{a(0)} + (V_\gamma^{b(0)} V_\gamma^{a(0)} \delta_{\alpha\lambda} - \delta_{\gamma\lambda} V_\alpha^{b(0)} V_\gamma^{a(0)}) \partial_i \partial_j \\
&\quad + [(\partial_i V_\gamma^{b(0)}) V_\gamma^{a(0)} \delta_{\alpha\lambda} - (\partial_i V_\alpha^{b(0)}) V_\gamma^{a(0)} \delta_{\gamma\lambda}] \partial_j \\
&\quad + [(\partial_j V_\gamma^{b(0)}) V_\gamma^{a(0)} \delta_{\alpha\lambda} - (\partial_j V_\alpha^{b(0)}) V_\gamma^{a(0)} \delta_{\gamma\lambda}] \partial_i \\
&\quad - \delta_{\gamma\lambda} (\partial_i \partial_j V_\alpha^{b(0)}) V_\gamma^{a(0)}. \tag{5.15}
\end{aligned}$$

The first two terms of Eq. (5.13) correspond to the NMR response of Larmor precession of δS_α with frequency $\omega_L = \gamma H^{(0)}$. While the last two terms of Eq. (5.13) induce the NMR frequency shift, and they conventionally are called torque terms.

From Eq. (5.14) and Eq. (5.15), we found that torque terms are fully determined by the equilibrium textures of spin vectors. In our case with pseudo-random lattices of 2/4 spin solitons, this means the NMR frequency shifts are totally induced by equilibrium textures of spin solitons in 1D nexus objects. That's why the transverse NMR spectrum is perfect tool to observe the network of 1D nexus objects and network of KLS string wall. Taking into account the static magnetic field $\mathbf{H}^{(0)} = |\mathbf{H}^{(0)}| \hat{\mathbf{y}}$ and the parametrization Eq. (4.9), we can derive the dynamic response equations of transverse spin density

$$\delta S_+ = \frac{1}{\sqrt{2}} [\delta S_1(\omega) + i \delta S_3(\omega)] \tag{5.16}$$

under weak magnetic drive $\delta \mathbf{H}(t)$, see the detail of calculation in Appendix. C.3. This calculation gives

$$\begin{aligned}
(\omega^2 - \omega_L^2) \delta S_+(\omega) &= (\Xi_{11} + \Xi_{33}) \delta S_+(\omega) + i(\Xi_{13} - \Xi_{31}) \delta S_+(\omega) \\
&\quad - \left[\frac{1}{2} (C_{11} + C_{31}) - \frac{\chi_\perp}{\sqrt{2}\gamma} (\Xi_{33} + i\Xi_{13} - i\Xi_{31}) \right] \delta H_1(\omega). \tag{5.17}
\end{aligned}$$

Thus

$$\frac{\delta S_+(\omega)}{\delta H_1(\omega)} \propto \frac{1}{\omega^2 - \omega_L^2 - (\Xi_{11} + \Xi_{33}) - i(\Xi_{13} - \Xi_{31})}. \tag{5.18}$$

The poles of spin dynamic response function $\delta S_+ / \delta H_1$, which are determined by eigenequation

$$(\omega^2 - \omega_L^2) \delta S_+(\omega) = (\Xi_{11} + \Xi_{33}) \delta S_+(\omega) + i(\Xi_{13} - \Xi_{31}) \delta S_+(\omega), \tag{5.19}$$

correspond to the eigen-modes of transverse NMR frequency shift related to Larmor frequency induced by pseudo-random lattices of 1D nexus objects. We numerically solve this eigen-equation in next section with different D and $|q|$.

5.2 NMR of 1D nexus objects

For facilitating the numeric calculation, we firstly transform the spin dynamic eigenequation Eq. (5.19) into dimensionless form. All $\Xi_{\alpha\lambda}$ operators in Eq. (5.19) must be simplified with parametrization Eq. (4.9), See the details in Appendix. C.4. This

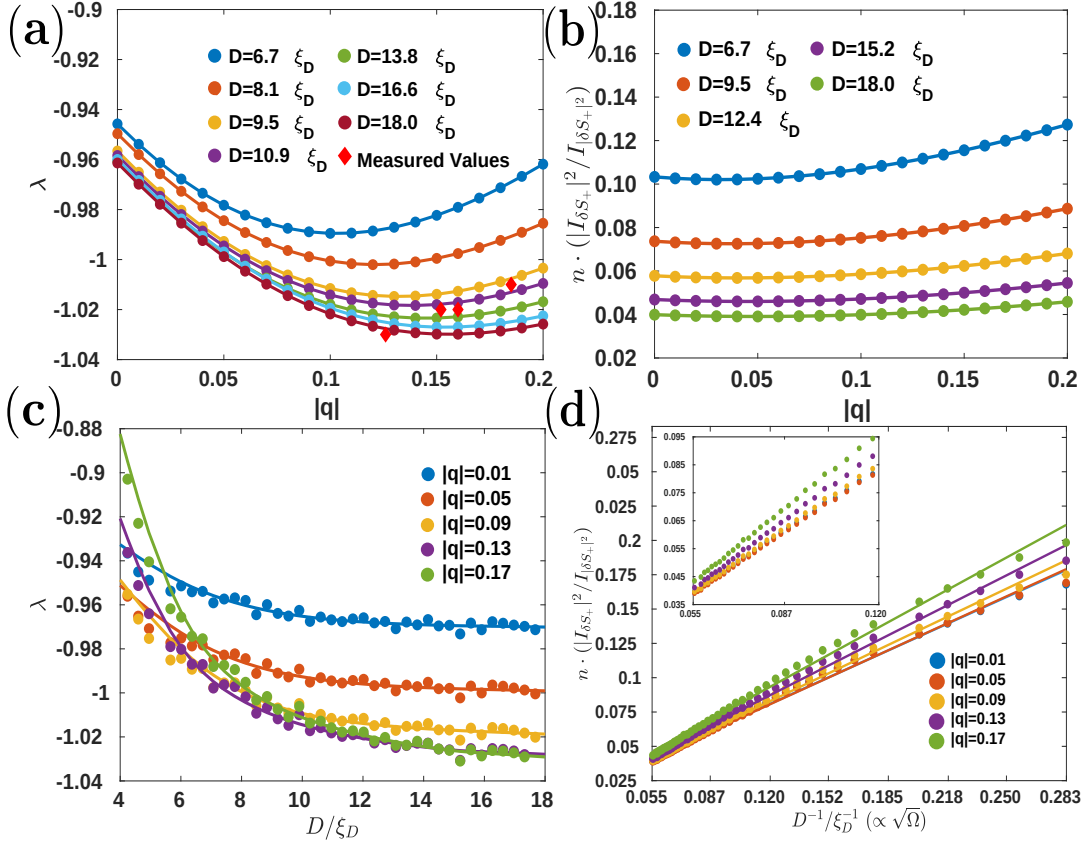


FIGURE 5.2: Transverse NMR frequency shifts λ and surface densities of ratio intensity $n \cdot (|I_{\delta S_+}|^2 / I_{\delta S_+}^2)$ of pseudo-random lattices consisting of inseparable spin solitons (π -solitons). The frequency shifts λ are eigenvalues of Eq. (5.20) with equilibrium textures of π -solitons in London limit. The surface densities of NMR ratio intensity are calculated by using Eq. (5.24). All scattering dots represent the original numeric results, while colored lines are smoothing spline fittings of these original numeric results. (a) Transverse NMR frequency shifts λ as functions of $|q|$ with different D . For large enough unit cells ($D > 10\xi_D$), we found λ decreases when $|q|$ increases as long as $|q| \leq 0.16$. The typical values of λ are around -1.015 to -1.03 when pseudo-random lattices model is good enough. This exactly coincides with the region of λ which was observed in experiment of Ref. [74], as shown via red diamonds. (b) depicts the surface densities of ratio intensity $n \cdot (|I_{\delta S_+}|^2 / I_{\delta S_+}^2)$ of the eigenmodes. (c) depicts the transverse frequency shifts λ as function of D . (d) The surface densities of ratio intensity $n \cdot (|I_{\delta S_+}|^2 / I_{\delta S_+}^2)$ as function of $1/D \propto \sqrt{\Omega}$. We found $n \cdot (|I_{\delta S_+}|^2 / I_{\delta S_+}^2)$ increases linearly if $\sqrt{\Omega}$ increases. This coincides with the results of experimental observation in Ref. [74]. The inset is the magnified plot between $1/D = 0.055$ till $1/D = 0.120$.

gives

$$\lambda \delta S_+(\omega) = \xi_D^2 [(6\rho_2^2 + \rho_1^2 + 1)\partial_y \partial_y + (3\rho_1^2 + 2\rho_2^2 + 1)\partial_x \partial_x - 2iV] \delta S_+(\omega) + U \delta S_+(\omega) \quad (5.20)$$

with

$$V = (1 + 3\rho_1^2 \cos 2\theta) \partial_x \theta \partial_x + (1 + \rho_1^2) \partial_y \theta \partial_y + \frac{1}{2\xi_D^2} [(1 + \rho_1)^2 \sin 2\theta - (1 + \rho_1) \rho_2 \cos \theta],$$

$$U = (1 + \rho_1) [-(1 + \rho_1) \cos 2\theta - 5\rho_2 \sin \theta] + 1 + \rho_1^2 + 4\rho_2^2, \quad (5.21)$$

where $\rho_1 = \Delta_{\perp 1}/\Delta_P$ and $\rho_2 = \Delta_{\perp 2}/\Delta_P$. Here the dimensionless eigenvalue

$$\lambda = \frac{(\omega^2 - \omega_L^2)}{\tilde{\Omega}^2} \quad (5.22)$$

is the transverse NMR frequency shift under weak magnetic drive and

$$\tilde{\Omega}^2 = \left(\frac{5\chi_{\perp}}{6\gamma^2 \Delta_P^2 g_D} \right)^{-1}. \quad (5.23)$$

We use the Galerkin strategy under finite-element partition to solve Eq. (5.20) [145], see details of algorithm see Appendix. B.3. The solving regions are the unit cells of pseudo-random lattices of 1D nexus objects. The equilibrium spin textures of pseudo-random lattices, which we got in Sec. 4.3.3, are directly used to solve Eq. (5.20). Because δH_{α} is low energy drive, we merely consider the spin dynamic response mode with the lowest λ of Eq. (5.20).

In addition, the ratio intensity of NMR signal is another observable besides the frequency shift λ . the scaling rule between ratio intensity and angular velocity Ω is a significant feature of the system. The surface density of ratio intensity, which is generated by unit area of pseudo-random lattices of 1D nexuses, is given as

$$n \cdot \frac{|I_{\delta S_+}|^2}{I_{|\delta S_+|^2}} = n \cdot \frac{|\int_{\sigma} \delta S_+ d\sigma|^2}{\int_{\sigma} |\delta S_+|^2 d\sigma}, \quad (5.24)$$

where $n = D^{-2}$ is the density of 1D nexuses and σ is area of one-half of unit cell of pseudo-random lattice.

We demonstrate the moduli of the lowest transverse spin dynamic response modes $|\delta S_+(\omega)|$ located in the unit cells of pseudo-random lattices of 1D nexus objects with inseparable and separable 2/4 spin solitons in Fig. 5.1. In the unit cell of pseudo-random lattice consisting of inseparable 2/4 spin soliton, the lowest spin dynamic response mode locates on the region which is occupied by π -soliton. While, in the unit cell of pseudo-random lattice consisting of separable 2/4 spin soliton, the lowest spin dynamic response mode locates on the region which is occupied by soliton ($|\Delta\theta| = \pi - 2\theta_0$). This means the KLS-soliton in the separable spin soliton does not respond the continuous-wave magnetic drive. The transverse NMR frequency shifts λ and surface densities of ratio intensity of pseudo-random lattices for inseparable and separable 2/4 spin solitons are shown in Fig. 5.2 and Fig. 5.3 respectively. Let's discuss them separately.

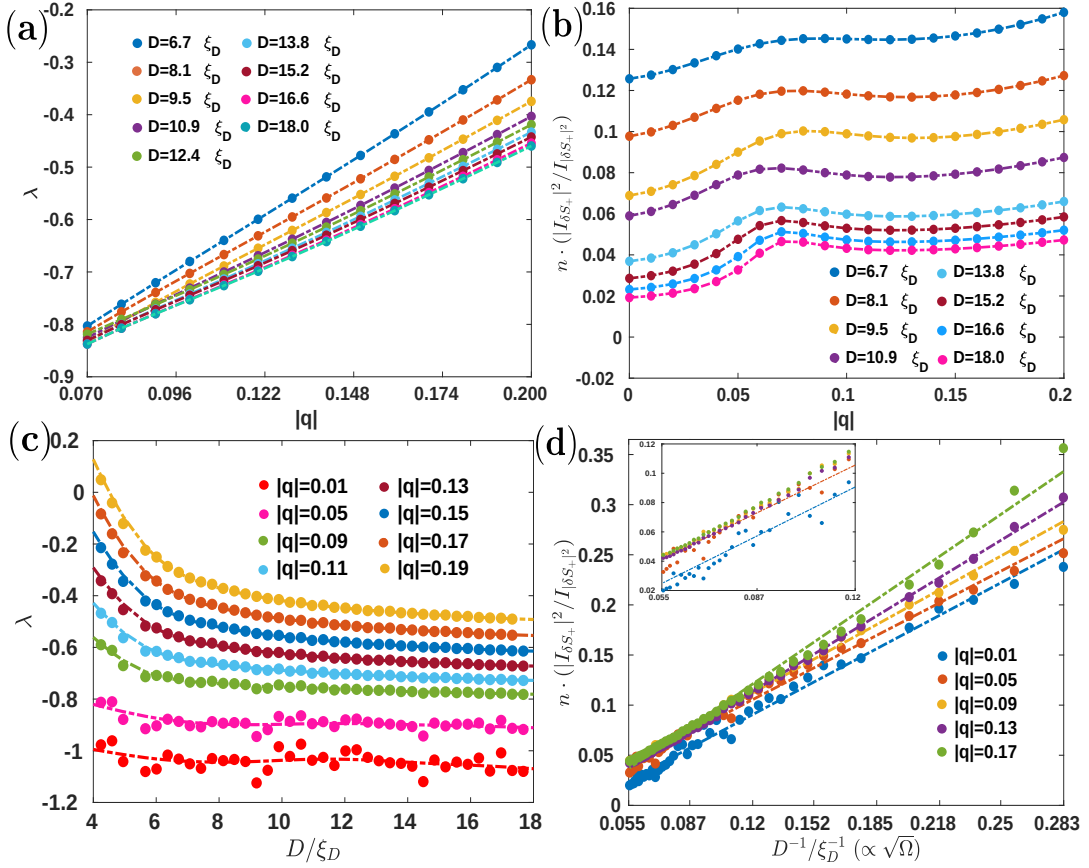


FIGURE 5.3: Transverse NMR frequencies shifts λ and surface densities of ratio intensity $n \cdot (|I_{\delta S_+}|^2 / I_{\delta S_+}^2)$ of pseudo-random lattices of separable spin solitons (KLS-solitons and solitons). The frequency shifts λ are eigenvalues of Eq. (5.20) with equilibrium textures of $1/4 + 1/4$ spin solitons in London limit. The surface densities of NMR ratio intensity are calculated by using Eq. (5.24). All scattering dots represent the original numeric results, while colored lines are smoothing spline fittings of these original numeric results. (a) Transverse NMR frequency shifts λ increases when $|q|$ increases. This is because only solitons ($|\Delta\theta| = \pi - 2\theta_0$) contribute to the lowest transverse spin dynamic response mode. When $|q|$ increases, λ generated by solitons increases, see the details in appendices Sec. D.2. The typical values of λ are larger than -0.9 when $D \geq 10\xi_D$. (b) depicts the surface densities of ratio intensity $n \cdot (|I_{\delta S_+}|^2 / I_{\delta S_+}^2)$ of the eigenmodes. (c) depicts the transverse frequency shifts λ as function of D . (d) The surface densities of ratio intensity $n \cdot (|I_{\delta S_+}|^2 / I_{\delta S_+}^2)$ as function of $1/D \propto \sqrt{\Omega}$. The inset is the magnified plot between $1/D = 0.055$ till $1/D = 0.120$.

5.2.1 Transverse NMR frequency shifts and surface densities of ratio intensity — inseparable spin solitons

The transverse NMR frequency shifts λ of pseudo-random lattices of inseparable spin solitons (π -solitons) exactly coincide with the observed values in the experiment of Ref. [74]. As been shown in Fig. 5.2 (a), the numeric values of λ generated by network of π -solitons is around -1.01 to -1.03 when pseudo-random lattice model is good enough i.e., $D \geq 10\xi_D$. In this case, the transverse NMR frequency shifts λ slightly increase as $|q|$ increasing when $|q| > 0.16$. This phenomenon has also been observed in experiment of Ref. [74]. The ratio intensities generated by unit area of pseudo-random lattice consisting of π -solitons linearly increase when the square root of angular velocity $\sqrt{\Omega} \propto 1/D$ increases, as shown in Fig. 5.2 (d). This coincides with the $\sqrt{\Omega}$ -scaling of satellite intensity observed in the experiment when $T = 0.38T_c$ ($|q| \approx 0.152$) [74].

In Sec. 4.3.4, based on the topological analysis and free energy calculations, we suggested the possible equilibrium state which was observed in experiment is the pseudo-random lattices of 2/4 inseparable spin solitons of 1D nexus objects network. Here we see the results of numeric simulations of transverse NMR spin dynamic response of this kind of pseudo-random lattices indeed coincide with the experimental observations.

5.2.2 Transverse NMR frequency shifts and surface densities of ratio intensity — separable spin solitons

In contrast with pseudo-random lattices consisting of inseparable 2/4 spin solitons, the transverse NMR frequency shifts of pseudo-random lattices consisting of separable spin solitons strongly deviate from the results of experimental observations, see Fig. 5.3 (a). λ increase when $|q|$ increases. This is because only the solitons ($|\Delta\theta| = \pi - 2\theta_0$) of separable spin solitons contribute to the transverse NMR frequency shift, and the frequency shifts λ of the soliton ($|\Delta\theta| = \pi - 2\theta_0$) increase as $|q|$ increases, see the details in Appendix. D.2. Moreover, the magnitudes of the surface densities of ratio intensity $n \cdot (|I_{\delta S_+}|^2 / I_{\delta S_+}^2)$ generated by pseudo-random lattices of separable spin solitons are larger than those generated by pseudo-random lattices consisting of inseparable spin solitons, as shown in Fig. 5.3 (d).

Chapter 6

Conclusion and Outlook

In this review, we discussed a series of significant results originated from fibration between vacuum manifolds of nafen-distorted superfluid ^3He . This fibration occurs in the vicinity of the second time symmetry breaking of two-step successive symmetry breaking phase transition from normal phase vacuum to PdB phase via polar phase. In this symmetry breaking pattern, any topological objects of the polar phase, which are described by $\pi_n(R_P)$, covert to the composite topological defects described by $\pi_n(R_1, R_2)$ in PdB phase because of the fibration. For the superfluid ^3He system, the possible composite topological defects are string monopole (Nambu monopole) and cosmological KLS string wall.

The ROTA group has experimentally observed the KLS string wall in nafen-distorted superfluid ^3He [74]. In chapter. 3, we demonstrated that in the vicinity of the second transition, such composite object is described by the relative homotopy groups $\pi_1(R_1, R_2)$ with length scale $r \leq \xi_H$. The reason for that is the existence of the two well separated length scales. The coherence length ξ , which relates to the symmetry breaking phase transition from the normal liquid to the polar phase, determines the core size of the half-quantum vortex (Alice cosmic string). The larger length scale $\xi/q \gg \xi$, which relates to the second symmetry breaking phase transition from the polar phase to the PdB phase, determines the soft core size of the KLS wall terminated by this string.

In the first time symmetry breaking from normal phase to polar phase, the vacuum manifold is R_P . After the second time symmetry breaking, the vacuum manifold of system turn to be R_1 . Because the fibration between R_1 and R_P , the topological objects of polar phase convert to the composite cosmological objects in PdB phase. While the submanifold R_2 of R_1 becomes to the fiber, which describes the vacuum manifold of PdB generated from a given element of R_P . In physics, this is equivalent to symmetry breaking of polar phase with fixed value of the order parameter vacuum to PdB phase. Thus the observed KLS domain wall terminated by the HQV is determined by the nontrivial element of $\pi_1(R_1, R_2)$, which isomorphic to $\pi_1(R_P)$. The other composite object, which is still waiting for observation, is the string monopole (hedgehog), which terminates the string (the spin vortex). Its topology is determined by the nontrivial element of $\pi_2(R_1, R_2) \cong \pi_2(R_P)$. The core of the monopole is of coherence length size ξ , while the spin vortices have the soft core of size $\xi/q \gg \xi$.

In the work from 1970s and later, the relative homotopy groups have been applied for classification of topological defects on the surface of the ordered system i.e., the boojum [110], and for classification of topological solitons terminated by point

or linear defects [91]. The topology of these combined objects demonstrates new application of the relative homotopy groups. Moreover, this applications for the successive symmetry breaking phase transition reveals the footage of deep algebraic topological concepts in the novel physical system.

Following the idea of group theory application, We also considered the more complicated object – the nexus, which combines the monopole, the string terminated by monopole, and skyrmion (topological soliton) terminated by the same monopole. Such object in the PdB phase arises in the presence of orientation energies i.e., magnetic energy, which provides magnetic length ζ_H . In other condensed system, such as superconductor-ferromagnet heterostructures, the objects combining vortices and skyrmions were recently considered. These objects were suggested contain Majorana bound states [146, 147].

As discussions in Chapter. 4 show, the nexus is powerful and useful tool, which allows the composite cosmological objects with high energies can be directly detected through low energy spin dynamics. We discussed in details that the topological origin of the novel 1D nexus objects in PdB phase of nafen-distorted ^3He superfluid. In contrast to the topological objects named 2D nexus objects which are similar but live in higher spatial dimension in PdB superfluid [97, 126–130], the network of 1D nexus objects have been directly detected in ROTA's NMR measurement [74].

The observation is supported not only by topological analysis but also by the calculations of equilibrium free energies and the spin dynamic response. For the superfluid ^3He distorted by nafen-strands, the locations of the HQVs are fixed once they appear during cooling down with a given angular velocity. In the limit of low angular velocity i.e., $\Omega \ll \Omega_c$, the average distance between pinned HQVs is around hundred microns. As a result, the KLS domain walls attached on the HQVs have very large geometric sizes when the symmetry breaking transition from polar phase to PdB phase occurs. In the spatial regions with length scales ζ_D , the SOC energy reduces the vacuum manifolds to discrete sets. The reduced vacuum manifolds have spin solitons, which are described by relative homotopy group $\pi_1(R_1^H, \tilde{R}_1^{SOC})$. Similar process also happens in bulk Helium-3 superfluid and spinor Bose condensate [101, 123, 124]. The textures of spin solitons with length scales ζ_D strongly influence the SOC energy and then modifies the low frequency NMR signals under continuous wave drive.

In Chapter. 4 and Chapter. 5, we proved the 2/4 spin solitons smoothly connected on every KLS string wall and form pseudo-random lattices in small angular velocity. The equilibrium configurations and the surface densities of equilibrium free energies of two different pseudo-random lattices with topological invariant 2/4 are numerically evaluated with self-developed non-linear optimization library. These two types of pseudo-random lattices correspond to two representations of group $G = \pi_1(S_S^1, \tilde{R}_2)$, the relative homotopy group of 2/4 spin solitons of 1D nexus objects. Our analysis shows the pseudo-random lattices of inseparable spin solitons are energy favorable. And we further calculated the transverse spin dynamic response under NMR continuous wave drive to compare with the experimental observations. The results of pseudo-random lattices consisting of inseparable spin solitons exactly coincide with the experimental measurements.

In the limit of low angular velocity, the pseudo-random lattices models work very well because the randomness of the network of 1D nexus objects doesn't influence the spin textures of spin solitons. This means the randomness and disorder introduced by nafen-aerogel are lost in the low angular velocity. However, when the angular velocity approaches the critic value Ω_c , the coupling between spin solitons may dramatically modify the equilibrium spin textures of random lattices of 1D nexus objects. In this case, the random distributions of KLS string wall lead to spin solitons glasses [139]. Thus we can expect the observable effects of this randomness on the NMR spectrums under high enough angular velocity. Moreover, PdB phase could be a good platform to observe the monopole-antimonopole networks because the string monopole is topologically protected by π_2 relative homotopy group [97]. These kinds of complex networks are predicted in condensed matter system and also in the Grand Unified Theories [118–122, 148–150]. The Grand Unified Theories may have a huge variety of networks consisting of monopoles and strings because of their complex symmetry breaking chains [151, 152]. In the absence of magnetic field, the string monopoles in PdB phase may connect to planar solitons with geometric size around ξ_D because of the reduction of vacuum manifold by SOC energy. Similar with pseudo-random lattices of spin solitons, these planar solitons may result in observable influence on NMR spectrum.

In summary, we demonstrated and reveled the significant influences of fibration between vacuum manifolds for a given symmetry breaking system. Similar phenomena may also occurs in other systems, in which the similar fibration of vacuum manifolds happens. For example, the ferroelectric nematic liquid crystal, which was observed recently [153] and the spinor Bose-Einstein condensate [154]. In fact the string-domain wall structure has been observed in the spin-1 Bose-Einstein condensate system. Another systems, in which the fibration mechanism could happens, are GUT models. In such kinds of models, the symmetry breaking patterns may be very complicated and may generate abundant novel results [151, 152].

Typically the state of the system with topological defects represents the excited state of the system. However, the topological defects can form the ground state. Earlier it was suggested that the suppression of the B-phase on the boundary of superfluid ^3He may lead to formation of stripe phase in $^3\text{He-B}$ under nanoscale confinement in a slab geometry [155]. On a microscopic level, this inhomogeneous phase is thought as the periodic array of the KLS domain walls between the degenerate states of the B-phase, see Refs. [106, 132]. Recently the experiments, which are suggested as the possible observation of such spatially modulated phase, has been reported [156, 157]. For nafen-distorted ^3He , similar situation may take place as well. The strands of nafen could play the same role as the boundaries in the slab confinement. The suppression of the order parameter near the strands may result in the spontaneous proliferation of the composite defects leading to the stripe phases or stripe glasses.

Appendix A

Fibration, Relative Homotopy Groups and Exact Sequences

A.1 Long and short exact sequences

The homotopy groups and relative homotopy groups of vacuum manifolds R_1 and R_2 form a long exact sequence (LES)

$$\dots \pi_k(R_2) \xrightarrow{i_*} \pi_k(R_1) \xrightarrow{j_*} \pi_k(R_1, R_2) \xrightarrow{\partial^*} \pi_{k-1}(R_2) \dots \quad (\text{A.1})$$

by the meaning of their definitions [107]. The exact sequence of (relative) homotopy groups means that the image of any homomorphism $x_*^n : A \rightarrow B$ of Eq. A.1 (the sets of the elements of the group B into which the elements of A are mapped) is the kernel of the next homomorphism $x_*^{n+1} : B \rightarrow C$ (the sets of the elements of B which are mapped to the zero element of C) i.e. $\text{im } x_*^n \cong \ker x_*^{n+1}$, with $n \in \mathbb{Z}$ [107].

The relative homotopy classes of $\pi_{k+1}(R_1, R_2)$ are mapped to the homotopy classes of $\pi_k(R_2)$ by mapping the k -dimension subset of $k+1$ sphere, which surrounds the defects, into R_2 . This mapping between two homotopy classes with different dimensions is called boundary homomorphism ∂_* [107]. Boundary homomorphism shows how topological objects with different dimensions connect to each other.

In principle, Eq. A.1 has infinite terms, thus Eq. A.1 is called LES. This make the calculation and analysis difficult. Then we need to split LES in to short exact sequences (SES) [112]. For every relative homotopy group $\pi_1(R_1, R_2)$, the LES can be split as

$$0 \rightarrow \text{im } j_* \xrightarrow{j_*} \pi_k(R_1, R_2) \xrightarrow{\partial^*} \text{im } \partial^* \rightarrow 0, \quad (\text{A.2})$$

by image of ∂^* and j_* . In this case, the relative homotopy group $\pi_k(R_1, R_2)$ is called as extension of $\text{im } j_*$ by $\text{im } \partial^*$.

A.1.1 LES and SES of $\pi_n(R_P)$

Exact sequence is a concept coming from category theory, this means there are many way to construct exact sequence of homotopy groups (of course, for others algebraic structures such as ring or domains). Here we demonstrate the exact sequence of $\pi_n(R_P)$ and use this exact sequence to get Eq. (2.14). Because $R_P \cong (S^2 \times U(1))/\mathbb{Z}_2$, the long sequence

$$\dots \pi_k(\mathbb{Z}_2) \rightarrow \pi_k(S^2 \times U(1)) \rightarrow \pi_k(R_P) \rightarrow \pi_{k-1}(\mathbb{Z}_2) \dots \quad (\text{A.3})$$

is exact. Thus we immediately get the SES

$$0 \rightarrow \mathbb{Z}^S \xrightarrow{j^*} \pi_2(R_P) \xrightarrow{m^*} 0 \rightarrow 0 \quad (\text{A.4})$$

of $\pi_2(R_P)$ and SES

$$0 \rightarrow \mathbb{Z}^\Phi \xrightarrow{n^*} \pi_1(R_P) \xrightarrow{f^*} \mathbb{Z}_2 \rightarrow 0 \quad (\text{A.5})$$

of $\pi_1(R_P)$. Equation. (A.4) simply means $\pi_2(R_P) = \mathbb{Z}^S$, while Eq. (A.5) suggests $\pi_1(R_P) = \tilde{\mathbb{Z}}$ such that $\pi_1(R_P)/\mathbb{Z}^\Phi \cong \mathbb{Z}_2$.

A.2 Extensions with and without magnetic field

A.2.1 No Magnetic Field

In the PdB phase the explicit form of exact sequence of homomorphisms is

$$\begin{array}{cccccccccccccccc} \pi_2(R_2) & \xrightarrow{i_*} & \pi_2(R_1) & \xrightarrow{j_*} & \pi_2(R_1, R_2) & \xrightarrow{\partial_*^k} & \pi_1(R_2) & \xrightarrow{m_*} & \pi_1(R_1) & \xrightarrow{n_*} & \pi_1(R_1, R_2) & \xrightarrow{\partial_*^p} & \pi_0(R_2) & \xrightarrow{q_*} & \pi_0(R_1) \\ \downarrow & & \downarrow & & \downarrow & & \downarrow & & \downarrow & & \downarrow & & \downarrow & & \downarrow \\ 0 & \xrightarrow{i_*} & 0 & \xrightarrow{j_*} & \mathbb{Z} & \xrightarrow{\partial_*^k} & \mathbb{Z} & \xrightarrow{m_*} & \mathbb{Z} \times \mathbb{Z}_2 & \xrightarrow{n_*} & \tilde{\mathbb{Z}} & \xrightarrow{\partial_*^p} & \mathbb{Z}_2 & \xrightarrow{q_*} & 0 \end{array} \quad (\text{A.6})$$

where the ∂_*^k and ∂_*^p are boundary homomorphisms. This gives the following relative homotopy groups: $\pi_2(R_1, R_2) \cong \mathbb{Z}$, $\pi_1(R_1, R_2) \cong \tilde{\mathbb{Z}}$ and $\pi_0(R_1, R_2) \cong 0$ as the fibration suggests. Then following Sec. A.1, we get the SES of $\pi_2(R_1, R_2)$

$$0 \rightarrow 0 \xrightarrow{j^*} \pi_2(R_1, R_2) \xrightarrow{\partial_*^k} 2\mathbb{Z} \rightarrow 0, \quad (\text{A.7})$$

and SES of $\pi_2(R_1, R_2)$

$$0 \rightarrow \mathbb{Z} \xrightarrow{n^*} \pi_1(R_1, R_2) \xrightarrow{\partial_*^p} \mathbb{Z}_2 \rightarrow 0. \quad (\text{A.8})$$

The boundary homomorphism ∂_*^k maps $S^1 \subset S^2$ to R_2 . Then the $\text{im } \partial_*^k$ describes all classes of string defects terminated by the monopoles. We found $\text{im } \partial_*^k = 2\mathbb{Z} \cong \mathbb{Z}$, which is the set of even numbers. This means that only the spin vortices with even winding number can form the string monopole. This situation is similar to the monopole connected with four HQVs in the A-phase, where the total winding number is 2 [115]. The topologically trivial monopole cannot connect with the string defects because of $\ker \partial_*^k \cong 0$. Actually this trivial class is identical to $\pi_2(R_1)$ because $\ker j_* \cong \text{im } i_* \cong 0$.

The ∂_*^p maps the homotopy classes of KLS string wall to homotopy classes of domain wall. From $\ker q_* \cong \text{im } \partial_*^p \cong \pi_0(R_2) \cong \mathbb{Z}_2$, we know there are domain walls bounded by string defects. The set of half-odd integers of the group $\tilde{\mathbb{Z}}$, which come from $\text{im } \partial_*^p$ describes the domain wall terminated by string defects – the KLS wall terminated by vortex with half-odd integer winding number $N = k + 1/2$. The vortices, which come from $\ker \partial_*^p \cong \mathbb{Z}$ are vortices with integer winding number. These vortices are free.

A.2.2 In the presence of magnetic field

In the presence of magnetic field the corresponding exact sequence is

$$\begin{array}{ccccccc} \pi_2(S^1 \times U(1)) & \xrightarrow{i_*} & \pi_2(R_1) & \xrightarrow{j_*} & \pi_2(R_1, S^1 \times U(1)) & \xrightarrow{\partial_*^k} & \pi_1(S^1 \times U(1)) \xrightarrow{m_*} \pi_1(R_1) \\ \downarrow & & \downarrow & & \downarrow & & \downarrow \\ 0 & \xrightarrow{i_*} & 0 & \xrightarrow{j_*} & \mathbb{Z} & \xrightarrow{\partial_*^k} & \mathbb{Z} \times \mathbb{Z} \xrightarrow{m_*} \mathbb{Z}_2 \times \mathbb{Z} \end{array} \quad (\text{A.9})$$

i.e. $\pi_2(R_1, S^1 \times U(1)) = 2\mathbb{Z} \cong \mathbb{Z}$ and the corresponding SES

$$0 \rightarrow 0 \xrightarrow{j_*} \pi_2(R_1, S^1 \times U(1)) \xrightarrow{\partial_*^k} 2\mathbb{Z} \rightarrow 0 \quad (\text{A.10})$$

From SES in Eq. (A.10) it follows that $\pi_2(R_1, S^1 \times U(1)) = 2\mathbb{Z}_2 \cong \mathbb{Z}$. We found $\ker \partial_*^k \cong 0$ and $\text{im } \partial_*^k = 2\mathbb{Z} \cong \mathbb{Z}$. That means that only those objects, which have an even total winding number of spin rotation, are topologically protected. These objects are the $\hat{\mathbf{d}}$ -vector skyrmions. Since $\pi_2(R_1, S^1 \times U(1)) \cong \pi_2(R_2, R_1)$, these $\hat{\mathbf{d}}$ -skyrmions can terminate on the $\hat{\mathbf{d}}$ -monopole, which in turn is the end point of spin vortices with the even number of spin rotation and is the linear analogs of the original point-like skyrmion [158, 159]. As a result one obtains the composite effect – the nexus in Fig. 3.6. The spin texture inside the cross-section D_2 of the skyrmion corresponds to continuous mapping to $SO_S(3)$, which is implemented by choosing first a direction of $\hat{\mathbf{d}}$, then making $SO_S(2)$ rotation of $\hat{\mathbf{e}}^1$ and $\hat{\mathbf{e}}^2$ around this direction. This skyrmion also represents the spin vortex with even winding number, because of $\text{im } \partial_*^k \cong 2\mathbb{Z}$ and $\ker \partial_*^k \cong 0$.

A.3 Fibration and a theorem

Fibration is a significant concepts of Homotopy theory [90]. Like most of modern mathematics, fibration can be described in a quite general language with the help of category theory. The category theory concept, which be used to define fibration, is the lift property or lifting property of a given continuous mapping. When this concept be mapped into homotopy theory, it gets a more explicit name i.e., the homotopy lifting property. In order to get an intuitive understanding of this concept, let's us imagine that we have a continuous mapping p between topological spaces E and B such that

$$p : E \rightarrow B, \quad (\text{A.11})$$

and B has a homotopy

$$f_t : X \times [0, 1] \mapsto B. \quad (\text{A.12})$$

Now, we introduce a new homotopy $\tilde{f}_t : X \times [0, 1] \mapsto E$ for E , such that

$$f_t = p \circ \tilde{f}_t, \quad f_0 = p \circ \tilde{f}_0. \quad (\text{A.13})$$

If such \tilde{f} really exists, then we say p has homotopy lifting property [90]. Furthermore, if p has homotopy lifting property respect to any topological space X , then p is named as fibration.

One classic example of fibration is the Hopf fibration between S^3 and S^2 . Here the fibration $p : S^3 \rightarrow S^2$ is Hopf mapping. Another example is Serre fibration between $SO(3)$ and S^2 . For this example, $SO(3)$ is universal covering space of S^2 . For

our case, the fibration between R_1 and R_p is quite similar with the case of Serre fibration i.e., $p : R_1 \rightarrow R_p$ is covering mapping and R_1 is covering space of R_p . As we have seen in Chapter. 3, with the help of the third isomorphism theorem, we indeed identified the covering mapping between R_1 and R_p .

For a given fibration, there is a theorem to describe the relations between the relative homotopy group $\pi_n(E, F)$ and homotopy group $\pi_k(B)$, where $F \subset E$ is the fiber [90].

- **Theorem** Given a fibration $p : E \rightarrow B$, points $b \in B$ and $e \in F : p^{-1}(b)$, there is an isomorphism $p_* : \pi_n(E, F, e) \rightarrow \pi_n(B, b)$.

Appendix B

Soblev Space, Non-Linear Optimization and Discrete Eigen-Value Problem

In Appdeix. B, we discuss the mathematical background and algorithm implements of numeric minimization of functional — the non-linear optimization. The motivation of this is using a mathematically reliable method to find out the equilibrium configurations of pseudo-random lattice of 1D nexus network. The solving domain is the unit cell of pseudo-random lattice. However, because there function θ is even respect to the y -direction of solving domain, the calculations are usually be practiced in one-half of unit cell. In this case, the stable configuration of θ is element of Helbert space of functions, which are defined on the solving domain [160]. Thanks for the Lax-Milgram lemma, there is one and only one solution for θ [160]. However, this is helpless to solve our problem, because it says nothing about how and where to find out this solution.

In this case, we introduce the new concept about function space i.e., the Sobolev space, which is subset of $C^m(\Omega)$ within domain Ω . The significant property of Sobolev space is it supports the weak derivatives of its elements. This means all elements of Sobolev space satisfy the Green integral formula — the high dimensional analog of integral by parts [160]. Based on the Sobolev space, the Ritz strategy and Galerkin strategy are developed, such that the former is suitable for functional minimization, while the latter is suitable for eigen-equation problem [160]. We start our discussion from Ritz strategy, then introduce the finite element partition of elements of Sobolev space. Finally we discuss how the Galerkin strategy be conducted for NMR eigen-equations. The main algorithm will be shown by pseudo-code and the Matlab script. The C++ code for calculation of sparse matrices of the square of derivative terms will be shown in last section .

B.1 Ritz strategy and finite elements partition

The Hilbert space on the solving domain is an infinite dimensional space, then it is impossible to deal with it by computer. The basic idea of Ritz strategy is choosing a subset S_N of Hilbert space to substitute the Hilbert space. S_N is the N -elements Sobolev space, then the θ function is expanded as

$$\theta = \sum_i^N c_i \phi_i(\mathbf{x}), \quad (\text{B.1})$$

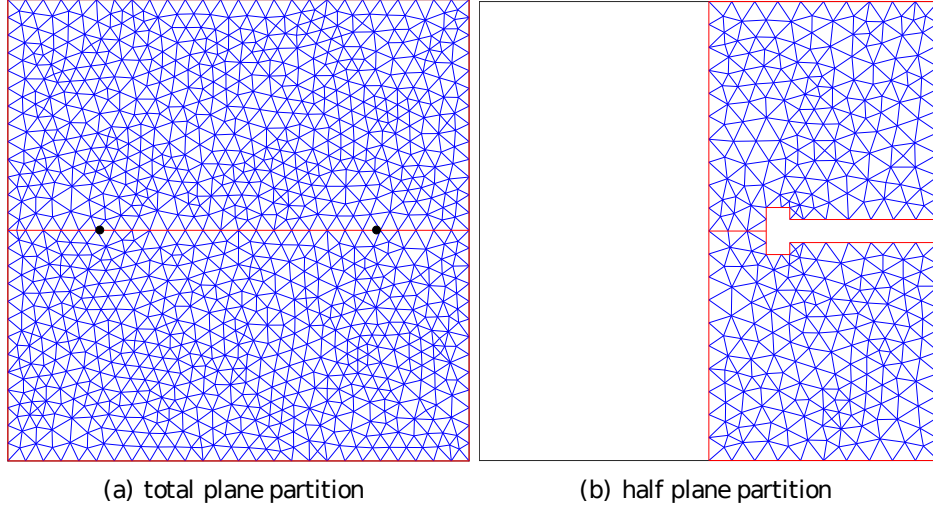


FIGURE B.1: Triangular elements partitions in unit cell of pseudo-random lattice. (a) The partition may be done for the whole unit cell, while (b) it also can be done for one-half of the unit cell. In most case, I used the partition (b) because it provide more higher points density than the manner (a).

where $\phi_i(\mathbf{x}) \in S_N$, $c_i \in \mathbb{C}$ and \mathbf{x} is space coordinates. Plugging Eq. (B.1) into the dimensionless London limit free energy Eq. (4.29), we get the finite-dimensional approximation

$$\begin{aligned} \tilde{F}(c_i)_{London} = & \frac{1}{\xi_D} \sum_{ij}^N \left\{ \int_{\Sigma} c_i c_j \left[\frac{1}{2} (\gamma_1 + 2\gamma_2) \partial_x \phi_i \partial_x \phi_j + \frac{1}{2} \gamma_1 \partial_y \phi_i \partial_y \phi_j \right] d\Sigma \right. \\ & \left. + \frac{1}{\xi_D^2} \int_{\Sigma} \left(-\frac{1}{2} \gamma_4 \cos 2 \sum_i^N c_i \phi_i - \gamma_3 \sin \sum_i^N c_i \phi_i \right) d\Sigma \right\} \end{aligned} \quad (\text{B.2})$$

of the continuous London limit free energy. Eq. (B.2) actually transfers the continuous solution θ over Σ to a discrete set of coefficients $c_1, c_2, c_3 \dots c_i \dots c_N$. We can get θ from Eq. (B.1) as long as we get c_i . Moreover, there is additional benefit of Eq. (B.2), that is Eq. (B.2) converts the free energy functional to a high dimensional function, which can be numerically minimized by non-linear optimization. In order to get c_i by using computer, we still need a properly chosen set of $\phi_i \in S_N$. And we hope ϕ_i could be as simple as possible.

This special set of ϕ_i is set of interpolation functions on triangular elements of finite elements (FE) partition [160]. In this manner, the solving domain is partitioned into small triangles as shown in Fig. B.1. Then Eq. (B.2) can be written as

$$\begin{aligned} \tilde{F}(c_i)_{London} = & \frac{1}{\xi_D} \sum_{ij}^N \sum_c \left\{ \int_c c_i c_j \left[\frac{1}{2} (\gamma_1 + 2\gamma_2) \partial_x \phi_i \partial_x \phi_j + \frac{1}{2} \gamma_1 \partial_y \phi_i \partial_y \phi_j \right] d\Sigma \right. \\ & \left. + \sum_c \frac{1}{\xi_D^2} \int_c \left(-\frac{1}{2} \gamma_4 \cos 2 \sum_i^N c_i \phi_i - \gamma_3 \sin \sum_i^N c_i \phi_i \right) d\Sigma, \right\} \end{aligned} \quad (\text{B.3})$$

where c represents the triangular element (cell) of the partition. The benefit of converting free energy functional into the form of Eq. (B.3) is we only need to deal the explicit form of ϕ_i on a small cell, other than on the whole solving domain. In this

situation, we can expect any element (e.g., θ for our problem) of S_N is a linear function on every c as long as they connect continuously with each other and c keeps be small. In most case, this element linear function is given as [160]

$$\theta^c = \sum_{\alpha}^3 c_{\alpha} \phi_{\alpha}^c, \quad (\text{B.4})$$

where

$$\phi_{\alpha}^c = \frac{1}{D}(\eta_{\alpha}x - \xi_{\alpha}y + \omega_{\alpha}), \quad D = \sum_{\alpha}^3 \omega_{\alpha} \quad (\text{B.5})$$

with

$$\begin{aligned} \xi_1 &= x_2 - x_3, \xi_2 = x_3 - x_1, \xi_3 = x_1 - x_2, \\ \eta_1 &= y_2 - y_3, \eta_2 = y_3 - y_1, \eta_3 = y_1 - y_2, \\ \omega_1 &= x_2y_3 - x_3y_2, \omega_2 = x_3y_1 - x_1y_3, \omega_3 = x_1y_2 - x_2y_1. \end{aligned} \quad (\text{B.6})$$

Plugging Eq. (B.4) into Eq. (B.3), and keep in mind that the coefficients c_{α} of cell should be reorganized as c_i of whole domain, we get

$$\tilde{F}(c_i)_{\text{London}} = \frac{1}{\xi_D} \sum_{ij}^N a_{ij} c_i c_j + \sum_c \frac{1}{\xi_D^2} \int_c \left(-\frac{1}{2} \gamma_4 \cos 2 \sum_{\alpha}^3 c_{\alpha} \phi_{\alpha}^c - \gamma_3 \sin \sum_{\alpha}^3 c_{\alpha} \phi_{\alpha}^c \right) d\Sigma, \quad (\text{B.7})$$

where a_{ij} is a sparse matrix and contains different summations of the quadratic integration in Eq. (B.3).

B.2 BFGS algorithm and implements

After the conversion of the continuous free energy functional to high-dimensional function in Eq. (B.7), we must consider how to minimize this function, which usually has 4000 to 6000 c_i . What we chosen is the popular BFGS algorithm [137]. As a quasi-Newtonian method, BFGS algorithm merely uses first order derivative and fast enough. The algorithm is given as The a_{ij} matrix is used for calculating the

Algorithm 1 BFGS iteration

Require: Given vector c_i^0 , $\epsilon > 0$ and unit matrix $H^0 = I$, and calculate the zeroth gradient $\partial_i \tilde{F}(c_i)$
while $\text{norm}(\partial_i \tilde{F}(c_i)) > \epsilon$ **do**
 $d_k \leftarrow -H_k \partial_i \tilde{F}(c_i)$
 Take single variable minimization for $\tilde{F}(c_i^k + \lambda_k d_k)$ to search λ_k
 $c_i^{k+1} \leftarrow c_i^k + \lambda_k d_k$
 calculate the $k+1$ th gradient $\partial_i \tilde{F}(c_i^{k+1})$
 make the BFGS modification for H^{k+1}
end while

gradient $\partial_i \tilde{F}(c_i)$ and λ_k -search, then a_{ij} actually has been gotten before the iteration starting. The iteration. 1 is conducted on Matlab and the a_{ij} is calculated by self-developed C++ library. The C++ code must be compiled to a sharing library in Matlab environment with supported g++ compiler, this is because Matlab has its own API for C++ program. In the last part of Sec. B.2. we show the matlab script and C++ code.

Here is the Matlab script of iteration. 1:

```
gkn1=gradient2DdSolitonWallQN(Cv,CbIv,A,...
    Thetakn1,elements,nodes,Np,gamma1,gamma);
while norm(gkn1)>tol
    dkn1=-Hkn1*gkn1;
    lambdakn1=fminsearch(@(lambda) PiThetaLambda(lambda,...
        A,Thetakn1,dkn1,Cv,CbIv,...
        elements,Nelem,nodes,Np,gamma1,...
        gamma),0);
    % search \lambda_{k}
    CV=[Cv CbIv]; thetakn1t=zeros(length(CV),1);
    for k=1:length(CV)
        thetakn1t(k,1)=Thetakn1(CV(k));
    end
    % take out all variables of $c_{i}$

    thetakt=thetakn1t+lambdakn1.*dkn1; % iteration
    Thetak=TransferVtoTheta2DSolitonWallQN(thetabw,...
        thetabu,thetabd,thetabiu,...
        thetabid,thetakt,CbW,Cbu,Cbd,...
        Cbiu,Cbid,CbIv,Cv,Thetakn1,Np,2);
    % refresh the solution

    %%%%%%%%% BFGS modification %%%%%%%%%
    skn1=thetakt-thetakn1t;
    gk=gradient2DdSolitonWallQN(Cv,CbIv,A,Thetak,...
        elements,nodes,Np,gamma1,gamma);
    ykn1=gk-gkn1; rhokn1=1./((ykn1')*skn1);
    Hk=InHassian2DSolitonQN(Is,rhokn1,skn1,ykn1,Hkn1);
    %%%%%%%%%
    Hkn1=Hk; Thetakn1=Thetak; gkn1=gk;
    % refresh H^{k} and gradient for next iteration
end
```

In this script, the functions *gradient2DdSolitonWallQN*, *PiThetaLambda* and *TransferVtoTheta2DSolitonWallQN* are all self-developed scripts, they can be found in my Github repository [161]. The implement of calculation for a_{ij} is a C++ class, which was named as "CalculateAMatrix". The head file is shown as

```
/*
 * this code is the header file of
 * c++ class AMatrixCalculator, which
 * gets elemnts and nodes array to
 * calculate the "A matrix"
 * the inputs are the pointer arraies
 * of element array (2D) and node array (2D)
 */

#ifdef calculateAMatrix_hpp
#define calculateAMatrix_hpp
#include <cstdint>
```

```

#include <iostream>

class CalculateAMatrix {
    int ** elementArrayPtr;
    double ** nodeArrayPtr;
    double ** AMatrixArrayPtr;
public:
    size_t lengthRowElement;
    size_t lengthColElement;
    size_t lengthRowNode;
    size_t lengthColNode;

    CalculateAMatrix(): lengthRowElement(0), lengthColElement(0),
                        elementArrayPtr(NULL), lengthRowNode(0),
                        lengthColNode(0), nodeArrayPtr(NULL) { };
    // default constructor to initilaze data member

    // pass in the elements array and node array
    void getAllArray(int ** array1ptr, double ** array2ptr,
                    const size_t rowDim1, const size_t colDim1,
                    const size_t rowDim2, const size_t colDim2);

    // Show what array have been passed in this "A-Matrix" calculator
    void showOriginalArr(int ** array1ptr, double ** array2ptr,
                        const size_t rowDim1, const size_t colDim1,
                        const size_t rowDim2, const size_t colDim2);

    void showObjectLocalArray();

    void AMatrixCalculatorRun();

    void showObjectLocalAMatrix();

    double ** const returnAMatrixPtr() const;

    // implements of member functions
    void CalculateAMatrix::getAllArray(int ** array1ptr,
                                       double ** array2ptr, const size_t rowDim1,
                                       const size_t colDim1, const size_t rowDim2,
                                       const size_t colDim2)
    {
        // make a object copy of Element array
        if (this->lengthRowElement == 0
            && this->lengthColElement == 0
            && this->elementArrayPtr == NULL){
            // allocate the row pointers array,
            // and allocate column array for every
            this->elementArrayPtr = new int * [rowDim1];
            for(size_t idx_row = 0; idx_row < rowDim1; ++idx_row)
            {
                elementArrayPtr[idx_row] = new int[colDim1];
            }
        }
    }

```

```

    }
}
// copy array element into the Object-local Element array
for (size_t idx_row = 0;
     idx_row < rowDim1; ++idx_row)
{
    for (size_t idx_col = 0;
         idx_col < colDim1; ++idx_col)
        this->elementArrayPtr[idx_row][idx_col]
            = array1ptr[idx_row][idx_col];
}
this->lengthRowElement = rowDim1;
this->lengthColElement = colDim1;
// make a object copy of Node array
if (this->lengthRowNode == 0
    && this->lengthColNode == 0
    && this->nodeArrayPtr == NULL)
{
    // allocate the row pointers array ,
    // and allocate column array for every
    // pointer elements of row pointer array.
    this->nodeArrayPtr = new double * [rowDim2];
    for(size_t idx_row = 0; idx_row < rowDim2; ++idx_row)
    {
        nodeArrayPtr[idx_row] = new double[colDim2];
    }
}

// copy array element into the Object-local Node array
for (size_t idx_row = 0; idx_row < rowDim2; ++idx_row)
{
    for (size_t idx_col = 0; idx_col < colDim2; ++idx_col)
        this->nodeArrayPtr[idx_row][idx_col]
            = array2ptr[idx_row][idx_col];
}
this->lengthRowNode = rowDim2;
this->lengthColNode = colDim2;
}

void CalculateAMatrix::showOriginalArr(int ** array1ptr,
double ** array2ptr, const size_t rowDim1,
const size_t colDim1, const size_t rowDim2,
const size_t colDim2)
{
    std::cout << "_first_pointer_to_pointer
of_original_Element_array:" << array1ptr << std::endl;
    std::cout << "_second_pointer_to_pointer
of_original_Node_array:" << array2ptr << std::endl;

    std::cout << "_Show_the_first_array_passed_in_" << std::endl;

```

```

    for(size_t rowidx = 0; rowidx < rowDim1; ++rowidx)
    {
        for(size_t colidx = 0; colidx < colDim1; ++colidx)
            std::cout << array1ptr[rowidx][colidx] << " ";
        std::cout << std::endl;
    }

    std::cout << "Show the second array passed in" << std::endl;
    for(size_t rowidx = 0; rowidx < rowDim2; ++rowidx)
    {
        for(size_t colidx = 0; colidx < colDim2; ++colidx)
            std::cout << array2ptr[rowidx][colidx] << " ";
        std::cout << std::endl;
    }
}

void CalculateAMatrix::showObjectLocalArray()
{
    std::cout << "pointer to pointer of Object-local Element array:"
        << elementArrayPtr << std::endl;
    for (size_t idx_row = 0; idx_row < lengthRowElement; ++idx_row)
    {
        for (size_t idx_col = 0;
            idx_col < lengthColElement; ++idx_col)
            std::cout <<
                this->elementArrayPtr[idx_row][idx_col] << " ";
        std::cout << std::endl;
    }

    std::cout << "pointer to pointer of Object-local Node array:"
        << nodeArrayPtr << std::endl;
    for (size_t idx_row = 0; idx_row < lengthRowNode; ++idx_row)
    {
        for (size_t idx_col = 0; idx_col < lengthColNode; ++idx_col)
            std::cout << this->nodeArrayPtr[idx_row][idx_col] << " ";
        std::cout << std::endl;
    }
}

// memeber function AMatrixCalculatorRun()
// is the main functionality of this class
// i.e., calculate the A Matrix with object-local arraies
void CalculateAMatrix::AMatrixCalculatorRun()
{
    std::cout << "calculator starts" << std::endl;
    // dynamically allocate the array of A-Matrix,
    // using pointer array for store the Row
    AMatrixArrayPtr = new double * [lengthRowNode];
    std::cout << "ptr array allocate successfully" << std::endl;
}

```

```

for(size_t idx_row = 0; idx_row < lengthRowNode; ++idx_row)
{
    AMatrixArrayPtr[idx_row] = new double[lengthRowNode];
}
std::cout << "_A-Mtrix_columns
allocate_successfully_" << std::endl;

// put 0.0 into the allocated A-Matrix, innitilization
for(size_t idx_row = 0; idx_row < lengthRowNode; ++idx_row)
{
    std::cout << "_assign_loop
1-level ,idx_row_is_"
    << idx_row << std::endl;
    for(size_t idx_col = 0;
        idx_col < lengthRowNode; ++idx_col)
    {
        std::cout << "_assign_loop_2-level ,
idx_col_is_" << idx_col << std::endl;
        AMatrixArrayPtr[idx_row][idx_col] = 0.0;
    }
}

std::cout << "_dynamical_allocated_successfull_" << std::endl;

// calculate the Matrix-elements and save
// the results into the initilized A-Matrix array
size_t idx_element = 0;
while( idx_element < lengthRowElement )
{
    std::cout << "_loop_start:
idx_element_is_" << idx_element << std::endl;

    // data prerparations
    int nodeIndex0Elem = elementArrayPtr[idx_element][0];
    int nodeIndex1Elem = elementArrayPtr[idx_element][1];
    int nodeIndex2Elem = elementArrayPtr[idx_element][2];
    int nodeIndex[] = {nodeIndex0Elem,
                      nodeIndex1Elem, nodeIndex2Elem};

    std::cout << "_node_indcies
with_idx_element_" << idx_element << std::endl;
    std::cout << "_nodeIndex_in_element_" << idx_element
    << "_are_" << nodeIndex[0] << "_" << nodeIndex[1]
    << "_" << nodeIndex[2] << std::endl;

    double x0 = nodeArrayPtr[nodeIndex0Elem][0];
    double y0 = nodeArrayPtr[nodeIndex0Elem][1];

    double x1 = nodeArrayPtr[nodeIndex1Elem][0];
    double y1 = nodeArrayPtr[nodeIndex1Elem][1];

```

```

double x2 = nodeArrayPtr[nodeIndex2Elem][0];
double y2 = nodeArrayPtr[nodeIndex2Elem][1];

// xi, eta, omega
double xi[] = {x1-x2, x2-x0, x0-x1};
double eta[] = {y1-y2, y2-y0, y0-y1};
double omega[] = {x1*y2-x2*y1, x2*y0-x0*y2, x0*y1-x1*y0};

double Di = 0; // initialization Di
    for(size_t i = 0; i < 3; ++i) { Di += omega[i]; }
double Si = (std::abs (Di))/2;

// Wall effect
// double gx = gamma1 + 2*gamma2;
// double gy = gamma1;
    double gx = 0.1;
    double gy = 0.05;

/*
    all data have been prepared, next is build
    the element matrix ax2ij, ay2ij, a2ij
*/

// define a 3 by 3 array for ax2ij
    double ax2ij[3][3] = {
        {0.0, 0.0, 0.0},
        {0.0, 0.0, 0.0},
        {0.0, 0.0, 0.0}
    };

// define a 3 by 3 array for ay2ij
    double ay2ij[3][3] = {
        {0.0, 0.0, 0.0},
        {0.0, 0.0, 0.0},
        {0.0, 0.0, 0.0}
    };

// define a 3 by 3 array for a2ij
    double a2ij[3][3] = {
        {0.0, 0.0, 0.0},
        {0.0, 0.0, 0.0},
        {0.0, 0.0, 0.0}
    };

// calculate ax2ij and ay2ij
    for(size_t o = 0; o < 3; ++o)
    {
        ax2ij[o][0] = (1.0/(2.0*(Di*Di)))*eta[o]*eta[0]*Si*gx;
        ax2ij[o][1] = (1.0/(2.0*(Di*Di)))*eta[o]*eta[1]*Si*gx;
        ax2ij[o][2] = (1.0/(2.0*(Di*Di)))*eta[o]*eta[2]*Si*gx;
    }

```

```
        ay2ij[o][0] = (1.0/(2.0*(Di*Di)))*xi[o]*xi[0]*Si*gy;
        ay2ij[o][1] = (1.0/(2.0*(Di*Di)))*xi[o]*xi[1]*Si*gy;
        ay2ij[o][2] = (1.0/(2.0*(Di*Di)))*xi[o]*xi[2]*Si*gy;
    }
    // a2ij = ax2ij + ay2ij
    for(size_t i = 0; i < 3; ++i)
    {
        for(size_t j = 0; j < 3; ++j)
        {
            a2ij[i][j] = ax2ij[i][j] + ay2ij[i][j];
        }
    }

    std::cout << "_a2ij_matrix_now_is_" << std::endl;
    for(size_t i = 0; i < 3; ++i)
    {
        for(size_t j = 0; j < 3; ++j)
            std::cout << a2ij[i][j] << "_";
        std::cout << std::endl;
    }

    // traspose the a2ij
    double a2ji[3][3] = {
        {0.0, 0.0, 0.0},
        {0.0, 0.0, 0.0},
        {0.0, 0.0, 0.0}
    };

    for(size_t i = 0; i < 3; ++i)
    {
        for(size_t j = 0; j < 3; ++j)
        {
            a2ji[j][i] = a2ij[i][j]; // matrix transpose
        }
    }

    std::cout << "_a2ji_matrix_now_is_" << std::endl;
    for(size_t i = 0; i < 3; ++i)
    {
        for(size_t j = 0; j < 3; ++j)
            std::cout << a2ji[i][j] << "_";
        std::cout << std::endl;
    }

    // symmetrize the element array
    double A2ij[3][3] = {
        {0.0, 0.0, 0.0},
        {0.0, 0.0, 0.0},
        {0.0, 0.0, 0.0}
    };
};
```



```

    for(size_t i = 0; i < 3; ++i)
    {
        for(size_t j = 0; j < 3; ++j)
        {
            A2ij[i][j] = (1.0/2.0)*(a2ij[i][j] + a2ji[i][j]);
            std::cout << A2ij[i][j] << "_and_"
                << (1/2)*(a2ij[i][j]+a2ji[i][j]) << std::endl;
        }
    }
    {
        for(size_t j = 0; j < 3; ++j)
            std::cout << A2ij[i][j] << "_";
        std::cout << std::endl;
    }

    // add the element results onto the A-Matrix array
    for(size_t row = 0; row < 3; ++row)
    {
        std::cout << "_row_is_" << row << std::endl;

        AMatrixArrayPtr[nodeIndex[row]][nodeIndex[0]]
            = A2ij[row][0]
              + AMatrixArrayPtr[nodeIndex[row]][nodeIndex[0]];
        AMatrixArrayPtr[nodeIndex[row]][nodeIndex[1]]
            = A2ij[row][1]
              + AMatrixArrayPtr[nodeIndex[row]][nodeIndex[1]];
        AMatrixArrayPtr[nodeIndex[row]][nodeIndex[2]]
            = A2ij[row][2]
              + AMatrixArrayPtr[nodeIndex[row]][nodeIndex[2]];

    }
    ++idx_element;
}

}

void CalculateAMatrix::showObjectLocalAMatrix()
{
    std::cout << "_pointer_to_pointer_of_Object-local\n\n"
        << "A-Matrix_array:" << AMatrixArrayPtr << std::endl;
    for (size_t idx_row = 0; idx_row < lengthRowNode; ++idx_row)
    {
        for (size_t idx_col = 0;
            idx_col < lengthRowNode; ++idx_col)
        {
            std::cout <<
                this->AMatrixArrayPtr[idx_row][idx_col] << "_";
            std::cout << std::endl;
        }
    }
}

// Here, you can define the return
// function as "const double **", but

```

```

// you can difine it as double ** const ,
// i.e., you can return const pointer ,
// but you can not require pointer to point const object
// double ** const Mat::returnPointerOfMatrix() const
// {
//     return this->arr;
// }

double ** const CalculateAMatrix::returnAMatrixPtr() const
{
    return this->AMatrixArrayPtr;
}

};
#endif

```

B.3 Garlkin strategy with finite element partition

In order to solve the eign-equation Eq. (5.20) by suing the expanded coefficients of θ in Sobolev space. We must expand δS_+ in Sobolev space as well. Similar with what we have talked in Sec. B.1, this operation coverts the partial differential Equation into a discrete form. Moreover, this discrete form of Eq. (5.20) is a high-dimensional linear equation systems, which looks like a matrix representation of quantum observable. The lowest eigen-value and eigen-mode of this linear system are what we want. This process is called Garlkin strategy [160]. With the FE partition in Sec. B.1, Eq. (5.20) can be rewritten as

$$\begin{aligned}
 \lambda \sum_c \sum_\alpha b_{\alpha\beta}^c \xi_\alpha = & \\
 & \sum_c \sum_\alpha \{ [6\gamma_2^2 + (\gamma_1^2 + 1)] a_{\alpha\beta}^{c,y} \\
 & + [3\gamma_1^2 + (2\gamma_2^2 + 1)] a_{\alpha\beta}^{c,x} + 2ia_{\alpha\beta}^{c,3} + 2i(1 + \gamma_1^2) a_{\alpha\beta}^{c,4} + a_{\alpha\beta}^{c,5} \} \xi_\alpha,
 \end{aligned} \tag{B.8}$$

where cell matrices $b_{\alpha\beta}^c, a_{\alpha\beta}^{c,y}, a_{\alpha\beta}^{c,x}, a_{\alpha\beta}^{c,3(4,5)}$ correspond to the cell integrals of terms on the right hand side of Eq. (5.20). After reorganizing all cell matrices and cell expansion coefficients ξ_α , we get the linear system

$$\lambda B_{ij} \xi_j = A_{ij} \xi_j, \tag{B.9}$$

where A_{ij} and B_{ij} are high dimensional spares matrices, which can be calculated by the same C++ library in Sec. B.2 and they form general eigen-value system. This kinds linear system can be directly solved by Matlab build-in function.

Appendix C

Simplifications of Eign-Equations

C.1 The derivation of the first order dynamic equation

Using Eq. (4.1), Eq. (4.2), Eq. (4.3) and Eq. (4.6), All terms of energy densities in hydrodynamic free energy $F_{hydrodynamics}$ are given as

$$\begin{aligned}
 f_{grad} = & \frac{1}{2} \{ K_1 \Delta_P^2 \partial_i \hat{d}_\alpha \partial_i \hat{d}_\alpha + K_1 \Delta_{\perp 1}^2 \partial_i \hat{e}_\alpha^1 \partial_i \hat{e}_\alpha^1 + K_1 \Delta_{\perp 2}^2 \partial_i \hat{e}_\alpha^2 \partial_i \hat{e}_\alpha^2 \\
 & + K_2 \Delta_P^2 \partial_j \hat{d}_\alpha \hat{z}_j \partial_i \hat{d}_\alpha \hat{z}_i + K_2 \Delta_{\perp 1}^2 \partial_j \hat{e}_\alpha^1 \hat{x}_j \partial_i \hat{e}_\alpha^1 \hat{x}_i + K_2 \Delta_{\perp 2}^2 \partial_j \hat{e}_\alpha^2 \hat{y}_j \partial_i \hat{e}_\alpha^2 \hat{y}_i \\
 & + K_3 \Delta_P^2 \partial_i \hat{d}_\alpha \hat{z}_i \partial_j \hat{d}_\alpha \hat{z}_j + K_3 \Delta_{\perp 1}^2 \partial_i \hat{e}_\alpha^1 \hat{x}_i \partial_j \hat{e}_\alpha^1 \hat{x}_j + K_3 \Delta_{\perp 2}^2 \partial_i \hat{e}_\alpha^2 \hat{y}_i \partial_j \hat{e}_\alpha^2 \hat{y}_j \\
 & + K_2 [\partial_j \hat{d}_\alpha \hat{z}_i \partial_j \hat{e}_\alpha^1 \hat{x}_j + \partial_j \hat{e}_\alpha^1 \hat{x}_i \partial_i \hat{d}_\alpha \hat{z}_j] \Delta_P \Delta_{\perp 1} + K_2 [\partial_j \hat{d}_\alpha \hat{z}_i \partial_i \hat{e}_\alpha^2 \hat{y}_j + \partial_j \hat{e}_\alpha^2 \hat{y}_i \partial_i \hat{d}_\alpha \hat{z}_j] \Delta_P \Delta_{\perp 2} \\
 & + K_2 [\partial_j \hat{e}_\alpha^1 \hat{x}_i \partial_i \hat{e}_\alpha^2 \hat{y}_j + \partial_j \hat{e}_\alpha^2 \hat{y}_i \partial_i \hat{e}_\alpha^1 \hat{x}_j] \Delta_{\perp 1} \Delta_{\perp 2} + K_3 [\partial_i \hat{d}_\alpha \hat{z}_i \partial_j \hat{e}_\alpha^1 \hat{x}_j + \partial_i \hat{e}_\alpha^2 \hat{x}_i \partial_j \hat{d}_\alpha \hat{z}_j] \Delta_P \Delta_{\perp 1} \\
 & + K_3 [\partial_i \hat{d}_\alpha \hat{z}_i \partial_j \hat{e}_\alpha^2 \hat{y}_j + \partial_i \hat{e}_\alpha^2 \hat{y}_i \partial_j \hat{d}_\alpha \hat{z}_j] \Delta_P \Delta_{\perp 2} + K_3 [\partial_i \hat{e}_\alpha^1 \hat{x}_i \partial_j \hat{e}_\alpha^2 \hat{y}_j + \partial_i \hat{e}_\alpha^2 \hat{y}_i \partial_j \hat{e}_\alpha^1 \hat{x}_j] \Delta_{\perp 1} \Delta_{\perp 2} \},
 \end{aligned} \tag{C.1}$$

$$\begin{aligned}
 f_{soc} = & \frac{3g_D}{5} \{ \Delta_P^2 (\hat{d}_i \hat{z}_i)^2 + \Delta_P \Delta_{\perp 1} (\hat{d}_i \hat{z}_i) (\hat{e}_j^1 \hat{x}_j) + \Delta_P \Delta_{\perp 2} (\hat{d}_i \hat{z}_i) (\hat{e}_j^2 \hat{y}_j) + \Delta_P \Delta_{\perp 1} (\hat{e}_i^1 \hat{x}_i) (\hat{d}_j \hat{z}_j) \\
 & + \Delta_{\perp 1}^2 (\hat{e}_i^1 \hat{x}_i)^2 + \Delta_{\perp 1} \Delta_{\perp 2} (\hat{e}_i^1 \hat{x}_i) (\hat{e}_j^2 \hat{y}_j) + \Delta_{\perp 2} \Delta_{\perp 1} (\hat{e}_i^2 \hat{y}_i) (\hat{d}_j \hat{z}_j) + \Delta_{\perp 2} \Delta_{\perp 1} (\hat{e}_i^2 \hat{y}_i) (\hat{e}_j^1 \hat{x}_j) \\
 & + \Delta_{\perp 2}^2 (\hat{e}_i^2 \hat{y}_i)^2 + \Delta_P^2 (\hat{d}_i \hat{z}_i)^2 + \Delta_P \Delta_{\perp 1} (\hat{d}_i \hat{x}_i) (\hat{e}_j^1 \hat{z}_j) \\
 & + \Delta_P \Delta_{\perp 2} (\hat{d}_i \hat{z}_j) (\hat{e}_j^2 \hat{y}_i) + \Delta_P \Delta_{\perp 1} (\hat{e}_i^1 \hat{x}_j) (\hat{d}_j \hat{z}_i) + \Delta_{\perp 1}^2 (\hat{e}_i^1 \hat{x}_i)^2 \\
 & + \Delta_{\perp 1} \Delta_{\perp 2} (\hat{e}_i^1 \hat{x}_j) (\hat{e}_j^2 \hat{y}_j) + \Delta_{\perp 2} \Delta_P (\hat{e}_i^2 \hat{y}_j) (\hat{d}_j \hat{z}_i) + \Delta_{\perp 1} \Delta_{\perp 2} (\hat{e}_i^2 \hat{y}_j) (\hat{e}_j^1 \hat{x}_i) + \Delta_{\perp 2}^2 (\hat{e}_j^2 \hat{y}_j)^2 \\
 & - \frac{2}{3} (\Delta_P^2 + \Delta_{\perp 1}^2 + \Delta_{\perp 2}^2) \},
 \end{aligned} \tag{C.2}$$

$$f_H = -\gamma H_\beta S_\beta + \frac{\gamma^2}{2} \chi_\perp^{-1} [(\hat{d}_\beta S_\beta)^2 \delta + S_\beta S_\beta]. \tag{C.3}$$

Then we have all of functional derivatives

$$\frac{\delta F_{hydrodynamics}}{\delta S_\beta}(\mathbf{r}') = \frac{\partial f_H}{\partial S_\beta}(\mathbf{r}') = -\gamma H_\beta + \gamma^2 \chi_\perp^{-1} [(S_\gamma \hat{d}_\gamma) \hat{d}_\beta \delta + S_\beta], \tag{C.4}$$

$$\begin{aligned}
\frac{\delta F_{hydrodynamics}}{\delta \hat{d}_\beta}(\mathbf{r}') &= \frac{\partial f_H}{\partial \hat{d}_\beta}(\mathbf{r}') + \frac{\partial f_{soc}}{\partial \hat{d}_\beta}(\mathbf{r}') - \partial_i \frac{f_{grad}}{\partial \partial_i \hat{d}_\beta}(\mathbf{r}') \\
&= \gamma^2 \chi_\perp^{-1} \delta S_\gamma \hat{d}_\gamma S_\beta + \frac{3g_D}{5} (2\Delta_P^2 \hat{d}_\gamma \hat{z}_\gamma \hat{z}_\beta + \Delta_P \Delta_{\perp 1} \hat{z}_\beta \hat{e}_i^1 \hat{x}_i + \Delta_P \Delta_{\perp 2} \hat{z}_\beta \hat{e}_i^2 \hat{y}_i \\
&\quad + \Delta_P \Delta_{\perp 1} \hat{z}_\beta \hat{e}_i^1 \hat{x}_i + \Delta_P \Delta_{\perp 2} \hat{z}_\beta \hat{e}_i^2 \hat{y}_i + 2\Delta_P^2 \hat{d}_\gamma \hat{z}_\gamma \hat{z}_\beta + \Delta_P \Delta_{\perp 1} \hat{z}_i \hat{e}_i^1 \hat{x}_\beta \\
&\quad + \Delta_P \Delta_{\perp 2} \hat{z}_i \hat{e}_i^2 \hat{y}_\beta + \Delta_P \Delta_{\perp 1} \hat{x}_\beta \hat{e}_i^1 \hat{z}_i + \Delta_P \Delta_{\perp 2} \hat{z}_i \hat{e}_i^2 \hat{y}_\beta) \\
&\quad - \frac{1}{2} (K_1 \Delta_P^2 2\partial_i \partial_i \hat{d}_\beta + K_2 \Delta_P^2 2\partial_i \partial_j \hat{d}_\beta \hat{z}_i \hat{z}_j \\
&\quad + 2K_2 \Delta_P \Delta_{\perp 1} \partial_i \partial_j \hat{e}_\beta^1 \hat{z}_j \hat{x}_i + 2K_2 \Delta_P \Delta_{\perp 2} \partial_i \partial_j \hat{e}_\beta^2 \hat{z}_j \hat{y}_i \\
&\quad + 2K_3 \Delta_P^2 \partial_i \partial_j \hat{d}_\beta \hat{z}_j \hat{z}_i + 2K_3 \Delta_P \Delta_{\perp 1} \hat{z}_i \partial_j \hat{e}_\beta^1 \hat{x}_j + 2K_3 \Delta_P \Delta_{\perp 1} \partial_i \hat{e}_\beta^2 \hat{y}_j \hat{z}_i), \tag{C.5}
\end{aligned}$$

$$\begin{aligned}
\frac{\delta F_{hydrodynamics}}{\delta \hat{e}_\beta^1}(\mathbf{r}') &= \frac{\partial f_{soc}}{\partial \hat{e}_\beta^1}(\mathbf{r}') - \partial_i \frac{f_{grad}}{\partial \partial_i \hat{e}_\beta^1}(\mathbf{r}') \\
&= \frac{3g_D}{5} (\Delta_P \Delta_{\perp 1} \hat{d}_\gamma \hat{z}_\gamma \hat{x}_\beta + \Delta_P \Delta_{\perp 1} \hat{d}_\gamma \hat{z}_\gamma \hat{x}_\beta + 2\Delta_{\perp 1}^2 \hat{e}_\gamma^1 \hat{x}_\gamma \hat{x}_\beta \\
&\quad + \Delta_{\perp 1} \Delta_{\perp 2} \hat{e}_\gamma^2 \hat{y}_\gamma \hat{x}_\beta + \Delta_P \Delta_{\perp 1} \hat{d}_\gamma \hat{x}_\gamma \hat{z}_\beta + \Delta_P \Delta_{\perp 1} \hat{d}_\gamma \hat{x}_\gamma \hat{z}_\beta \\
&\quad + \Delta_{\perp 1}^2 2\hat{e}_\gamma^1 \hat{x}_\gamma \hat{x}_\beta + \Delta_{\perp 1} \Delta_{\perp 2} \hat{e}_\gamma^2 \hat{x}_\gamma \hat{y}_\beta + \Delta_{\perp 2} \Delta_{\perp 1} \hat{e}_\gamma^2 \hat{y}_\gamma \hat{x}_\beta + \Delta_{\perp 2} \Delta_{\perp 1} \hat{e}_\gamma^2 \hat{x}_\gamma \hat{y}_\beta) \\
&\quad - \frac{1}{2} (2K_1 \Delta_{\perp 1}^2 \partial_i \partial_i \hat{e}_\beta^1 \hat{x}_j \hat{x}_j + 2K_2 \Delta_{\perp 1}^2 \partial_i \partial_j \hat{e}_\beta^1 \hat{x}_j \hat{x}_i + 2K_2 \Delta_P \Delta_{\perp 1} \partial_i \partial_j \hat{d}_\beta \hat{x}_j \hat{z}_i \\
&\quad + 2K_2 \Delta_{\perp 1} \Delta_{\perp 2} \partial_i \partial_j \hat{e}_\beta^2 \hat{x}_j \hat{y}_i \\
&\quad + 2K_3 \Delta_{\perp 1}^2 \partial_i \partial_j \hat{e}_\beta^1 \hat{x}_j \hat{x}_i + 2K_3 \Delta_P \Delta_{\perp 1} \partial_i \partial_j \hat{d}_\beta \hat{z}_j \hat{x}_i + 2K_3 \Delta_{\perp 1} \Delta_{\perp 2} \partial_i \partial_j \hat{e}_\beta^2 \hat{y}_j \hat{x}_i), \tag{C.6}
\end{aligned}$$

$$\begin{aligned}
\frac{\delta F_{hydrodynamics}}{\delta \hat{e}_\beta^2}(\mathbf{r}') &= \frac{\partial f_{soc}}{\partial \hat{e}_\beta^2}(\mathbf{r}') - \partial_i \frac{f_{grad}}{\partial \partial_i \hat{e}_\beta^2}(\mathbf{r}') \\
&= \frac{3g_D}{5} (\Delta_P \Delta_{\perp 2} \hat{d}_\gamma \hat{z}_\gamma \hat{y}_\beta + \Delta_P \Delta_{\perp 2} \hat{e}_\gamma^1 \hat{x}_\gamma \hat{y}_\gamma + \Delta_{\perp 2} \Delta_P \hat{y}_\beta \hat{d}_\gamma \hat{z}_\gamma \\
&\quad + \Delta_{\perp 2} \Delta_{\perp 1} \hat{e}_\gamma^1 \hat{x}_\gamma \hat{y}_\beta + 2\Delta_{\perp 2}^2 \hat{e}_\gamma^2 \hat{y}_\gamma \hat{y}_\beta + \Delta_P \Delta_{\perp 2} \hat{d}_\gamma \hat{y}_\gamma \hat{z}_\beta \\
&\quad + \Delta_{\perp 1} \Delta_{\perp 2} \hat{e}_\gamma^1 \hat{y}_\gamma \hat{x}_\beta + \Delta_{\perp 2} \Delta_P \hat{d}_\gamma \hat{y}_\gamma \hat{z}_\beta + \Delta_{\perp 1} \Delta_{\perp 2} \hat{e}_\gamma^1 \hat{y}_\gamma \hat{x}_\beta + \Delta_{\perp 2}^2 2\hat{e}_\gamma^2 \hat{y}_\gamma \hat{y}_\beta) \\
&\quad - \frac{1}{2} (2K_1 \Delta_{\perp 2}^2 \partial_i \partial_i \hat{e}_\beta^2 \hat{y}_j \hat{y}_j + 2K_2 \Delta_{\perp 2}^2 \partial_i \partial_j \hat{e}_\beta^2 \hat{y}_j \hat{y}_i + 2K_2 \Delta_P \Delta_{\perp 2} \partial_i \partial_j \hat{d}_\beta \hat{y}_j \hat{z}_i \\
&\quad + 2K_2 \Delta_{\perp 1} \Delta_{\perp 2} \partial_i \partial_j \hat{e}_\beta^1 \hat{y}_j \hat{x}_i \\
&\quad + 2K_3 \Delta_{\perp 2}^2 \partial_i \partial_j \hat{e}_\beta^2 \hat{y}_j \hat{y}_i + 2K_3 \Delta_P \Delta_{\perp 1} \partial_i \partial_j \hat{d}_\beta \hat{z}_j \hat{y}_i \\
&\quad + 2K_3 \Delta_{\perp 1} \Delta_{\perp 2} \partial_i \partial_j \hat{e}_\beta^1 \hat{x}_j \hat{y}_i). \tag{C.7}
\end{aligned}$$

Plugging Eq. (C.4), Eq. (C.5), Eq. (C.6) and Eq. (C.7) into Eq. (5.4) and Eq. (5.5), we get Eq. (5.7) and Eq. (5.8).

C.2 The derivation of the second order dynamic response equation

Firstly we take time-derivative to Eq. (5.7) and get

$$\begin{aligned} \gamma \epsilon_{\alpha\beta\gamma} (H_\beta^{(0)} \frac{\partial}{\partial t} \delta S_\gamma + \frac{\partial}{\partial t} \delta H_\beta S_\gamma^{(0)}) = \\ \epsilon_{\alpha\beta\gamma} [-\frac{6g_D}{5} Q_{\beta j}^{bd} (V_j^{d(0)} \frac{\partial}{\partial t} \delta V_\gamma^b + \frac{\partial}{\partial t} \delta V_j^d V_\gamma^{b(0)}) \\ + K_{ij}^{ba} (\partial_i \partial_j V_\beta^{b(0)} \frac{\partial}{\partial t} \delta V_\gamma^a + \partial_i \partial_j \frac{\partial}{\partial t} \delta V_\beta^b V_\gamma^{a(0)})], \end{aligned} \quad (C.8)$$

where

$$\begin{aligned} \frac{\partial}{\partial t} \delta V_\alpha^a = & \{ H_\beta^{(0)} V_\gamma^{a(0)} \gamma + \gamma H_\beta^{(0)} \delta V_\gamma^a + \gamma \delta H_\beta V_\gamma^{a(0)} \\ & - \gamma^2 \chi_\perp^{-1} \delta (S_\eta^{(0)} V_\eta^{3(0)}) (V_\beta^{3(0)} \delta V_\gamma^a + V_\gamma^{3(0)} \delta V_\beta^3) \\ & + \gamma^2 \chi_\perp^{-1} (S_\beta^{(0)} V_\gamma^{a(0)} + S_\beta^{(0)} \delta V_\gamma^a + \delta S_\beta V_\gamma^{a(0)}) \} \epsilon_{\alpha\beta\gamma}. \end{aligned} \quad (C.9)$$

Taking into account the relations:

$$\gamma S_\beta^{(0)} = H_\alpha^{(0)} \chi_{\alpha\beta}, \quad V_\eta^{3(0)} S_\eta^{(0)} = \hat{\mathbf{d}}^{(0)} \cdot \mathbf{S}^{(0)} = 0, \quad (C.10)$$

where magnetic susceptibility $\chi_{\alpha\beta} = \chi_\parallel \delta_{\alpha\beta} - (\chi_\perp - \chi_\parallel) \hat{d}_\alpha^{(0)} \hat{d}_\beta^{(0)}$, Eq. (C.9) is simplified to

$$\frac{\partial}{\partial t} \delta V_\alpha^a = \epsilon_{\alpha\beta\gamma} V_\gamma^{a(0)} (\gamma \delta H_\beta^{a(0)} - \gamma^2 \chi_\perp^{-1} \delta S_\beta) \quad (C.11)$$

Taking Eq. (C.11) back into Eq. (C.8), we get

$$\frac{\partial^2}{\partial t^2} \delta S_\alpha = \gamma \epsilon_{\alpha\beta\gamma} (H_\beta^{(0)} \frac{\partial}{\partial t} \delta S_\gamma + \frac{\partial}{\partial t} \delta H_\beta S_\gamma^{(0)}) + \Xi_{\alpha\lambda} \delta S_\lambda + C_{\alpha\eta} \delta H_\eta. \quad (C.12)$$

The last step is taking time Fourier transformation for dynamic variables δS_α and δH_β as well their derivatives

$$\begin{aligned} \delta H_\beta(\omega) = \frac{1}{\sqrt{2\pi}} \int dt \delta H_\beta e^{-i\omega t}, \quad \delta S_\alpha(\omega) = \frac{1}{\sqrt{2\pi}} \int dt \delta S_\alpha e^{-i\omega t}, \\ \mathfrak{F}(\frac{\partial}{\partial t} \delta H_\beta) = i\omega \delta H_\beta(\omega), \quad \mathfrak{F}(\frac{\partial}{\partial t} \delta S_\alpha) = i\omega \delta S_\alpha(\omega), \quad \mathfrak{F}(\frac{\partial^2}{\partial t^2} \delta S_\alpha) = -\omega^2 \delta S_\alpha(\omega) \end{aligned} \quad (C.13)$$

in Eq. (C.12), this gives out Eq. (5.13).

C.3 The derivation of transverse NMR response equation

In the limit of $|\omega - \omega_L| \ll \omega_L$ and under parametrization Eq. (4.9), Eq. (5.13) within components form are

$$\begin{aligned} i\omega\delta S_2(\omega) &= -\gamma S_3^{(0)}\delta H_1(\omega), \\ i\omega\delta S_1(\omega) &= \gamma H_2^{(0)}\delta S_3(\omega) + \frac{\Xi_{11}}{i\omega}\delta S_1(\omega) + \frac{\Xi_{13}}{i\omega}\delta S_3(\omega) + \frac{C_{31}}{i\omega}\delta H_1(\omega), \\ i\omega\delta S_3(\omega) &= \gamma[S_2^{(0)}\delta H_1(\omega) - H_2^{(0)}\delta S_1(\omega)] + \frac{\Xi_{31}}{i\omega}\delta S_1(\omega) + \frac{\Xi_{33}}{i\omega}\delta S_3(\omega) + \frac{C_{31}}{i\omega}\delta H_1(\omega). \end{aligned} \quad (C.14)$$

We expand ω around ω_L as $\omega = \omega_L + \epsilon + O^2(\epsilon)$, then we get

$$\delta S_1(\omega) = \frac{\delta S_3(\omega)}{i(1+\epsilon)}, \quad \delta S_3(\omega) = \frac{1}{i(1+\epsilon)}\left(\frac{\chi_\perp}{\gamma}\delta H_1(\omega) - \delta S_1(\omega)\right), \quad (C.15)$$

where $\epsilon = (\omega - \omega_L)$. By multiplying $i\omega$ and utilizing Eq. (C.15), Eq. (C.14) can be reorganized as

$$\begin{aligned} (\omega^2 - \omega_L^2)(\delta S_1(\omega) + i\delta S_3(\omega)) &= i[-\Xi_{31}\left(\frac{\delta S_1}{1+2\epsilon} + i\frac{\delta S_3}{1+2\epsilon}\right) + \Xi_{13}\left(\frac{\delta S_1}{1+2\epsilon} + i\delta S_3\right)] \\ &\quad + \frac{\Xi_{11}}{1+\epsilon}(\delta S_1 + i\delta S_3) + \frac{\Xi_{33}}{1+\epsilon}(\delta S_1 + i\delta S_3) \\ &\quad - (C_{11} + iC_{31})\delta H_1 - \frac{\chi_\perp}{\gamma}\left(\frac{\Xi_{33}}{1+\epsilon} + i\frac{\Xi_{13}}{1+2\epsilon} - i\frac{\Xi_{31}}{1+2\epsilon}\right)\delta H_1. \end{aligned} \quad (C.16)$$

In the case of $\epsilon \rightarrow 0$, this gives Eq. (5.17).

C.4 All $\Xi_{\alpha\lambda}$ terms in Eq. (5.19)

By utilizing Eq. (5.14) and parametrization Eq. (4.9), we have

$$\begin{aligned} \Xi_{11} + \Xi_{33} &= [2c_1(K_1 + K_2 + K_3)\Delta_{\perp 2}^2 + c_1K_1(\Delta_{\perp 1}^2 + \Delta_P^2)]\partial_y\partial_y\delta S_+ \\ &\quad + [c_1(K_1 + K_2 + K_3)\Delta_{\perp 1}^2 + c_1K_1(2\Delta_{\perp 2}^2 + \Delta_P^2)]\partial_x\partial_x\delta S_+ \\ &\quad + c_2(\Delta_P + \Delta_{\perp 1})[-(\Delta_{\perp 1} + \Delta_P)\cos 2\theta - 5\Delta_{\perp 2}\sin\theta] + c_2(\Delta_P^2 + \Delta_{\perp 1}^2 + 4\Delta_{\perp 2}^2), \end{aligned} \quad (C.17)$$

$$\begin{aligned} \Xi_{13} + \Xi_{31} &= -2c_1K_1\Delta_P^2\partial_i\delta S_+\partial_i\theta - 2c_1\Delta_{\perp}^2[K_1\partial_y\delta S_+\partial_y\theta + (K_1 + K_2 + K_3)\partial_x\delta S_+\partial_x\theta\cos 2\theta] \\ &\quad - c_1\{[K_1\Delta_P^2 + (K_1 + K_2 + K_3)\Delta_{\perp 1}^2]\partial_x\partial_x\theta + K_1(\Delta_P^2 + \Delta_{\perp 1}^2)\partial_y\partial_y\theta\}, \end{aligned} \quad (C.18)$$

where

$$c_1 = \frac{\gamma^2}{\chi_\perp}, \quad c_2 = \frac{6g_D\gamma^2}{5\chi_\perp}. \quad (C.19)$$

plugging Eq. (C.18), Eq. (C.19) into Eq. (5.19) and multiplying $\tilde{\Omega}^{-2}$ on both sides, we get

$$\begin{aligned} \frac{\omega^2 - \omega_L^2}{\tilde{\Omega}^2} \delta S_+ = & \left\{ \frac{5}{6g_D} [6K_1\rho_2^2 + K_1(\rho_1^2 + 1)] \partial_y \partial_y + \frac{5}{6g_D} [3K_1\rho_1^2 + K_1(2\rho_2^2 + 1)] \partial_x \partial_x \right. \\ & - i \frac{10}{6g_D} [(K_1 + 3\rho_1^2 K_1 \cos 2\theta) \partial_x \theta \partial_x - K_1(1 + \rho_1^2) \partial_y \theta \partial_y] \} \delta S_+ \quad (\text{C.20}) \\ & - i \frac{5}{6g_D} [K_1(1 + 3\rho_1^2) \partial_x \partial_x \theta + K_1(1 + \rho_1^2) \partial_y \partial_y \theta] \delta S_+ \\ & + \{ (1 + \rho_1) [-(1 + \rho_1) \cos 2\theta - 5\rho_2 \sin \theta] + (1 + \rho_1^2 + 4\rho_2^2) \} \delta S_+. \end{aligned}$$

To simplify Eq. (C.20), we need the Lagrangian equation of θ

$$\begin{aligned} \frac{\delta F_{\text{London}}(\theta)}{\delta \theta} = & c_1 \{ [K_1 \Delta_P^2 + (K_1 + K_2 + K_3) \Delta_{\perp 1}^2] \partial_x \partial_x \theta + K_1 (\Delta_P^2 + \Delta_{\perp 1}^2) \partial_y \partial_y \theta \} \\ & - c_2 \{ \Delta_{\perp 2} (\Delta_P + \Delta_{\perp 1}) \cos \theta + (\Delta_P + \Delta_{\perp 1})^2 \sin 2\theta \} = 0. \quad (\text{C.21}) \end{aligned}$$

This equation can be simplified to

$$(1 + 3\rho_1^2) \partial_x \partial_x \theta + (1 + \rho_1^2) \partial_y \partial_y \theta = \frac{1}{\tilde{\zeta}_D^2} [(1 + \rho_1)^2 \sin 2\theta - (1 + \rho_1) \rho_2 \cos \theta]. \quad (\text{C.22})$$

Then Eq. (C.20) can be written as

$$\begin{aligned} \frac{\omega^2 - \omega_L^2}{\tilde{\Omega}^2} \delta S_+ = & \left\{ \frac{5}{6g_D} [6K_1\rho_2^2 + K_1(\rho_1^2 + 1)] \partial_y \partial_y + \frac{5}{6g_D} [3K_1\rho_1^2 + K_1(2\rho_2^2 + 1)] \partial_x \partial_x \right. \\ & - i \frac{10}{6g_D} [(K_1 + 3\rho_1^2 K_1 \cos 2\theta) \partial_x \theta \partial_x - K_1(1 + \rho_1^2) \partial_y \theta \partial_y] \} \delta S_+ \quad (\text{C.23}) \\ & - i \frac{5K_1}{6g_D} \tilde{\zeta}_D^{-2} [(1 + \rho_1)^2 \sin 2\theta - (1 + \rho_1) \rho_2 \cos \theta] \delta S_+ \\ & + \{ (1 + \rho_1) [-(1 + \rho_1) \cos 2\theta - 5\rho_2 \sin \theta] + (1 + \rho_1^2 + 4\rho_2^2) \} \delta S_+. \end{aligned}$$

This is Eq. (5.20).

Appendix D

Separable spin soliton with $\theta_{KLS} = \pi$ and its NMR

D.1 Pseudo-random lattices with two different domain wall boundary conditions – $\theta_{KLS} = 0$ and $\theta_{KLS} = \pi$

Here, we demonstrate the numeric results the spin textures of one-half unit cell of the lattices consisting of separable spin solitons with topological invariant $1/4 + 1/4$ under these two boundary conditions. The London limit free energies of one-half unit cell and the surface densities of London limit free energies of the pseudo-random lattices were calculated. In Fig. D.1 (a) and (b), we show the equilibrium spin textures in one-half unit cell. We can see these two textures are related by π -rotation about x -axis. They have same London limit free energies as well as same surface densities of free energy as shown in Fig. D.1 (c) and (d).

D.2 NMR frequency shifts Of soliton ($|\Delta\theta| = \pi - 2\theta_0$) and big-soliton ($|\Delta\theta| = \pi + 2\theta_0$)

Here we discuss the transverse NMR frequency shifts of soliton ($|\Delta\theta| = \pi - 2\theta_0$) and big-soliton ($|\Delta\theta| = \pi + 2\theta_0$) in the absence of KLS string wall. The frequency shifts λ are numeric results of Eq. (5.20) with equilibrium spin textures of soliton ($|\Delta\theta| = \pi - 2\theta_0$) and big-soliton ($|\Delta\theta| = \pi + 2\theta_0$) which we got in Sec. 4.3.2. We depict the results with $|q|$ from 0.0 to 0.2 in Fig. D.2. It shows the transverse NMR frequency shift of soliton ($|\Delta\theta| = \pi - 2\theta_0$) increases when $|q|$ increases, while the transverse NMR frequency shift of big-soliton ($|\Delta\theta| = \pi + 2\theta_0$) decreases when $|q|$ increases. The typical values of λ of soliton and big-soliton are $\lambda \geq -0.7$ and $\lambda \leq -1.3$ respectively when $|q| \geq 0.14$.

Because the unit cell of pseudo-random lattices of separable spin solitons with topological invariant $1/4 + 1/4$ contains KLS-soliton and soliton, the transverse NMR frequency shift of unit cell is determined by the equilibrium spin texture of soliton. As are result, λ of pseudo-random lattices consisting of separable spin soliton with topological invariant $1/4 + 1/4$ is very close to those induced by soliton ($|\Delta\theta| = \pi - 2\theta_0$).

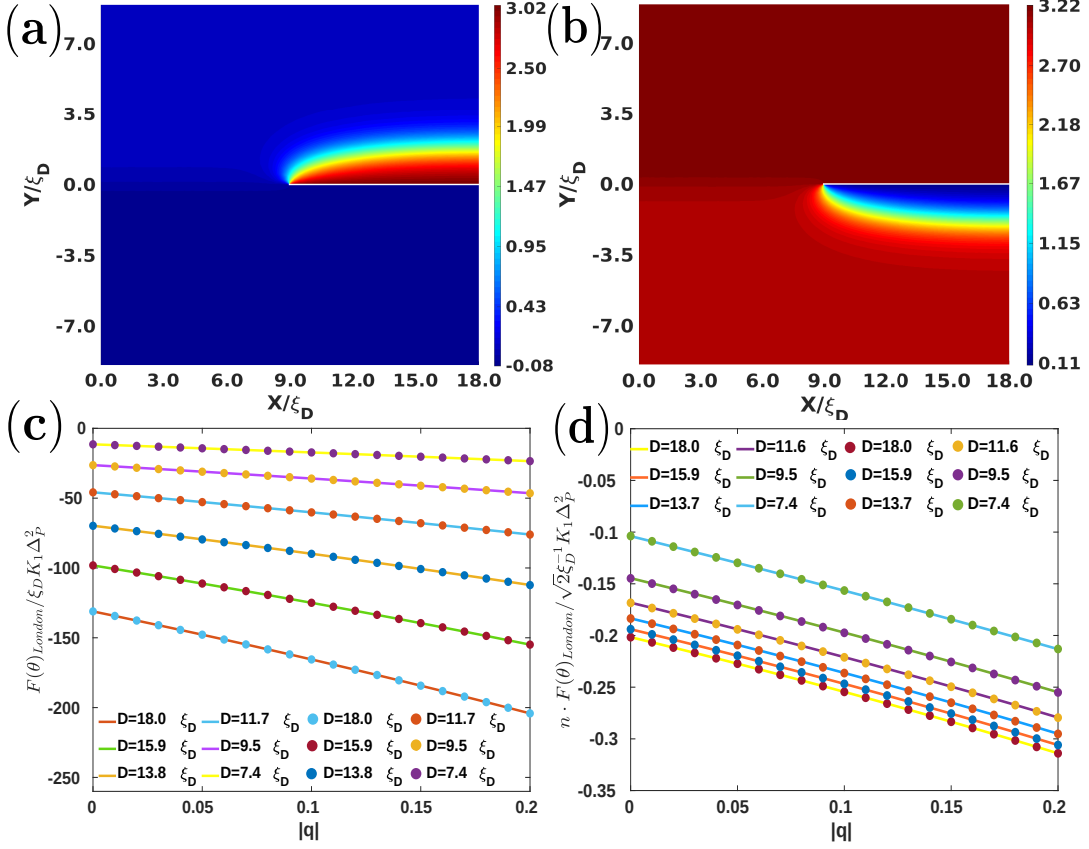


FIGURE D.1: Equilibrium spin textures and equilibrium London limit free energies of one-half unit cell consisting of $1/4 + 1/4$ separable spin solitons with $\theta_{KLS} = 0$ and $\theta_{KLS} = \pi$. The dots represent data of equilibrium configurations with $\theta_{KLS} = 0$, while the solid lines represent data of equilibrium configurations with $\theta_{KLS} = \pi$. (a) is the equilibrium spin textures of one-half unit cell with $\theta_{KLS} = 0$, $|q| = 0.2$ and $D = 18\zeta_D$. (b) is the equilibrium spin textures of one-half unit cell with $\theta_{KLS} = \pi$, $|q| = 0.2$ and $D = 18\zeta_D$. (a) and (b) have same $|\Delta\theta| = \pi$ and are related by a π -rotation around \hat{x} axis. (c) depicts the equilibrium London limit free energies of spin textures with $\theta_{KLS} = 0$ and $\theta_{KLS} = \pi$ respectively. (d) depicts the surface densities of equilibrium London limit free energies of spin textures with $\theta_{KLS} = 0$ and $\theta_{KLS} = \pi$ respectively. (c) and (d) demonstrate the pseudo-random lattices consisting of separable spin solitons have same equilibrium London limit free energies for boundary conditions $\theta_{KLS} = 0$ and $\theta_{KLS} = \pi$.

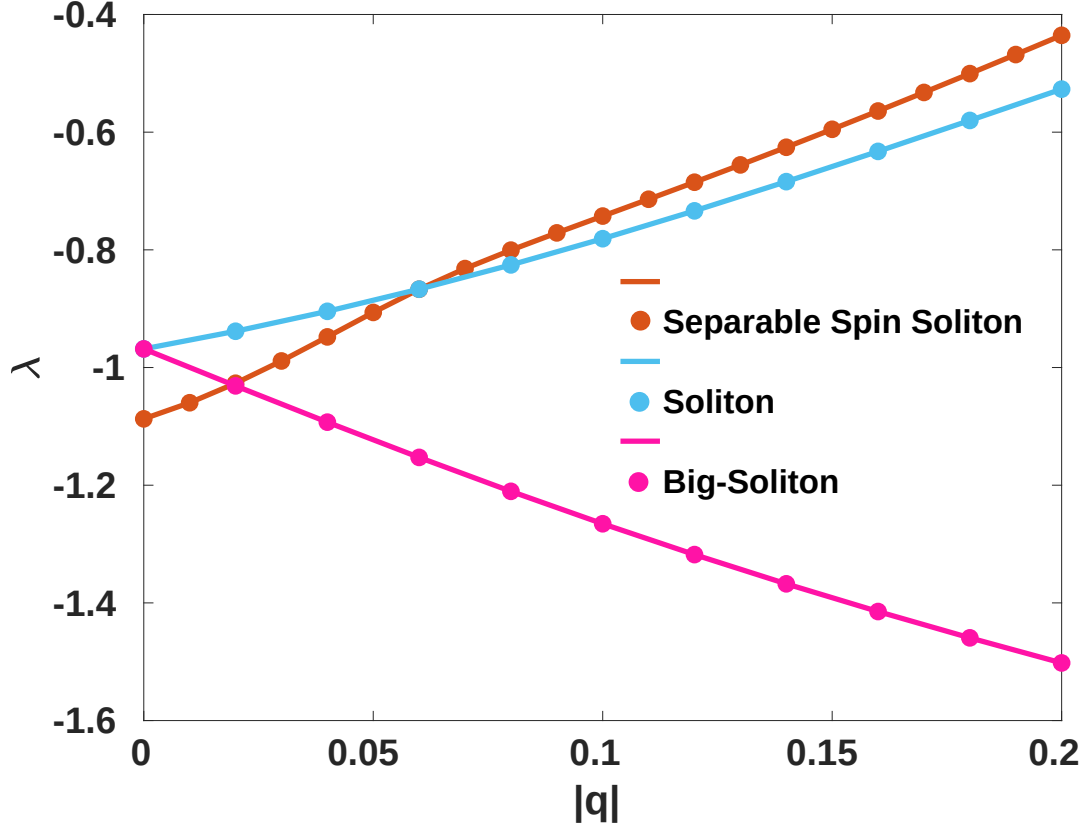


FIGURE D.2: NMR frequency shifts of unit cell of pseudo-random lattices consisting of separable spin soliton, NMR frequency shifts of soliton ($|\Delta\theta| = \pi - 2\theta_0$) and big-soliton ($|\Delta\theta| = \pi + 2\theta_0$). All colored dots are original numeric data, while colored lines are the linear interpolations of numeric data. $D = 14.1\xi_D$. We found the NMR frequency shifts λ of soliton ($|\Delta\theta| = \pi - 2\theta_0$) monotonically increase when $|q|$ increases. The typical values of λ of soliton (blue line) are larger than -0.7 when $|q| \geq 0.14$. In contrast, the NMR frequency shifts of big-soliton (pink line) monotonically decrease when $|q|$ increases and the typical values of λ in this case are smaller than -1.35 when $|q| \geq 0.14$. On the other side, the frequency shifts induced by pseudo-random lattices of 2/4 separable spin solitons (brown lines) monotonically increase as $|q|$ increase. The typical values of λ are larger than -0.65 when $|q| > 0.14$. We find this range of λ are very close to those induced by soliton ($|\Delta\theta| = \pi - 2\theta_0$). This is because only the soliton ($|\Delta\theta| = \pi - 2\theta_0$) of 2/4 separable spin soliton responds to the continuous wave transverse magnetic drive. Moreover, we can see that the frequency shifts of pseudo-random lattices consisting of 2/4 separable spin solitons is smaller than -1 when $|q| = 0$. This deviates from the experimental observations of the frequency shifts of spin soliton in polar phase with $|q| = 0$ [35].

Bibliography

- [1] Zaven. Arzoumanian et al. “The NANOGrav 12.5 yr data set: Search for an isotropic stochastic gravitational-wave background”. In: *Astrophys. J. Lett.* 905 (2021), p. L34.
- [2] Vedran. Brdar Simone. Blasi and Kai. Schmitz. “Has NANOGrav found first evidence for cosmic strings?” In: *Phys. Rev. Lett.* 126 (2021), p. 041305.
- [3] John. Ellis and Marek. Lewicki. “Cosmic string interpretation of NANOGrav pulsar timing data”. In: *Phys. Rev. Lett.* 126 (2021), p. 041304.
- [4] G. Franciolini V. De. Luca and A. Riotto. “NANOGrav data hints at primordial black holes as dark matter”. In: *Phys. Rev. Lett.* 126 (2021), p. 041303.
- [5] V. Vaskonen and H. Veermäe. “Did NANOGrav see a signal from primordial black hole formation?” In: *Phys. Rev. Lett.* 126 (2021), p. 051303.
- [6] T. W. B. Kibble. “Topology of cosmic domains and strings”. In: *Journal of Physics A: Mathematical and General* 9 (1976), p. 1387.
- [7] A. Vilenkin and E. P. S. Shellard. *Cosmic Strings and Other Topological Defects*. Cambridge University Press, 1994.
- [8] M. B. Hindmarsh and T. W. B. Kibble. “Cosmic strings,” in: *Rep. Prog. Phys* 58 (1995), p. 477.
- [9] J. Robinson R. A. Battye and A. Albrecht. “Structure formation by cosmic strings with a cosmological constant”. In: *Phys. Rev. Lett.* 80 (1998), pp. 4847–50.
- [10] J. H. P. Wu P. P. Avelino E. P. S. Shellard and B. Allen. “Cosmic- string-seeded structure formation”. In: *Phys. Rev. Lett.* 81 (1998), pp. 2008–11.
- [11] M. Majumdar and A. C. Davis. “Cosmological creation of D-branes and anti-D-branes”. In: *JHEP* 0203 (2002), p. 056.
- [12] S. Sarangi and S.-H. H. Tye. “Cosmic string production towards the end of brane inflation”. In: *Phys. Lett. B* 536 (2002), pp. 185–192.
- [13] S.-H. H. Tye L. Pogosian, I. Wasserman, and M. Wyman. “Observational constraints on cosmic string production during brane inflation”. In: *Phys. Rev. D* 68 (2003), p. 023506.
- [14] G. Dvali and A. Vilenkin. “Formation and evolution of cosmic D-strings”. In: *JCAP* 0403 (2004), p. 010.
- [15] J. Rocher R. Jeannerot and M. Sakellariadou. “How generic is cosmic string formation in SUSY GUTs?” In: *Phys. Rev. D* 68.10351 (2003), p. 4.
- [16] S. Dimopoulos N. Arkani-Hamed and G. R. Dvali. “The hierarchy problem and new dimensions at a millimeter”. In: *Phys. Lett. B* 429 (1998), p. 263.
- [17] S. Dimopoulos N. Arkani-Hamed and G. R. Dvali. “Phenomenology, astrophysics and cosmology of theories with sub-millimeter dimensions and TeV scale quantum gravity”. In: *Phys. Rev. D* 59 (1999), p. 086004.

- [18] L. Randall and A R. Sundrum. “large mass hierarchy from a small extra dimension,” in: *Phys. Rev. Lett.* 83 (1999), p. 3370.
- [19] T.W.B. Kibble. “Cosmic strings reborn?” In: *arXiv:astro-ph/* (2004), p. 0410073.
- [20] M. Kunz R. Durrer and A. Melchiorri. “Cosmic structure formation with topological defects”. In: *Phys. Rep.* 364 (2002), pp. 1–81.
- [21] M. B. Hindmarsh C. Contaldi and J. Magueijo. “Cosmic microwave background and density fluctuations from strings plus inflation”. In: *Phys. Rev. Lett.* 82 (1999), pp. 2034–2037.
- [22] P. Peter F. R. Bouchet, A. Riazuelo, and M. Sakellariadou. “Evidence against or for topological defects in the BOOMERanG data”. In: *Phys. Rev. D* 65 (2002), p. 021301.
- [23] M. B. Hindmarsh and T. W. B. Kibble. “Cosmic strings”. In: *Rep. Prog. Phys.* 58 (1995), p. 477.
- [24] A. Vilenkin and E.S. Shellard. *Cosmic Strings and Other Topological Defects*. Cambridge University Press, 2000.
- [25] Y. Cui et al. “Cosmic archaeology with gravitational waves from cosmic strings”. In: *Phys. Rev. D* 97 (2018), p. 123505.
- [26] D. Matsunami et al. “Decay of Cosmic String Loops due to Particle Radiation”. In: *Phys. Rev. Lett.* 122 (2019), p. 201301.
- [27] P. Auclair, D.A. Steer, and T. Vachaspati. “Particle emission and gravitational radiation from cosmic strings: Observational constraints”. In: *Phys. Rev. D* 101 (2020), p. 083511.
- [28] G. Lazarides T. W. B. Kibble and Q. Shafi. “Walls bounded by strings”. In: *Phys. Rev. D* 26 (1982).
- [29] T.W.B. Kibble, G. Lazarides, and Q. Shafi. “Strings in SO(10)”. In: *Phys. Lett. B* 113.3 (1982), pp. 237–239.
- [30] V. M. H. Ruutu et al. “Vortex formation in neutron-irradiated superfluid ^3He as an analogue of cosmological defect formation”. In: *Nature* 382 (1996), pp. 334–336.
- [31] T. W. B. Kibble and G. E. Volovik. “On phase ordering behind the propagating front of a second-order transition”. In: *JETP Lett* 65 (1997), pp. 102–107.
- [32] M. J. Duff and K. S. Stelle. “Sir Thomas Walter Bannerman Kibble. 23 December 1932 – 2 June 2016”. In: *Biographical Memoirs of Fellows of the Royal Society* 70 (2021), pp. 225–244.
- [33] J. E. Kiskis. “Disconnected gauge groups and the global violation of charge conservation”. In: *Phys. Rev. D* 17 (1978), p. 3196.
- [34] A. S. Schwarz. “Field theories with no local conservation of the electric charge”. In: *Nucl. Phys. B* 208 (1982), p. 141.
- [35] S. Autti et al. “Observation of half-quantum vortices in superfluid ^3He ”. In: *Phys. Rev. Lett.* 117 (2016), p. 255301.
- [36] J. V. Porto and J. M. Parpia. “Superfluid ^3He in Aerogel”. In: *Phys. Rev. Lett.* 74 (23 1995), pp. 4667–4670.
- [37] E. V. Thuneberg et al. “Models for Superfluid ^3He in Aerogel”. In: *Phys. Rev. Lett.* 80 (1998), pp. 2861–2864.

- [38] D. T. Sprague et al. "Homogeneous Equal-Spin Pairing Superfluid State of ^3He in Aerogel". In: *Phys. Rev. Lett.* 75 (1995), pp. 661–664.
- [39] H. Alles et al. "Evidence for Superfluid B Phase of ^3He in Aerogel". In: *Phys. Rev. Lett.* 83 (1999), pp. 1367–1370.
- [40] B. I. Barker et al. "Observation of a Superfluid He-3 A- B Phase Transition in Silica Aerogel". In: *Phys. Rev. Lett.* 85 (Sept. 2000), pp. 2148–2151.
- [41] J. E. Baumgardner et al. "Interfacial Pinning in the Superfluid ^3He A–B Transition in Aerogel". In: *Phys. Rev. Lett.* 93 (2004), p. 055301.
- [42] G. Gervais et al. "Modification of the Superfluid ^3He Phase Diagram by Impurity Scattering". In: *Phys. Rev. Lett.* 87 (2001), p. 035701.
- [43] S. N. Fisher et al. "Thermal Conductivity of Liquid ^3He in Aerogel: A Gapless Superfluid". In: *Phys. Rev. Lett.* 91 (2003), p. 105303.
- [44] K. Kotera et al. "Observation of superfluidity of ^3He in aerogel by fourth sound technique". In: *Physica B: Condensed Matter* 329-333 (2003), pp. 316–317.
- [45] I. A. Fomin. "Order parameter of A-like ^3He phase in aerogel". In: *JETP Lett* 77 (2003), pp. 240–242.
- [46] W. P. Halperin and J. A. Sauls. "Helium-Three in Aerogel". In: *arXiv:cond-mat/* (2004), p. 0408593.
- [47] K. Aoyama and R. Ikeda. "Superfluid transition to ABM state of ^3He in aerogel". In: *Journal of Physics and Chemistry of Solids* 66 (2005), pp. 1330–1333.
- [48] Seiji Higashitani et al. "Sound propagation in superfluid ^3He in aerogel". In: *Journal of Physics and Chemistry of Solids* 66 (2005), pp. 1334–1338.
- [49] Y. M. Bunkov, E. C., and H. Godfrin. " ^3He NMR in aerogel". In: *Journal of Physics and Chemistry of Solids* 66.8 (2005), pp. 1325–1329.
- [50] I. A. Fomin. "Nanoimpurities in the superfluid ^3He ". In: *Journal of Physics and Chemistry of Solids* 66.8 (2005), pp. 1321–1324.
- [51] K. Aoyama and R. Ikeda. "Pairing states of superfluid ^3He in uniaxially anisotropic aerogel". In: *Phys. Rev. B* 73 (2006), p. 060504.
- [52] G. E. Volovik. "On Larkin-Imry-Ma State of ^3He -A in Aerogel". In: *J. Low. Temp. Phys* 150 (2008), pp. 453–463.
- [53] I. A. Fomin and E. V. Surovtsev. "Long-Range Order in the A-like Phase of Superfluid ^3He in Aerogel". In: *Journal of Low Temperature Physics* 150 (2008), pp. 464–471.
- [54] E. V. Surovtsev. and I. A. Fomin. "Model Calculation of Orientational Effect of Deformed Aerogel on the Order Parameter of Superfluid ^3He ". In: *Journal of Low Temperature Physics* 150.8 (2008), pp. 487–492.
- [55] D.I. Bradley et al. "Magnetic Distortion of the B-like Phase of Superfluid ^3He Confined in Aerogel". In: *Journal of Low Temperature Physics* 150 (2008), pp. 445–452.
- [56] V.V. Dmitriev · D.A. Krasnikhin · N. Mulders · D.E. Zmeev. "Soliton-Like Spin State in the A-Like Phase of ^3He in Anisotropic Aerogel". In: *Journal of Low Temperature Physics* 150 (2008), pp. 493–498.
- [57] T. Kunimatsu et al. "Quantum Fluid Dynamics of Rotating Superfluid ^3He in Aerogel". In: *Journal of Low Temperature Physics* 150 (2008), pp. 435–444.

- [58] H. Nakagawa et al. "A-B Phase Conversion and Coexistence of Superfluid ^3He in Aerogel". In: *Journal of Low Temperature Physics* 150.8 (2008), pp. 472–475.
- [59] J. A. Sauls. "Chiral phases of superfluid ^3He in an anisotropic medium". In: *Phys. Rev. B* 88 (21 Dec. 2013), p. 214503.
- [60] I. A. Fomin and E. V. Surovtsev. "Distorted Axi-Planar Superfluid Phase of ^3He in the "Nematically Ordered" Aerogel". In: *JETP Lett* 97.11 (2013), pp. 644–648.
- [61] Fomin. I.A. "Phenomenological phase diagram of superfluid ^3He in a stretched aerogel". In: *JETP* 118 (2014), pp. 765–770.
- [62] S. Yang and R. Ikeda. "Possibility of Unconventional Pairing States in Superfluid ^3He in Uniaxially Anisotropic Aerogels". In: *Journal of the Physical Society of Japan* 83.8 (2014), p. 084602.
- [63] Ikeda. Ryusuke. "Anisotropic strong-coupling effects on superfluid ^3He in aerogels: Conventional spin-fluctuation approach". In: *Phys. Rev. B* 91 (17 May 2015), p. 174515.
- [64] J. I. A. Li et al. "Stability of Superfluid ^3He –B in Compressed Aerogel". In: *Phys. Rev. Lett.* 112 (11 Mar. 2014), p. 115303.
- [65] J. I. A. Li et al. "Anisotropic Phases of Superfluid ^3He in Compressed Aerogel". In: *Phys. Rev. Lett.* 114 (10 Mar. 2015), p. 105302.
- [66] R. Sh. Askhadullin et al. "Measurements of spin diffusion in liquid ^3He in "ordered" aerogel". In: *J. Phys.: Conf. Ser.* 400 (2012), p. 012002.
- [67] V. V. Dmitriev et al. "Polar phase of superfluid ^3He in anisotropic aerogel". In: *Phys. Rev. Lett.* 115 (2015), p. 16530.
- [68] P. W. Anderson. "Theory of dirty superconductors," in: *J. Phys. Chem. Solids* 11 (1959), pp. 26–30.
- [69] I. A. Fomin. "Analog of Anderson theorem for the polar phase of liquid ^3He in nematic aerogel". In: *JETP* 127 (2018), pp. 933–938.
- [70] I. A. Fomin. In: *Temperature dependence of the order parameter of the polar phase of liquid ^3He in nematic aerogel* (). arXiv: [2003.09652](https://arxiv.org/abs/2003.09652).
- [71] M. Tange and R. Ikeda. "Half-quantum vortex pair in polar-distorted B phase of superfluid ^3He in aerogels". In: *Phys. Rev. B.* 101 (2020), p. 094512.
- [72] R. Sh. Askhadullin et al. "Phase diagram of ^3He in "nematically ordered" aerogel". In: *JETP Lett.* 95 (2012), p. 326.
- [73] V. V. Dmitriev et al. "B phase with polar distortion in superfluid ^3He in "ordered" aerogel". In: *JETP* 119 (2014), p. 1088.
- [74] J. T. Mäkinen et al. "Half-quantum vortices and walls bounded by strings in the polar-distorted phases of topological superfluid ^3He ". In: *Nat. Comm.* 10 (2019), p. 237.
- [75] Kibble T.W.B. *Classification of Topological Defects and Their Relevance to Cosmology and Elsewhere. Topological Defects and the Non-Equilibrium Dynamics of Symmetry Breaking Phase Transitions*. NATO Science Series (Series C: Mathematical and Physical Sciences). Ed. by Bunkov Y.M. and Godfrin H. Vol. 549. Dordrecht: Springer, 2000.

- [76] Y. B. Zeldovich, I. Y. Kobzarev, and L. B. Okun. "Cosmological consequences of the spontaneous breakdown of discrete symmetry". In: *Zh. Eksp. Teor. Fiz.* 67 (1974), p. 3.
- [77] Y. B. Zeldovich, I. Y. Kobzarev, and L. B. Okun'. "Cosmological consequences of a spontaneous breakdown of a discrete symmetry". In: *Sov. Phys. JETP* 40 (1974), p. 1.
- [78] A. Vilenkin and A. E. Everett. "Cosmic strings and domain walls in models with Goldstone and pseudo-Goldstone bosons". In: *Phys. Rev. Lett.* 48 (1982), p. 1867.
- [79] P. Sikivie. "Of Axion, Domain walls and the early Universe". In: *Phys. Rev. Lett.* 48 (1982).
- [80] M. C. Huang and P. Sikivie. "Structure of axionic domain walls". In: *Phys. Rev. D* 32 (1985), pp. 1560–1568.
- [81] P. Sikivie. *Axion Cosmology* In: Kuster M., Raffelt G., Beltrán B. (eds) *Axions. Lecture Notes in Physics*. Vol. 741. Berlin, Heidelberg: Springer, 2008.
- [82] Jihn E. Kim and Gianpaolo Carosi. "Axions and the strong CP problem". In: *Rev. Mod. Phys.* 82 (2010), pp. 557–601.
- [83] G. Lazarides and Q. Shafi. "Axion Models with No Domain Wall Problem". In: *Phys. Lett. B* 115 (1982), pp. 21–25.
- [84] G. Lazarides and Q. Shafi. "Superconducting String in Axion Models". In: *Phys. Lett. B* 151 (1985), pp. 123–126.
- [85] R. Sato, F. Takahashi, and M. Yamada. "Unified Origin of Axion and Monopole Dark Matter, and Solution to the Domain- wall Problem, Phys". In: *Rev. D* 98 (2018), p. 043535.
- [86] C. Chatterjee, T. Higaki, and M. Nitta. "Note on a solution to domain wall problem with the Lazarides-Shafi mechanism in axion dark matter models, Phys". In: *Rev. D* 101 (2020), p. 075026.
- [87] A. Caputo and M. Reig. "Cosmic implications of a low-scale solution to the axion domain wall problem, Phys". In: *Rev. D* 100 (2019), p. 063530.
- [88] Y. Nambu. "String-like configurations in the Weinberg-Salam theory". In: *Nucl. Phys. B* 130.505 (1977).
- [89] G. E. Volovik. *The Universe in a Helium Droplet*. Oxford University Press, 2009.
- [90] Allen Hatcher. *Algebraic Topology*. Cambridge University Press, 2002.
- [91] V. P. Mineyev and G. E. Volovik. "Planar and linear solitons in superfluid ^3He , Phys". In: *Rev. B* 18 (1978), pp. 3197–3203.
- [92] N. D. Mermin. "The topological theory of defects in ordered media, Rev". In: *Mod. Phys* 51 (1979), p. 591.
- [93] L. Michel. "Symmetry defects and broken symmetry". In: *Configurations Hidden Symmetry Rev* 52 (1980).
- [94] D. Vollhardt and P. Wölfle. *The superfluid phases of helium 3*. London: Taylor and Francis, 1990.
- [95] R. Sh. Askhadullin et al. "Liquid metal based technology of synthesis of nanostructured materials (by the example of oxides). These materials properties and applications areas". In: *J. Phys.: Conf. Ser.* 98 (2008), p. 072012.

- [96] Siegfried. Hess. *Tensors for Physics*. Ed. by Bunkov Y.M. and Godfrin H. Switzerland: Springer International Publishing Switzerland, 2015.
- [97] G. E. Volovik and K. Zhang. "String monopoles, string walls, vortex-skyrmions and nexus objects in polar distorted B-phase of ^3He ". In: *Physical Review Research* 2 (2020), p. 023263.
- [98] A. Ramires, D. F. Agterberg, and M. Sigrist. "Tailoring T_c by symmetry principles: The concept of superconducting fitness, Phys". In: *Rev. B* 98 (2018), p. 024501.
- [99] V. B. Eltsov, J. Rysti T. Kamppinen, and G. E. Volovik. "Topological nodal line in superfluid ^3He and the Anderson theorem". In: *arXiv* (), p. 1908.01645.
- [100] G. E. Volovik and V. P. Mineev. "Investigation of singularities in superfluid ^3He and liquid crystals by homotopic topology methods". In: *JETP* 45 (1977), pp. 1186–1196.
- [101] Y. Kondo et al. "Combined spin - mass vortices with soliton tail in superfluid $^3\text{He-B}$, Phys". In: *Rev. Lett.* 68 (1992), p. 3331.
- [102] G. E. Volovik. *Exotic Properties of Superfluid Helium-3*. World Scientific, 1992.
- [103] S. A. Pikin. "Weak first-order phase transitions". In: *Physica A: Statistical Mechanics and its Applications* 194 (1993), pp. 352–363.
- [104] M. Gleiser. *Electroweak Physics and the Early Universe. NATO ASI Series (Series B: Physics) 1994) On the Strength of First Order Phase Transitions*. Ed. by Romão J.C. and Freire F. Vol. 338. Boston: Springer, 1994.
- [105] H. Arkin et al. "Phase separation in a weak first-order phase transition". In: *Physica A: Statistical Mechanics and its Applications* 274 (1999), pp. 320–324.
- [106] M. M. Salomaa and G. E. Volovik. "Cosmiclike domain walls in superfluid $^3\text{He-B}$: Instantons and diabolical points in (\mathbf{k}, \mathbf{r}) space". In: *Phys. Rev. B* 37 (1988), pp. 9298–9311.
- [107] Charles Nash and Siddhartha Sen. *Topology and Geometry for Physicists*. Academic Press, 1988.
- [108] V. L. Golo and M. I. Monastyrsky. "Gauge groups and topological invariants of vacuum manifolds, Ann. l'I". In: *H.P. Phys* 28 (1978), pp. 75–89.
- [109] N. D. Mermin, V. P. Mineev, and G. E. Volovik. "Topological analysis of cores of singularities in the $^3\text{He-A}$, J". In: *Low Temp* 33 (1978), pp. 117–126.
- [110] G. E. Volovik. "Topological singularities on the surface of an ordered system". In: *Pis'ma. Zh. Eksp. Teor. Fiz.* 28 (1978), pp. 59–62.
- [111] I. Martin. Isaacs. *Algebra : a graduate course*. Providence, Rhode Island: American Mathematical Society, 2009.
- [112] M. Suzuki. *Group Theory I*. Berlin: Springer-Verlag, Heidelberg, 1982.
- [113] H. F. Jones. *Groups, Representations and Physics*. CRC Press, 1998.
- [114] M. Nakahara. *Geometry, Topology and Physics*. CRC Press, 2003.
- [115] G. E. Volovik. "Monopoles and fractional vortices in chiral superconductors". In: *Proc. Natl. Acad. Sci. U.S.A.* 97, 2000, pp. 2431–2436.
- [116] S. Blaha. "Quantization rules for point singularities in superfluid ^3He and liquid crystals, Phys". In: *Rev. Lett.* 36 (1976), pp. 874–876.
- [117] G. E. Volovik and V. P. Mineev. "Vortices with free ends in superfluid $^3\text{He-A}$, JETP". In: *Lett.* 23 (1976), pp. 593–596.

- [118] T. W. B. Kibble and T. Vachaspati. "Monopoles on strings," in: *J. Phys. G* 42 (2015), p. 094002.
- [119] A. Saurabh and T. Vachaspati. "Monopole–antimonopole: interaction, scattering and creation, Phil". In: *Trans. R. Soc. A* 377 (2019), p. 20190143.
- [120] G. Lazarides and Q. Shafi. "Monopoles, Strings, and Necklaces in $SO(10)$ and E_6 , J". In: *High Energ. Phys* 2019 (2019), p. 193.
- [121] G. E. Volovik. *Composite topological objects in topological superfluids*. 2019. arXiv: [1912.05962 \[cond-mat.other\]](#).
- [122] G. Lazarides and Q. Shafi. *Triply Charged Monopole and Magnetic Quarks*. 2021. arXiv: [2101.01412 \[hep-ph\]](#).
- [123] Seji Kang et al. "Observation of Wall-Vortex Composite Defects in a Spinor Bose-Einstein Condensate". In: *Phys. Rev. Lett.* 122 (2019), p. 095301.
- [124] S-C. Gou I-K. Liu and H. Takeuchi. "Phase diagram of solitons in the polar phase of a spin-1 Bose-Einstein condensate". In: *Phys. Rev. Research* 2 (Sept. 2020), p. 033506.
- [125] N. Mermin and T.-L. Ho. "Circulation and angular momentum in the A-phase of superfluid helium-3, Phys". In: *Rev. Lett.* 36 (1976), p. 594.
- [126] P. W. Anderson and G. Toulouse. "Phase slippage without vortex cores: vortex textures in superfluid ^3He , Phys". In: *Rev. Lett.* 38 (1977), pp. 508–511.
- [127] V. R. Chechetkin. "Types of vortex solutions in superfluid ^3He ". In: *JETP* 44 (1976), pp. 766–772.
- [128] G. E. Volovik and N. B. Kopnin. "On the rotating ^3He - A, Pis'ma". In: *Zh. Eksp. Teor. Fiz.* 25 (1977), pp. 22–24.
- [129] H. K. Seppälä et al. "Continuous vortices with broken symmetry in rotating superfluid ^3He -A, Phys". In: *Rev. Lett.* 52 (1984), pp. 1802–1805.
- [130] J. P. Pekola et al. "Observation of a topological transition in the ^3He -A vortices, Phys". In: *Rev. Lett* 65 (1990), pp. 3293–3296.
- [131] T. D. C. Bevan et al. "Momentum creation by vortices in superfluid ^3He as a model of primordial baryogenesis". In: *Nature* 386 (1997), pp. 689–692.
- [132] G. E. Volovik. "Half quantum vortices in the B phase of superfluid ^3He ". In: *JETP Lett.* 52 (1990), p. 358.
- [133] K. Zhang. "One-dimensional nexus objects, network of Kibble-Lazarides-Shafi string walls, and their spin dynamic response in polar-distorted B-phase of ^3He ". In: *Phys. Rev. Research* 2 (2020), p. 043356.
- [134] V. P. Mineyev and G. E. Volovik. "Planar and linear solitons in superfluid ^3He , Phys". In: *Rev. B* 18 (1978), p. 3197.
- [135] M. Tange and R. Ikeda. "Half-quantum vortex pair in polar-distorted B phase of superfluid ^3He in aerogels, Phys". In: *Rev. B.* 101 (2020), p. 094512.
- [136] G. E. Volovik. "Exotic Properties of Superfluid Helium 3". In: (1992).
- [137] J. Nocedal and S. J. Wright. *Numerical Optimization*. Springer, New York, 2006.
- [138] M. M. Salomaa and G. E. Volovik. "Half-quantum vortices in superfluid ^3He -A". In: *Phys. Rev. Lett.* 55 (1985), pp. 1184–1187.
- [139] G. E. Volovik et al. "Spin, orbital, Weyl and other glasses in topological superfluids". In: *J. Low. Temp. Phys* 196 (2019).

- [140] A. Altland and D. Simons. 2nd ed. *Condensed Matter Field Theory* (: Cambridge University Press, 2010).
- [141] P. W. Anderson. "Some Macroscopic Considerations on Motions of Anisotropic Superfluids". In: *Phys. Rev. Lett.* 30 (1973), p. 368.
- [142] P. W. Anderson and C. Varma. "Properties of a Possible Superfluid State of ^3He ". In: *Nature* 241 (1973), p. 187.
- [143] P. M. Chaikin and T. C. Lubensky. *Principles of Condensed Matter Physics*. Cambridge University Press, 1995.
- [144] I. E. Dzyaloshinskii and G. E. Volovick. "Poisson brackets in condensed matter physics". In: *Annals of Physics* 125 (1980), pp. 67–97.
- [145] P. G. Ciarlet. *The Finite Element Method for Elliptic Problems*. North Holland, 1978.
- [146] S. M. Dahir, A. F. Volkov, and I. M. Eremin. "Interaction of skyrmions and Pearl vortices in superconductor-chiral ferromagnet heterostructures". In: *Phys. Rev. Lett.* 122 (2019), p. 097001.
- [147] S. Rex, I. V. Gornyi, and A. D. Mirlin. "Majorana bound states in magnetic skyrmions imposed onto a superconductor, Phys". In: *Rev. B* 100 (2019), p. 064504.
- [148] G. Lazarides and Q. Shafi. "The Fate of Primordial Magnetic Monopoles, Phys". In: *Lett. B* 94 (1980), pp. 149–152.
- [149] G. Lazarides and Q. Shafi. *Electroweak Monopole and Magnetic Dumbbell in $SU(5)$* . 2021. arXiv: [2102.07124 \[hep-ph\]](#).
- [150] Joydeep Chakraborty et al. "Primordial monopoles and strings, inflation, and gravity waves". In: *Journal of High Energy Physics* 2021.2 (2021).
- [151] J. Chakraborty et al. "Roadmap of left-right models based on GUTs, Phys". In: *Rev. D* 97 (2018), p. 095010.
- [152] J. Chakraborty, R. Maji, and S. F. King. "proton decay, and topological defects in non-SUSY GUTs with thresholds, Phys". In: *Rev. D* 99 (2019), p. 095008.
- [153] Xi Chen et al. "First-principles experimental demonstration of ferroelectricity in a thermotropic nematic liquid crystal: Polar domains and striking electro-optics". In: (2020).
- [154] Hiromitsu Takeuchi. "Quantum Elliptic Vortex in a Nematic-Spin Bose-Einstein Condensate". In: *Phys. Rev. Lett.* 126 (2021), p. 195302.
- [155] A. B. Vorontsov and J. A. Sauls. "Crystalline order in superfluid ^3He films, Phys". In: *Rev. Lett.* 98 (2007), p. 045301.
- [156] J. Shook et al. "Stabilized pair density wave via nanoscale confinement of superfluid ^3He -A, Phys". In: *Rev. Lett.* 124 (2020), p. 015301.
- [157] L. V. Levitin et al. "Evidence for a spatially modulated superfluid phase of ^3He under confinement, Phys". In: *Rev. Lett.* 122 (2019), p. 085301.
- [158] T. H. R. Skyrme. "A unified field theory of mesons and baryons, Nucl". In: *Phys* 31 (1962), pp. 556–569.
- [159] U. A. Khawaja and H. Stoof. "Skyrmions in a ferromagnetic Bose-Einstein Condensate". In: *Nature* 411 (2001), pp. 918–920.
- [160] P. G. Ciarlet. *The Finite Element Method for Elliptic Problems*. North Holland, 1978.

- [161] K. Zhang. *Codes for 3D-2D Kibble Lazarides Shafi Domain Wall in Polar Distorted B-Phase*. 2021. URL: https://github.com/timohyva/3D-2D_Kibble_Razarides_Shafi_Domain_Wall_in_Polar_Distorted_BPhase (visited on 03/29/2021).